(2)

DETERMINATION OF SHEAR WAVE VELOCITY STRUCTURE IN THE RIO GRANDE RIFT THROUGH RECEIVER FUNCTION AND SURFACE WAVE ANALYSIS

by

BRIAN P. MURPHY, B.S.

THESIS

Presented to the Faculty of the Graduate School of

The University of Texas at El Paso

in Partial Fullfillment

of the Requirements

for the Degree of

MASTER OF SCIENCE

Department of Geological Sciences

THE UNIVERSITY OF TEXAS AT EL PASO

August, 1991

Appendix B

ACKNOWLEDGEMENTS

I express sincere appreciation to my committee chairperson, Dr. D. I. Doser, for the training in geophysics I have received as her graduate student. Thanks also to committee members Dr. G. R. Keller, Dr. E. Y. Anthony, and Dr. E. A. Dean for their assistance and instruction during this study. A special thanks goes to Dr. T. J. Owens, Dr. E. A. Dean, and Dr. D. R. Russell for the use of their seismic processing and modeling programs. I extend thanks to Dr. M. R. Baker for technical advice and assistance in various areas. My appreciation goes to Don Roberts and Carlos Montana for their assistance on the HP mainframe.

I am grateful to my parents for their support and interest along the way. I especially thank my wife, Traci, for her understanding and encouragement.

Research funding during this study was provided by the University of Texas at El Paso Dept. of Geological Sciences and the United States Air Force Geophysical Laboratories.

This thesis was submitted to my committee on April 8, 1991.

ABSTRACT

Waveform modeling of radial component receiver functions from ANMO (Albuquerque, New Mexico Observatory) for three source back azimuths (northwest, southeast, and southwest) has been performed. The receiver functions were derived through source equalization deconvolution of merged long period and short period digital three component seismograms. Derived S-wave velocity models reflect dominantly intermediate composition granitic rock in the upper crust (above 15 km depth, Vs 3.5 km/sec) and middle crust (15-25 km depth, Vs 3.5-3.7 km/sec). Lower crustal shear velocities of approximately 3.75-3.85 km/sec may be representative of intermediate-to-mafic granulite facies, possibly together with previously underplated mafic material and other precursor crustal rocks. Shear wave attenuation between about 30-34 km may indicate a lower crustal partial melt zone. A 3-to-6 km thick interval is interpreted as a partial melt zone in the upper mantle leading into lessdepleted spinel peridotite (Vs = 4.25-4.35 km/sec) near 37 km. Inversion of EPT-ALQ interstation dispersion data for average S-wave velocity structure produces a satisfactory velocity tie to the middle and lower crust portions of the southwest back azimuth model.

TABLE OF CONTENTS

LIST OF TABLES

LIST OF FIGURES

INTRODUCTION

Receiver function analysis has become a widely accepted method of modeling shear wave velocity structure beneath isolated digital three-component seismic stations. With broadband data, this approach offers resolution of 1-to-3 km thick subsurface layers to depths near 60 km. Furthermore, analyzing off azimuth teleseismic arrivals recorded at a single station allows for modeling of structure within a maximum radius of about 35 km at these upper mantle depths. Therefore, determination of detailed crustal and upper mantle structure is possible through receiver function studies.

Previous seismic projects conducted in the Rio Grande rift have provided information on local crustal thickness, average crustal and upper mantle shear structure, and local P-wave velocity structure within the southern and central rift province. Therefore, in the first part of this thesis a receiver function study is presented in which shear velocity structure beneath the Albuquerque, New Mexico seismic observatory (ANMO) is modeled. ANMO is located on the eastern margin of the Albuquerque basin in the Rio Grande rift (Figure 1). The objectives of this study are to (1) determine whether or not local crustal anomalies exist, (2) constrain the shear structure of both the crust-mantle interface and the upper mantle, and (3) propose probable lower crustal and upper mantle compositions supported by the

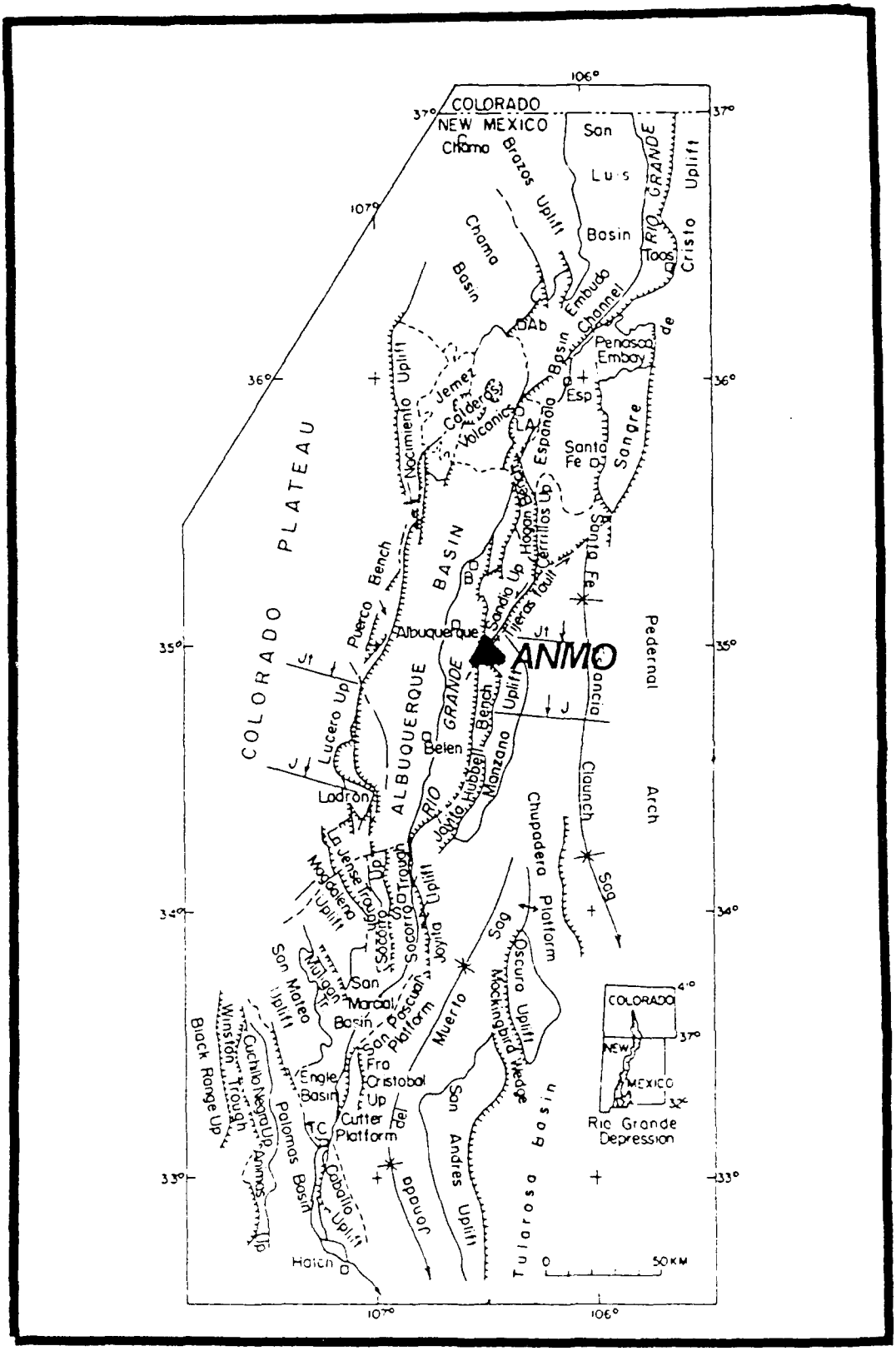

Figure 1. Rio Grande rift map depicting the Albuquerque basin and station ANMO (modified from Kelley, 1979).

geophysical information.

After selecting three-component seismograms of significant teleseismic events (Mb >=5.9) digitally recorded at ANMO during 1983 and 1984, these long and short period data are merged using the technique of Harvey and Choy (1981). By combining the long and short period spectra, records of broadband displacement (0.01 to above 1.0 Hz bandwidth) are attained, thus improving the sensitivity to P-to-S converted phases which occur within the crust and upper mantle. Receiver functions are then derived from these records using the processing methods of Langston (1979) and Owens (1984). The receiver functions are then modeled through both forward raytracing and inversion techniques to attain estimates of shear velocity structure along propagation paths.

The second phase of this thesis is a reinvestigation of the Rayleigh wave dispersion study originally conducted by Sinno and Keller (1986). In this previous study, an average S-wave velocity model for the Rio Grande rift axis was derived based on Rayleigh wave dispersion along the propagation path between the EPT (El Paso, Texas) and the ALQ (Albuquerque, New Mexico) seismic stations. The reanalysis of data used in the original study involves implementing phase matched filtering to improve estimates of group and phase velocity, and time variable filtering to smooth higher mode and multipath interference for interstation Green's

functions determined from multi-event data. Simultaneous fits of dispersion curves derived from filtered Green's functions are inverted for S-wave velocity structure using the inversion scheme of Russell (1980). Both biased and unbiased starting velocity models for the inversion are used, where the biased model is based on the teleseismic waveform modeling results.

This study presentation is organized into 4 chapters. Chapter 1 covers the geologic setting of the Rio Grande rift, and discusses the local geology for the Albuquerque basin area. Chapter 2 provides a summary of relevant past geophysical studies in the Rio Grande rift. A discussion of the theory and methods of both the receiver function and surface wave studies is made in Chapter 3. Lastly, Chapter 4 presents the processing, modeling, and interpretation results for both studies.

A summary of all computer code used in this project is given in the Appendix. This summary includes the code name, the name of the author, modifications made, and a brief description for each program.

CHAPTER 1: GEOLOGIC SETTING

RIO GRANDE RIFT

The Rio Grande rift is an extensional tectonic feature that extends from Leadville, Colorado to Presidio, Texas and Chihuahua, Mexico, a distance of more than 1000 miles (1600 km) (Figure 2) (Baldridge et al., 1984). Positioning of the rift features has been controlled locally by underlying crustal weaknesses formed during the many orogenic events that occurred from the late Precambrian to the early Cenozoic (Chapin, 1979; Ramberg and Smithson, 1975; Chapin and Seager, 1975). Following Laramide tectonism, the compressional stress field ended (Chapin, 1974) and subduction of the Farallon Plate beneath the North American Plate resulted in widespread calc-alkalic volcanism (Cook et al., 1979).

Recent studies (Morgan and Golombek, 1984; Seager et al., 1984; Morgan et al. 1986) demonstrate two phases of extension in the northern and southern rift. The first phase of Cenozoic extensional strain was initiated about 30 Ma. Crustal sagging along the developing rift formed broad, shallow basins containing mafic flows and volcanic ash beds intercalated with alluvial fill. Complex normal faulting further characterized this phase (Chapin, 1979). This transition from a subduction to an extensional regime is marked by a change from calc-alkalic to basaltic andesite magmatism. This phase was followed by a magmatic lull which

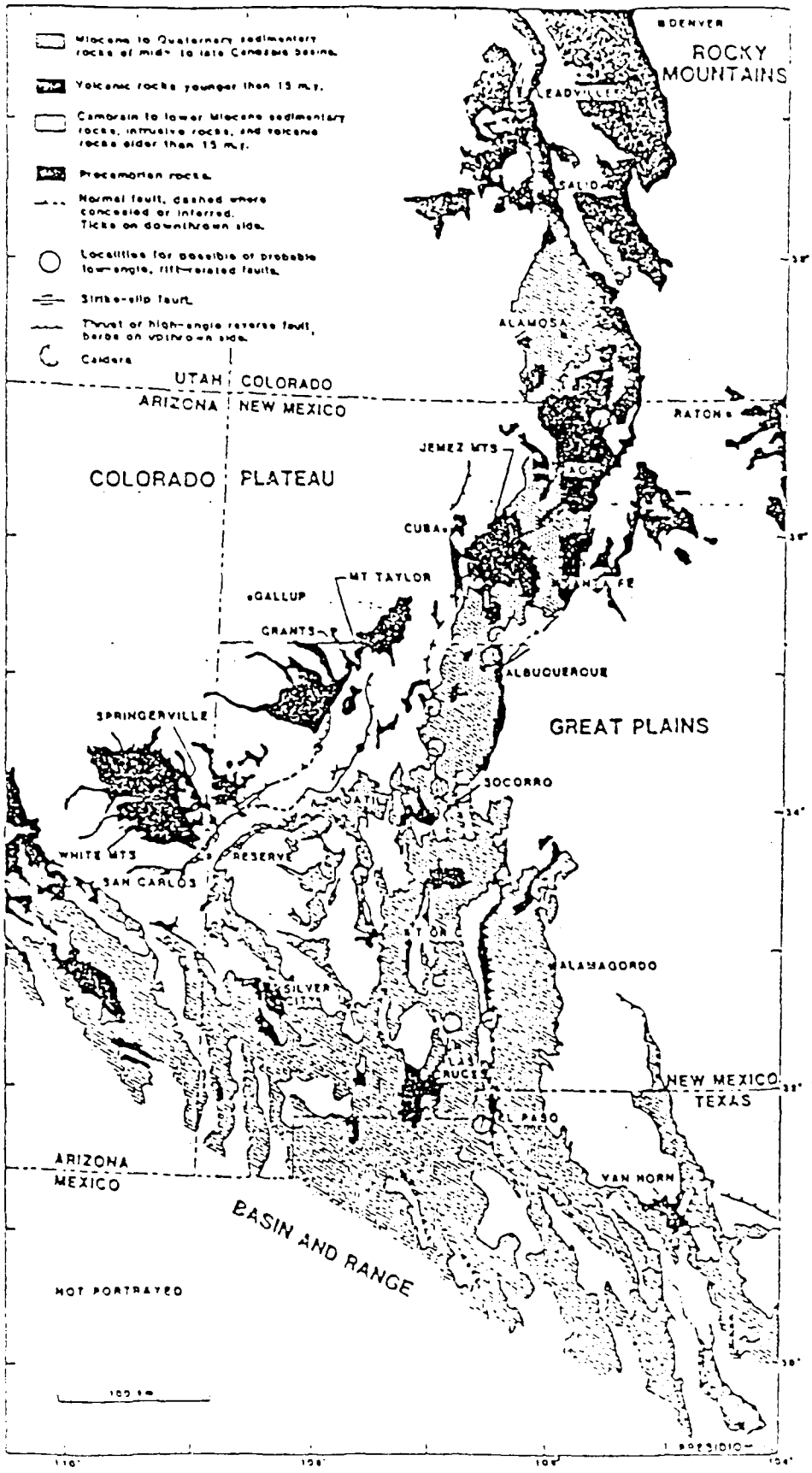

Figure 2. Tectonic map of the Rio Grande rift (modified from Baldridge et al., 1984).

lasted approximately between 26 Ma to 13 Ma in the southern rift and about 20 Ma to 13 Ma in the northern rift portion (Seager and Morgan, 1979).

The second phase of extension began about 13 Ma. At this point the crust became critically stretched, allowing partial melting in the upper mantle bulge beneath the rift. This period is marked by emplacement of alkali olivine basalts (Seager and Morgan, 1979). According to Chapin (1979), mantle upwelling has resulted in uplifts of about 1100 m since the middle Miocene in the Rocky Mountains and adjacent areas. Geophysical and regional uplift observations in the southern Rio Grande rift suggest that there is no direct cause and effect relationship between extension and subsidence as would be expected from crustal stretching models with a constant volume crust, so that underplating of material at the base of the crust is required to explain the regional elevation history (Keller et al., 1989). Bolson fill thicknesses of 1500 to 2500 m are common in basins of the southern rift (Seager and Morgan, 1979).

Modern activity in the rift is evidenced by abundant fault scarps cutting Pleistocene deposits, high heat flow, recent elevation changes, recent magma bodies and microseismicity (Chapin, 1979).

ALBUQUERQUE BASIN GEOLOGY

Figure 1 depicts the location of the Albuquerque basin.

This is one of the major sedimentary basins along the length of the Rio Grande rift, with approximate dimensions of 100 mi (160 km) north-south and 40 mi (64 km) east-west. The Precambrian crystalline basement rocks of the Sandia-Manzano-Los Pinos uplifts bound the basin on the eastern margin. The Albuquerque basin consists of two sub-basins. These are the North and South Graben Blocks shown in Figure 3. These basins reach maximum depths of about 24,000 ft (7317 m) in the North Graben and 23,000 ft (7012 m) in the South Graben. This basin fill is Tertiary continental clastic sedimentary rocks, overlying up to 11,000 ft (3354 m) of Paleozoic and Mesozoic pre-rift sedimentary basement. The Precambrian crystalline basement consists of 1300 Ma. granitic rocks and 1700 Ma. metamorphic rocks (Condie, 1976; Kelley, 1977; White, 1979) (Russell and Snelson, 1990).

CENTRAL RIFT MAGMATISM

Figure 4 shows the main volcanic fields of the central Rio Grande rift. Lavas from the northern Albuquerque-Belen basin consist of lower-alkali olivine tholeiite, similar to basalt from the northern rift. In the central Albuquerque-Belen basin, lavas are olivine tholeiite, basaltic andesite, and alkali olivine basalt of relatively restricted compositional range. Experimental data show that the olivine tholeiite basalt was derived from partial melting (15-20%) in the upper mantle, and that the alkali olivine basalt

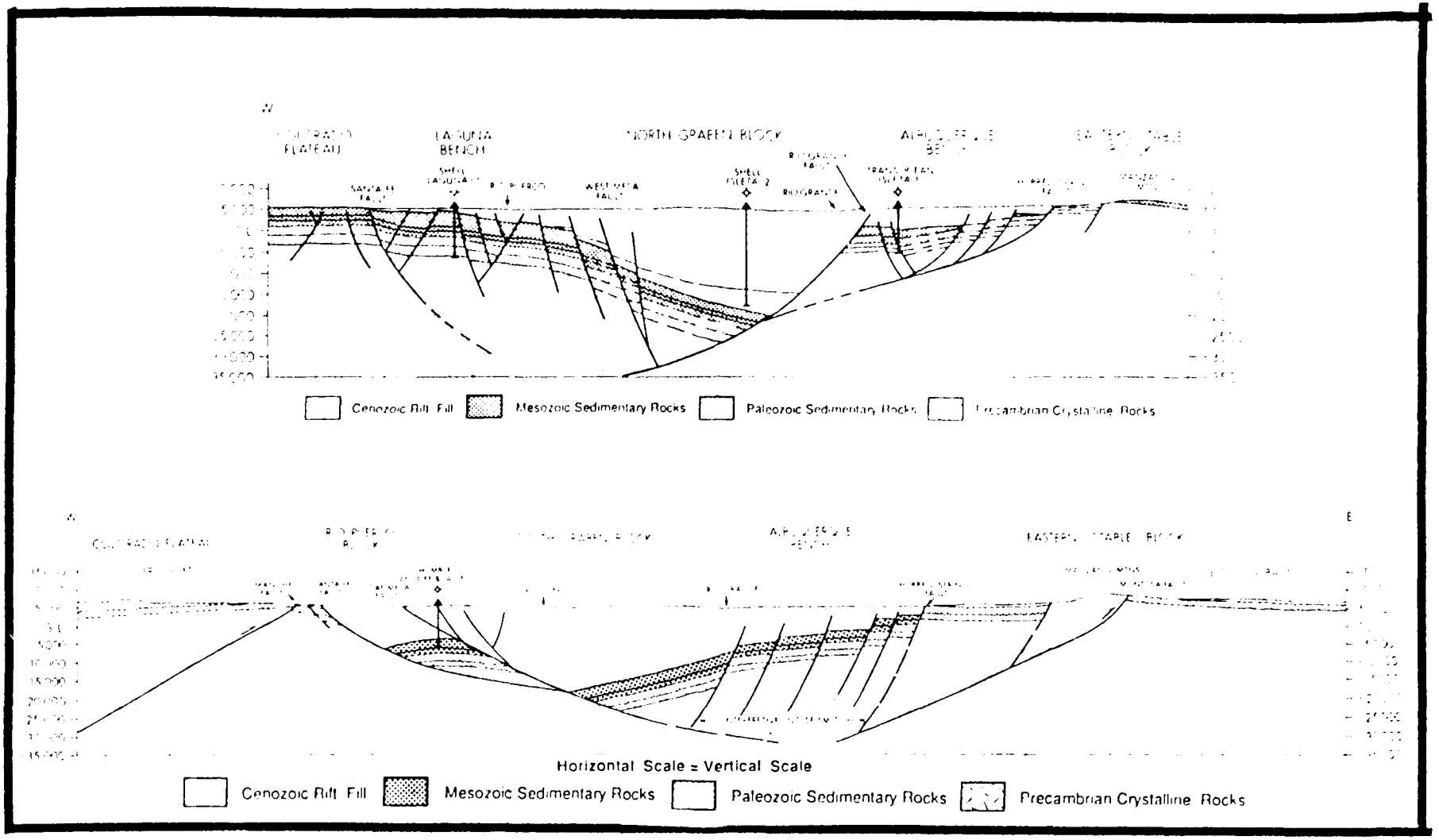

Figure 3. E-W geologic cross sections of the Albuquerque basin (from Russell and Snelson, 1990).

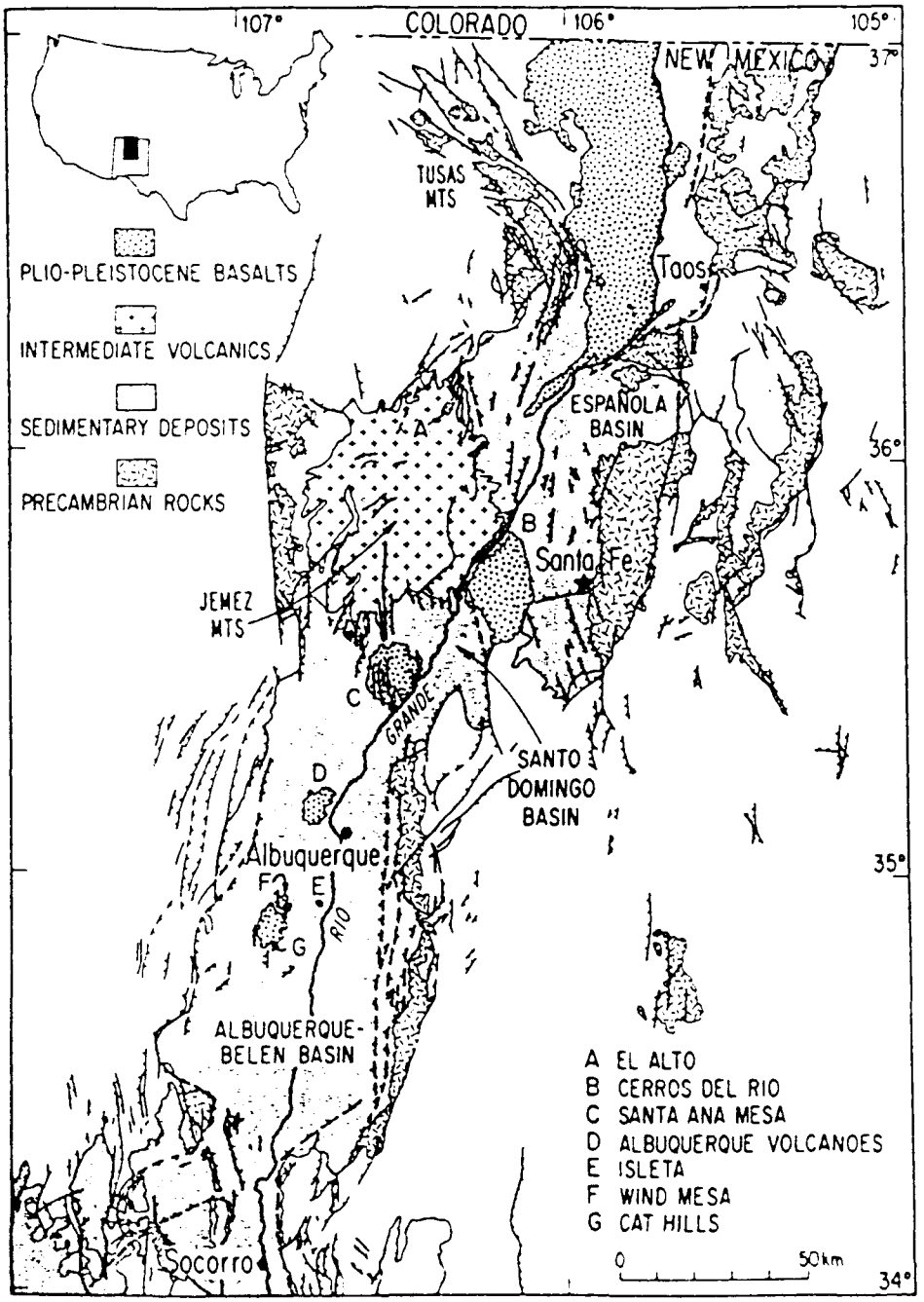

Figure 4. Main volcanic fields of the central Rio Grande rift (from Baldridge, 1979).

originated from a lesser degree of partial melting at 50-70 km depth (Baldridge, 1979). Perry et al. (1988) suggest that shifts in composition from alkali basalts to tholeiites was due to a significant shallowing in the zone of magma genesis following a thermal conversion of lithospheric mantle to asthenosphere between 8 and 4 Ma.

CHAPTER 2: PREVIOUS GEOPHYSICS

Gravity, seismic refraction, seismic reflection, surface wave dispersion, teleseismic travel-time delay, and heat flow studies have been conducted within the Rio Grande rift. Such measurements have evidenced crustal thinning, anomalously low upper mantle density, thick accumulations of sediment fill in rift basins, and seismic anomalies indicative of intracrustal magma bodies.

Rio Grande rift gravity modelling efforts have revealed three main components in the gravity field (Callender, et al. 1989). A long wavelength gravity low is interpreted to be due to lithospheric thinning (e.g., Bridwell, 1976; Ander, 1981). An axial gravity high component is demonstrated to be due to crustal thinning (Daggett et al. 1986, Decker and Smithson, 1975; Cordell, 1976, 1978; Ramberg et al., 1978). This anomaly narrows from south to north, indicating rift extension also decreases from south to north (Cordell, 1982). Lastly, a series of short wavelength gravity lows are due to thick sediment accumulations in rift basins (Callender, et al. 1989).

Seismic refraction studies within the rift (Table 1) include the works of Olsen et al. (1979) and Sinno et al. (1986) (published results of Sinno, 1984). The 1979 study involved an axial profile in the central to northern rift segment. The 1986 study was conducted in the southern Rio

TABLE 1 (From Sinno and Keller, 1986).

Average P Wave and S Wave Models and Calculated Values for Poisson's Ratio

Axial Model (*Sinno et al.*)		Axial Model (*Olsen et al.*, 1979)		Average P Wave Model		Surface Wave Model*	Poisson's Ratio†
Thickness, km/s	P velocity, km	Thickness, km	P velocity, km/s	Thickness, km	P velocity, km/s	S velocity km/s	
1.4	4.28	3.20	4.30	2.12	4.29	1.74 (SD 0.02)	—
11.19	5.92						
7.10	6.06	18.20	6.00	18.25	5.99	3.49 (SD 0.39)	0.24
12.09	6.55	12.30	6.40	12.20	6.48	3.64 (SD 0.54)	0.27
31.42	7.94	*33.70*	7.60	*32.57*	7.77	4.25 (SD 0.02)	0.29

SD is standard deviation. Italicized values indicate total crustal thickness.

* Determined by spectral whitening inverse.

† Determined from combined analysis of surface wave and refraction results.

Grande rift (Figure 5). Olsen et al. (1979) determined an upper crustal P-wave velocity of 6.0 km/sec, 6.4 km/sec for the lower crust, and an upper mantle velocity (Pn) of 7.6 km/sec, with a crustal thickness of 34 km. P-wave velocities of 5.92 km/sec for the upper crust, 6.06 for the mid-crust, 6.55 km/sec for the lower crust, and 7.7 km/sec (Pn) for the upper mantle were published by Sinno et al. (1986). Crustal thickness was determined to be 28 km near the southern New Mexico border and 32 km at the extreme northern end of the profile (approximately 33.5 degrees N latitude). This thinned crust distinguishes the rift from adjacent the Colorado Plateau, Rocky Mountains, and Great Plains provinces. Furthermore, the lower observed Pn velocity distinguishes the rift from the adjacent Basin and Range province.

Brown et al. (1979,1980) reported results of seismic reflection surveys conducted within the rift by the Consortium for Continental Reflection Profiling (COCORP) (Figure 6). A strong midcrustal reflector correlates with the tabular magma body beneath the Socorro, New Mexico region previously detected through local microearthquake studies by Sanford et al. (1973) and Brocher (1981b) (de Voogd et al., 1986). A discontinuous reflection at 11-12 sec agrees with the placement of the M-discontinuity derived from seismic refraction by Olsen et al. (1979) (Callendar et al., 1989). The crust-mantle transition zone (between 33 to 38 km depth,

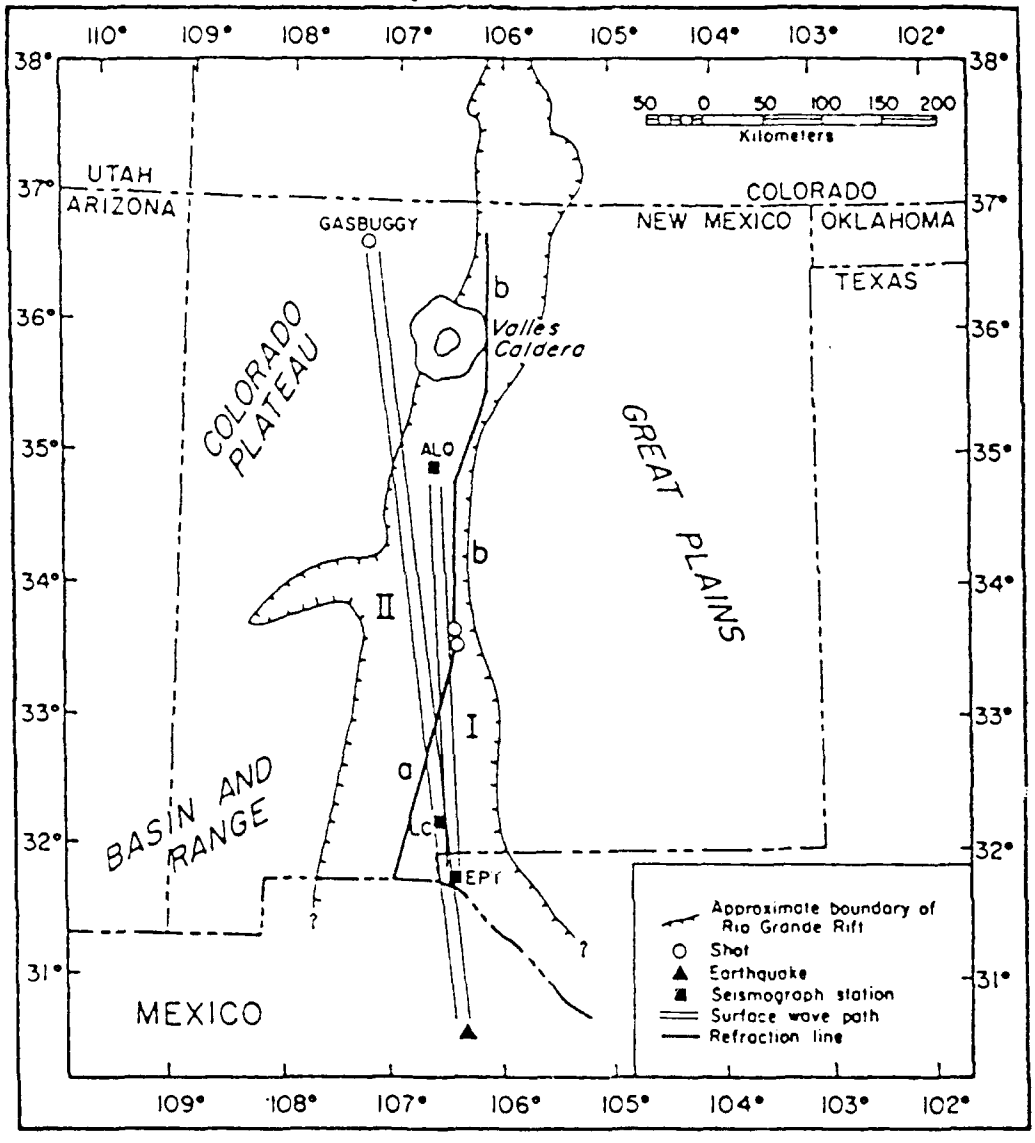

Figure 5. Map showing previous surface wave and refraction work: EPT-ALQ surface wave path (Sinno and Keller, 1986 study) and refraction lines (a = Sinno and Keller, 1986 axial line; b = Olsen et al., 1979 axial line) (From Sinno and Keller, 1986).

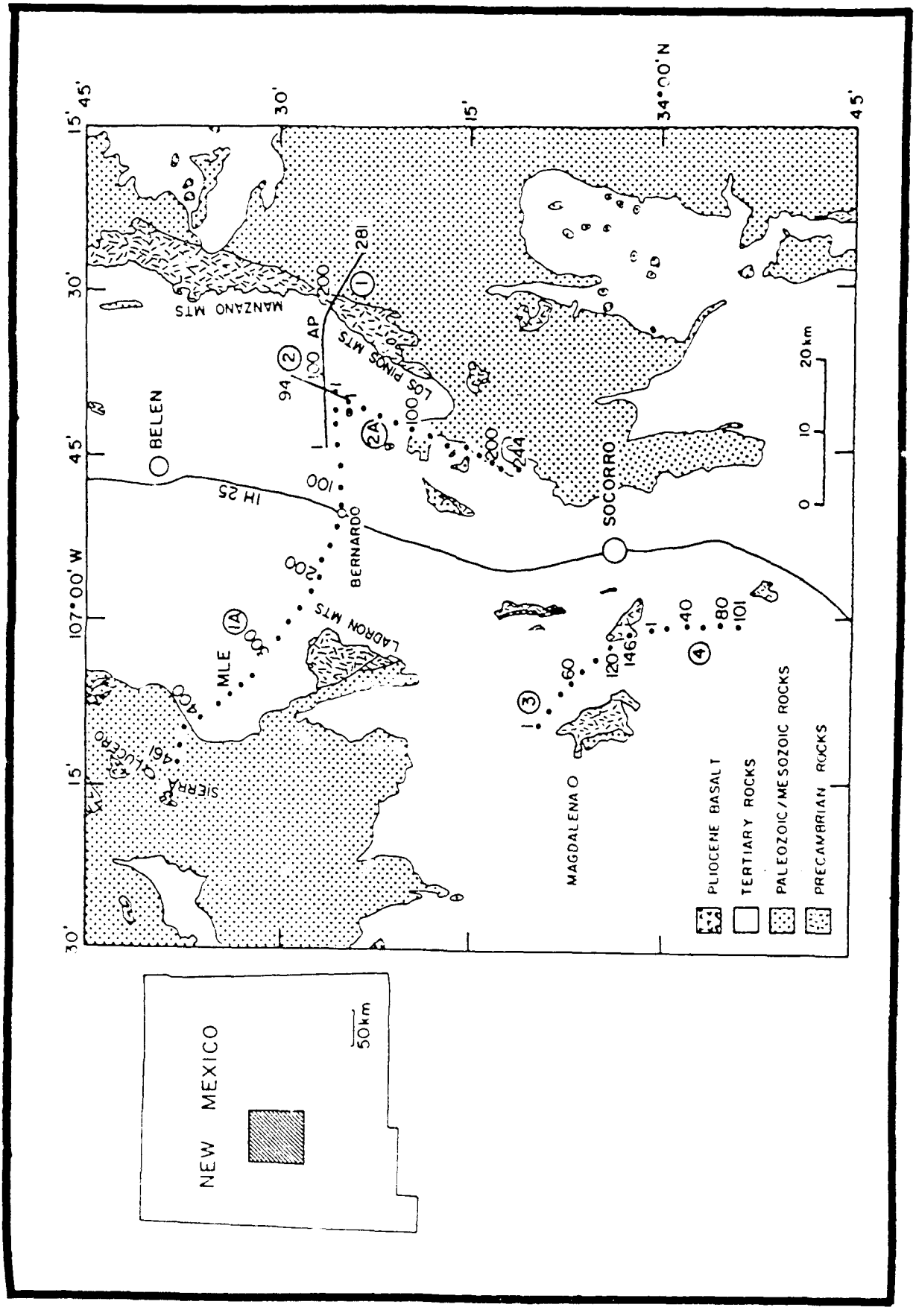

Figure 6. Map showing COCORP reflection lines. AP = Abo Pass line, MLE = Monte Largo embayment line (from Brown et al., 1979).

according to Toppozada and Sanford, 1976, and Olsen et al., 1979) was revealed to be a complex zone varying both laterally and vertically on a scale of a few kilometers, as evidenced by discontinuous reflectors, some of which have a layered character (Brown et al., 1979).

Average S-wave velocity models for propagation paths along the rift axis and across the central rift have been derived from Rayleigh wave studies. These studies include Sinno and Keller (1986), and Schlue et al. (1986).

Sinno and Keller (1986), using seismic records from 5 earthquakes located in the eastern Pacific between 1977 and 1982, analyzed Rayleigh wave dispersion between the EPT (El Paso, Texas) and ALQ seismic stations (Figure 5). Group dispersion curves were determined using the moving window technique (Landisman et al., 1969) and phase dispersion curves were determined using the cross-multiplication technique (Bloch and Hales, 1968). Group and phase velocities were inverted simultaneously using a first order difference inversion scheme (Russell, 1980; Braile and Keller, 1975) to determine an earth model which fit both data sets. Next, P-wave velocities derived from seismic refraction (Sinno et al., 1986) were used to constrain a surface wave velocity inversion using the spectral whitening technique. These results along with those from the refraction studies appear in Table 1. Here, an average crustal thickness of 32 km along the rift axis with an

average upper mantle S-wave velocity of 4.25 km/s is indicated. Poisson ratios calculated based on these velocity data indicate that lithospheric rigidity in the southern rift decreases with depth, indicating higher than normal upper mantle temperatures (Sinno and Keller, 1986).

Schlue et al. (1986) determined an upper crustal S-wave velocity model for the Albuquerque-Belen Basin for the path between stations RKO and TMG shown in Figure 7. Three Nevada Test Site (NTS) events recorded between 1983 and 1984 were used. Fundamental mode Rayleigh wave phase velocities were obtained and inverted to yield an S-wave velocity model for the upper 20 km of the basin. This model contained two low velocity zones near 6 km depth and 18 km depth. The velocity reversal near 18 km depth was considered due to the thermal effects of the midcrustal magma body previously identified through earthquake studies by Sanford et al. (1973). The low-velocity zone detected at near 6 km depth, based on high heat flow values of 110 mW/m along the rift axis, was believed to be possibly due to the effects of an upper crustal magma body.

Davis et al. (1984) analyzed P-wave travel-time delay data from 40 teleseismic events recorded at 20 seismic stations between Moab, Utah and Odessa, Texas between December 1982 and January, 1983. The recording station array crossed the Rio Grande rift axis (south of Santal Fe, New Mexico) at a 45 degree angle along an azimuth where

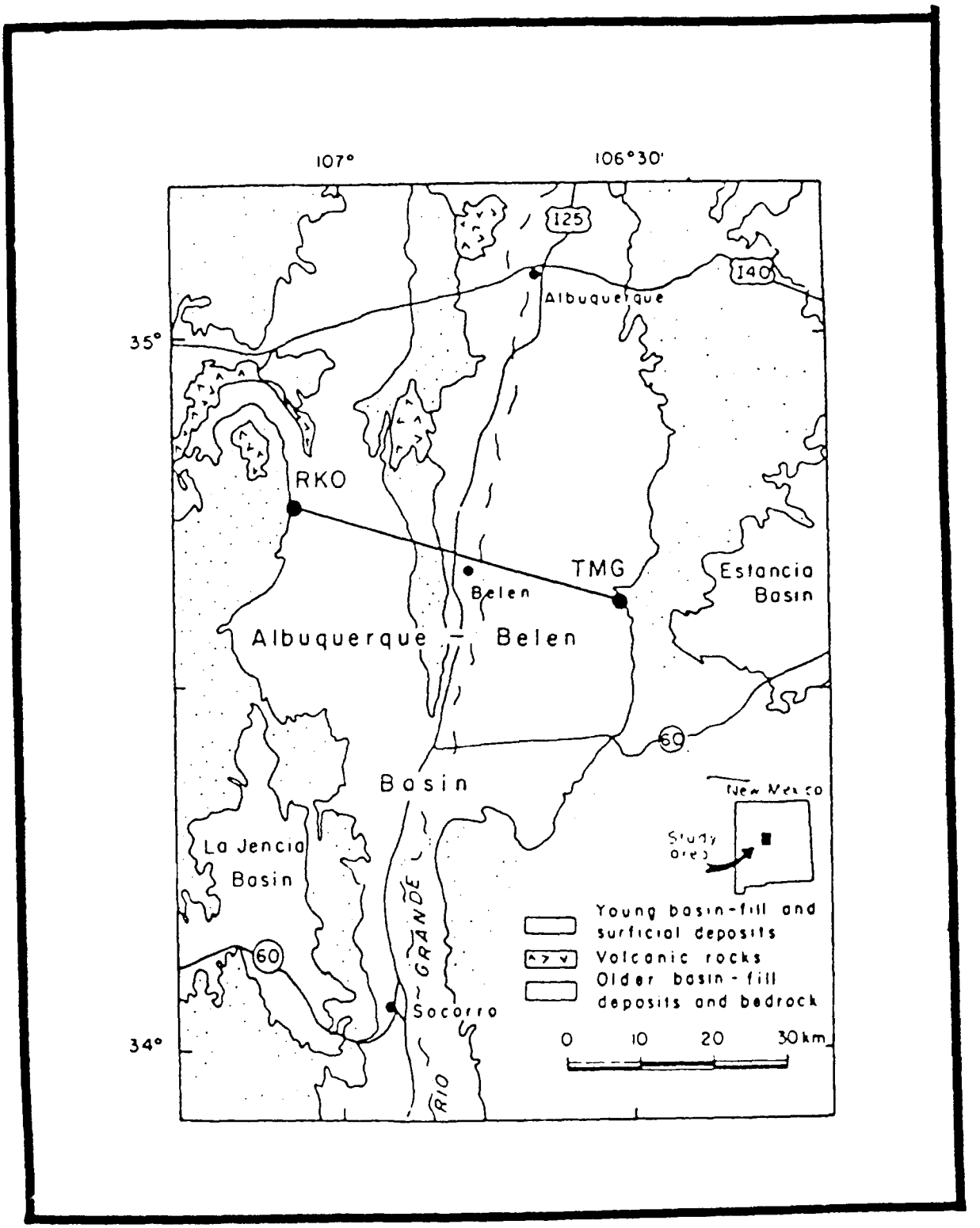

Figure 7. Map showing RKO-TMG surface wave path (from Schlue et al., 1986).

teleseismic arrivals frequently occur (Figure 8). The study found maximum P-wave delays of 1.5 sec for the central rift. These delays were interpreted to be caused by an upper mantle low-velocity zone within the rift boundary in the depth range 70-100 km, with a velocity contrast of -8% (Davis et al., 1984).

Estimates of heat flow from a deep petroleum test in the Albuquerque-Belen basin have been made by Reiter et al. (1986). A regional heat flow of $\simeq$ 77 mW/m^2 along with a NE-SW trend of higher heat flow (92-110 mW/m^2) across the region were determined. The background heat flow is consistent with simple models of crustal thinning. Higher heat flow components are believed due mainly to hydrothermal fluids (largely groundwaters but possibly magma in some areas) transporting heat upward along crustal fracture zones (Reiter et al., 1986). Heat flow for the entire rift region has been mapped by Seager and Morgan (1979) (Figure 9).

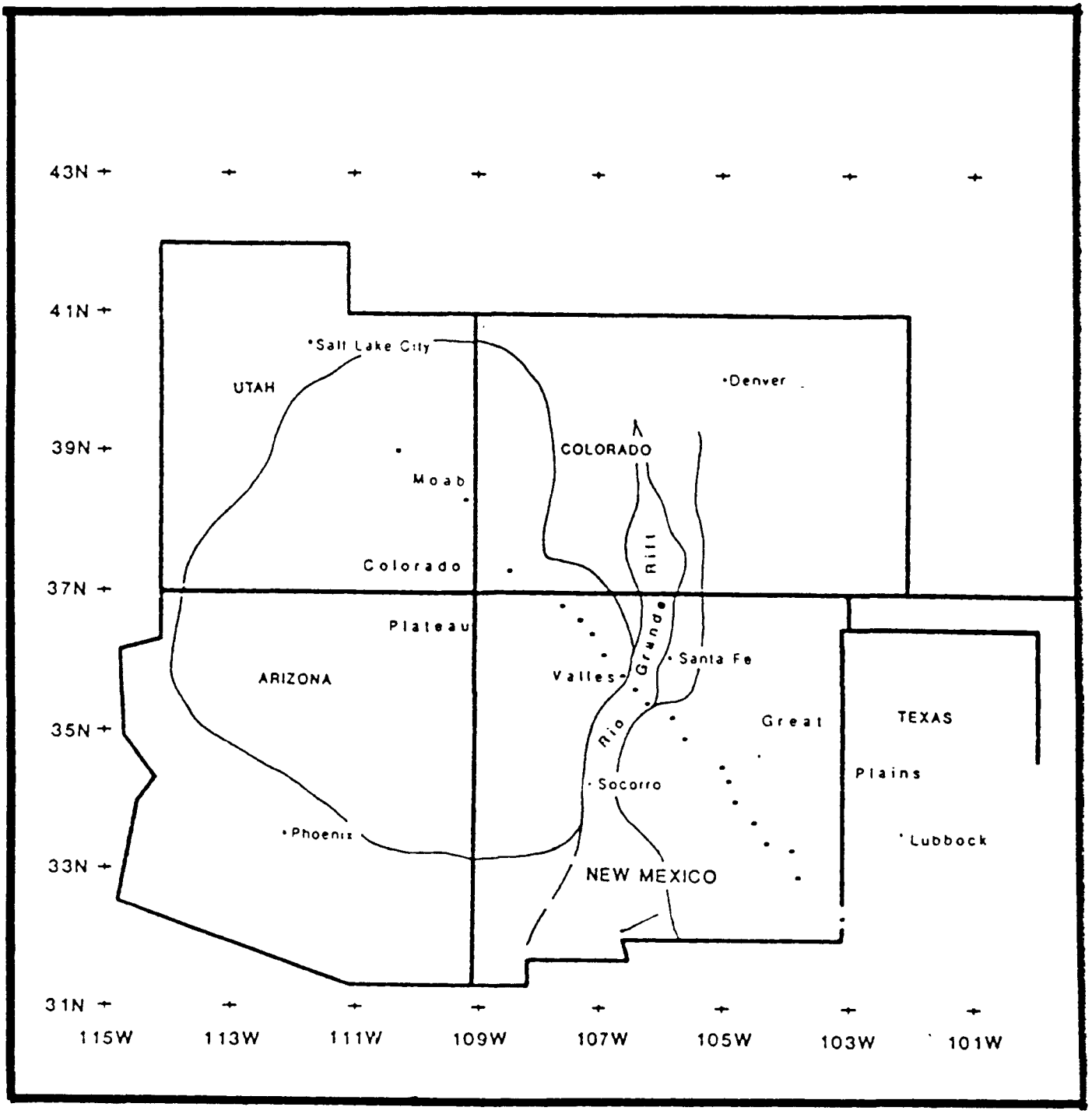

Figure 8. Portable seismic recording station locations for teleseismic P-delay study (from Davis et al., 1984).

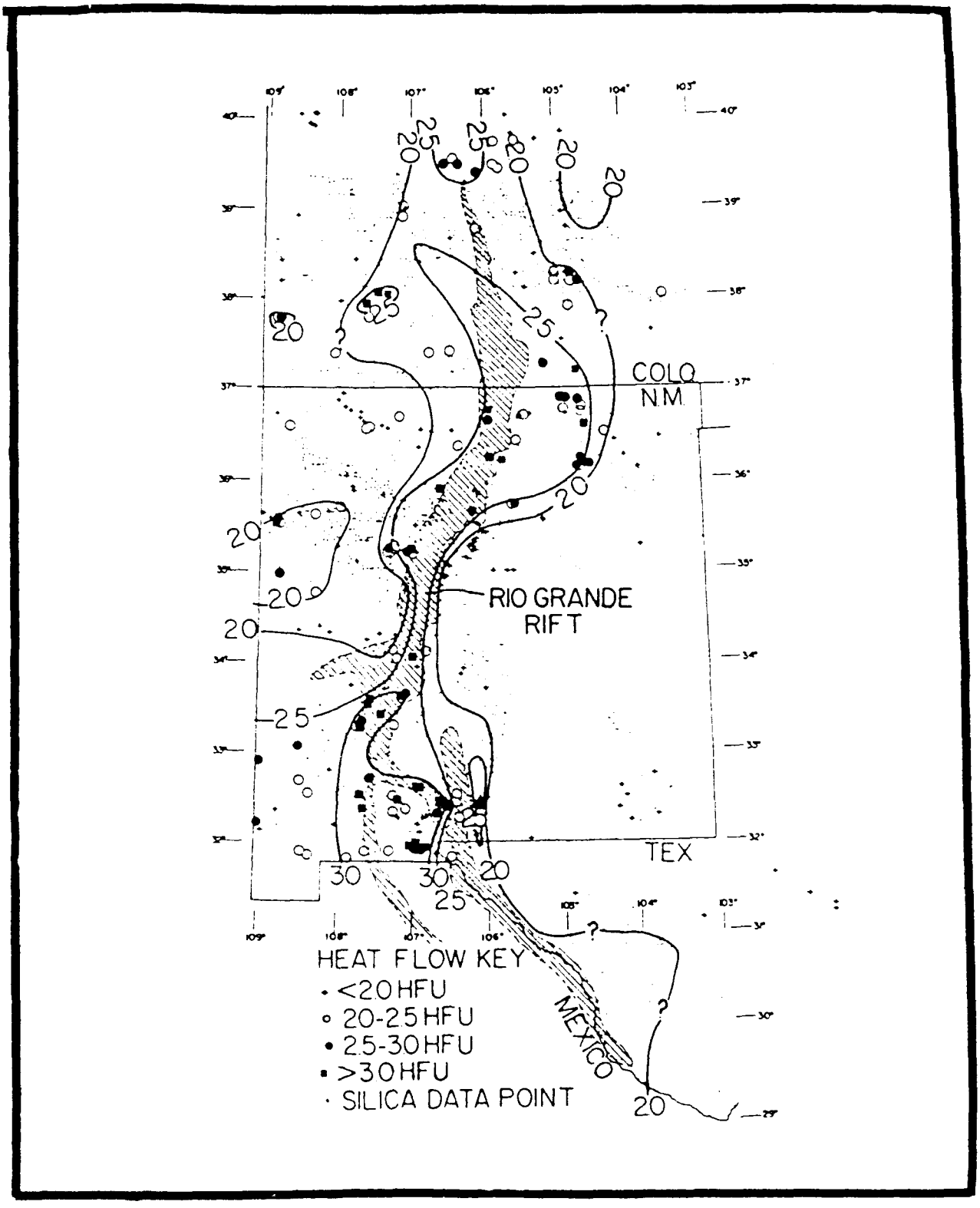

Figure 9. Heat flow map of the Rio Grande rift region (from Seager and Morgan, 1979, and Swanberg, 1979).

CHAPTER 3: THEORY AND METHODS

This thesis involves two seismic investigations in the Rio Grande rift province: a receiver function study using the ANMO seismic station, and a surface wave dispersion study reanalysis utilizing data from the EPT and ALQ seismic observatories. First, the methods of receiver function analysis as applied here will be discussed. Then a discussion of the concepts behind the surface wave processing and modeling will be presented.

RECEIVER FUNCTION STUDIES

The analysis of converted phases in teleseismic waveforms for determination of local earth structure beneath an isolated receiver has been well documented (e.g. Bath and Stefansson, 1966; Burdick and Langston, 1977; Owens, 1984, 1988). Early studies attempted to resolve earth structure beneath long-period WWSSN (Worldwide Standardized Seismograph Network) stations. The limited resolution of long-period data allowed only for the determination of simple crustal models. Owens (1984) first demonstrated the effectiveness of using broadband digitally recorded data to resolve detailed crustal and upper mantle structure.

This present study is a departure from previous experiments in that ANMO lacks broadband recording instruments. This requires beginning with the digitally

recorded three-component long and short period seismograms from ANMO, and merging each corresponding long and short period component together into a composite record with broadband frequency content. Then, proceeding as usual, the merged N-S and E-W component seismograms are rotated with respect to their source back azimuth, and source equalization deconvolution (Langston, 1979) is applied to isolate receiver functions from the records of total horizontal (radial and tangential) displacement. These receiver functions are then gathered into stacking suites based on common source distance and back azimuth. Each suite is then stacked to yield a mean receiver function for the particular back azimuth. Synthetic waveform matching of the mean radial component receiver functions is then performed in both forward and inverse modelling schemes. Langston's 3-D raytracing method (1979) is implemented in both approaches, where structure beneath the receiver is parameterized with a stack of planar, homogenous layers of finite thickness and arbitrary strike and dip (horizontal layers are used for this study). The objective is to reach an estimate of the shear velocity distribution beneath the seismic station by attaining a best-fit waveform match between the observed and synthetic waveforms, the latter being the result of raytracing through the parameterized earth model. The final earth model yields the best waveform match, and is a modified version of a starting model into which all available a priori information

has been incorporated.

DATA SELECTION

Following the criteria outlined by Owens (1984), the following requirements are met by the chosen data set: (1) Only teleseismic events (distance from the source epicenter to the receiver is between 35-95 degrees) are used. This guarantees that the arriving energy will impinge steeply beneath the receiver structure, thereby generating an impulsive vertical response within the structure. (2) To insure significant energy reaches the receiver for effective modeling, only events with Mb >= 5.9 are used for sources.

PRELIMINARY DATA PROCESSING

Prior to receiver function calculation, initial processing steps must be performed on the raw digital data. For the case of digitally recorded three-component WWSSN long and short period data, the following applies: (1) Using the technique of Harvey and Choy (1981), the long and short period data are merged together. As a result, the merged records have a bandwidth from 0.01 Hz to above 1.0 Hz. This significantly yields the same sensitivity to locally converted P-to-S phases as broadband recording. (2) A rotation is applied to the merged horizontal component (N-S and E-W) records in order to determine true radial and

tangential receiver displacement with respect to the particular teleseismic source back azimuth.

Merging the digital data involves first aligning the long and short period records in time. Originally, the long period seismogram is digitally sampled at 1 Hz, and the short period seismogram at 20 Hz. Before further processing, the long period record is resampled at 20 Hz. Given the difference in the long and short period seismometer responses (Figure 10), these effects must be removed prior to merging. Therefore, the long and short period seismograms are separately Fourier transformed, and the instrument frequency responses are removed in a divisional deconvolution. The effects of rapid instrument gain are removed before merging by applying a low-pass filter to the long period instrument corrected spectra and a high-pass filter to the corrected short period spectra (Figure 11). An inverse Fourier transform returns the long and short period time series, free of instrument effects. These are then summed to form the resultant broadband displacement seismograms (Harvey and Choy, 1981).

Figure 12 shows the original N-S long period and short period records of a particular Honshu teleseism together with the corresponding merged broadband record used in this study. The inclusion of the long period response makes possible the extraction of velocity information at lower crustal to subMoho depths.

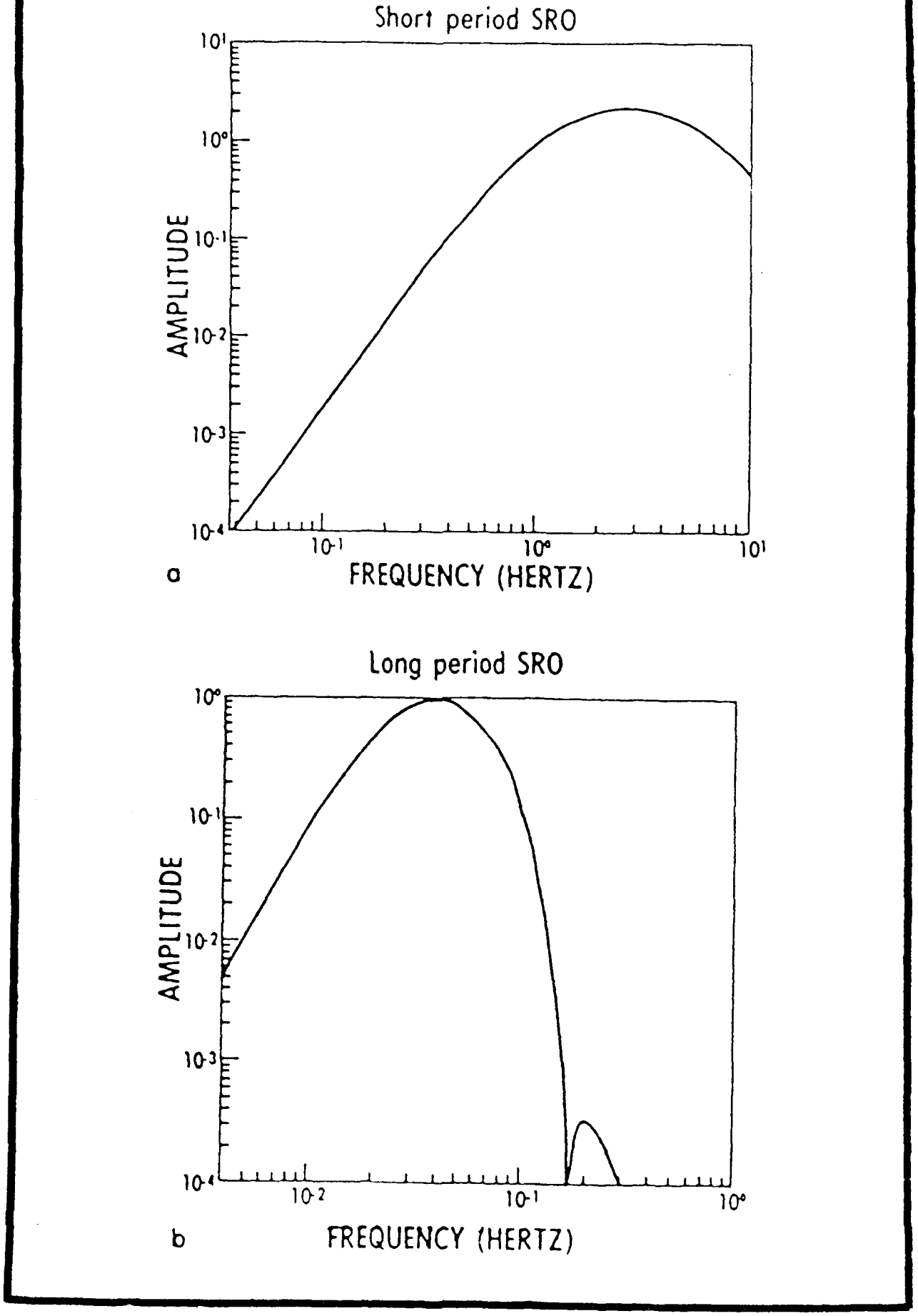

Figure 10. Station ANMO (a) short period, and (b) long period SRO instrument responses (from Harvey and Choy, 1981).

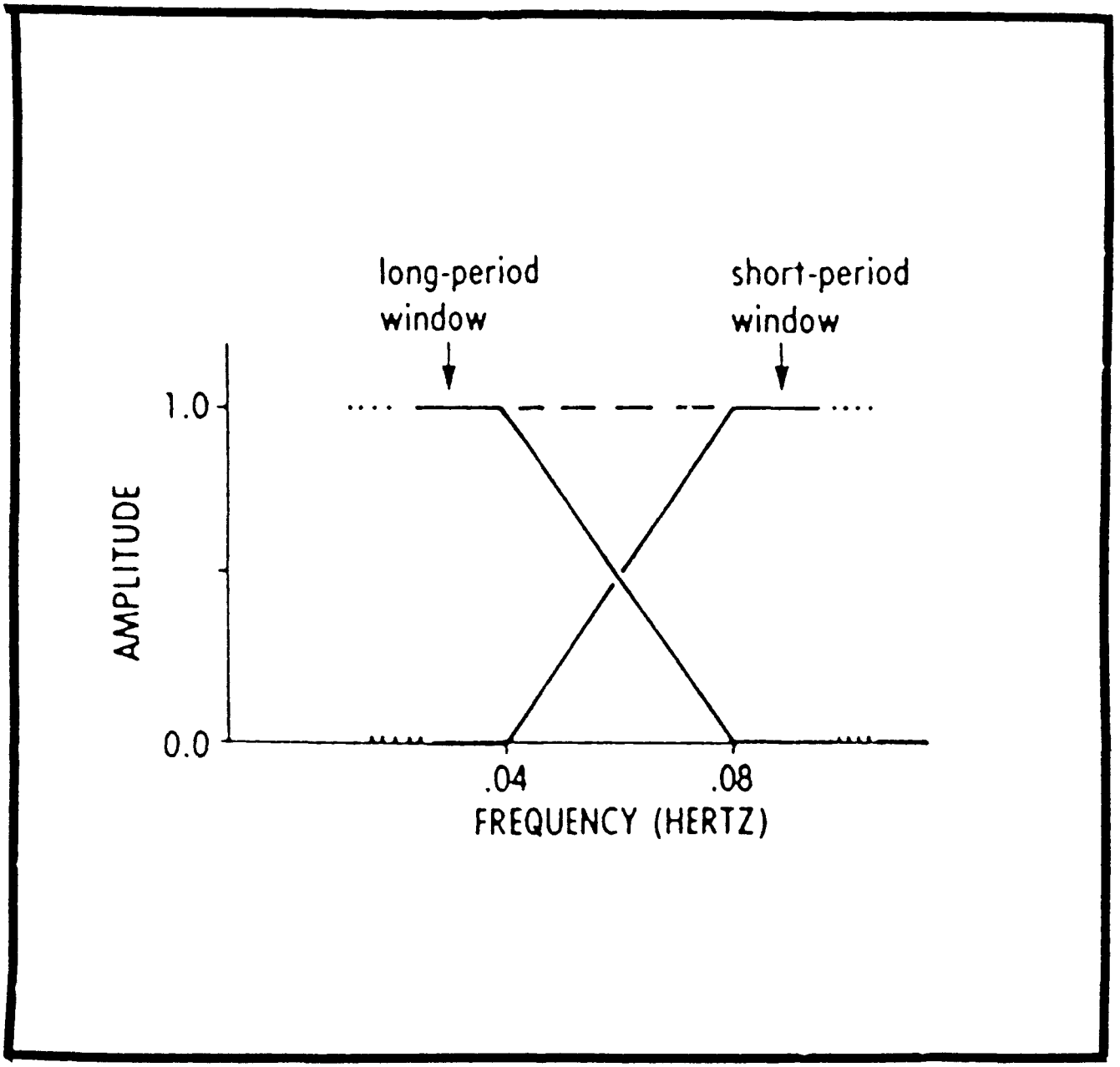

Figure 11. Illustration of frequency cutoffs for low-pass (long period) and high-pass (short period) filters which are applied to ANMO digital data prior to merging (from Harvey and Choy, 1981).

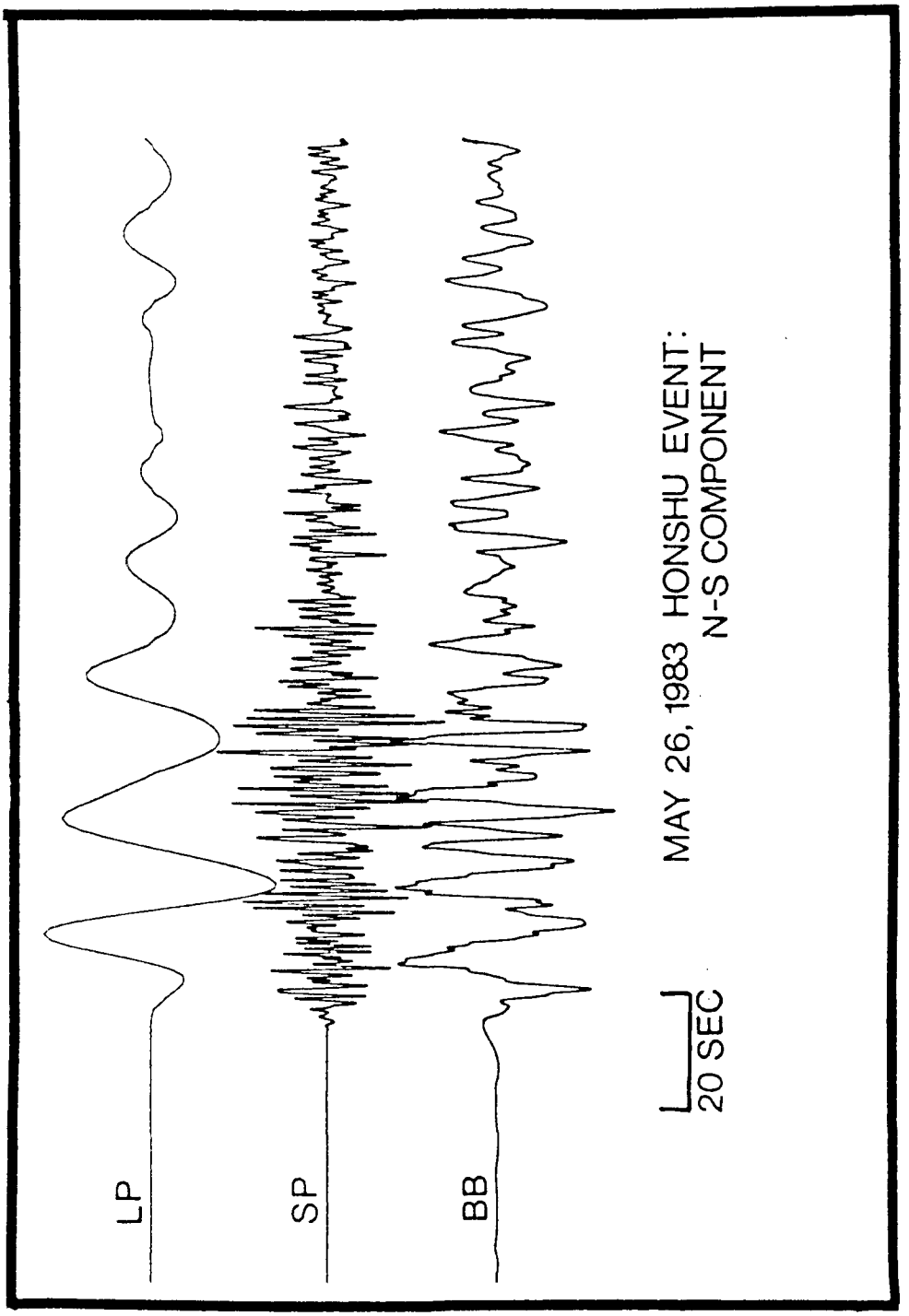

Figure 12. Example of data merging. LP (long period) and SP (short period) displacement records are merged to produce the BB (broadband) seismogram.

At this point in the analysis, the data set consists of three-component (N-S, E-W, and Z) broadband digital seismic records. The next step involves rotating the horizontal component seismograms with respect to the particular source back azimuth. The rotated output consists of true radial and tangential displacement seismograms for a propagation direction. Once rotated, source equalization can be performed on the three-component data to determine the receiver functions.

RECEIVER FUNCTION CALCULATION

Following the approach used by Langston (1979), the total seismograms, D(t), recorded at the three-component digital station, can be expressed in the time domain as convolutions of the impulse response of the recording instrument, I(t) the source function, S(t), and the response of the local earth structure, E(t):

$$Dv(t) = I(t) * S(t) * Ev(t),$$
$$Dr(t) = I(t) * S(t) * Er(t),$$
$$Dt(t) = I(t) * S(t) * Et(t),$$

where v, r, and t subscripts denote vertical, radial, and tangential components of motion, respectively. Determination of the receiver function requires the removal of the unwanted source and instrument effects to reveal the response of

structure beneath the receiver. Given that instrument responses are removed during the data merging process, then the broadband total displacement seismograms are expressed as:

$$Dv(t) = S(t) * Ev(t),$$
$$Dr(t) = S(t) * Er(t),$$
$$Dt(t) = S(t) * Et(t),$$

with the source function and earth response denoted as usual. Further development here will also exclude the instrument response term.

Assuming that the vertical component earth response for teleseismic events will be dominated by mainly a large direct P arrival followed only by minor crustal reverberations and phase conversions (Langston, 1979), the earth response for the vertical component of motion can be approximated by the Dirac delta function:

$$Ev(t) \simeq \quad (t).$$

This implies that the total vertical component seismogram can be represented as

$$Dv(t) \simeq S(t),$$

meaning that the source effects which should be removed are contained here. This allows for the source equalization deconvolution scheme developed by Langston (1979), in which a frequency domain deconvolution is applied to reveal the radial and tangential component receiver functions:

$$Er(w) = Dr(w) / (S(w)) \simeq Dr(w) / Dv(w),$$
$$Et(w) = Dt(w) / (S(w)) \simeq Dt(w) / Dv(w).$$

While stable for noise-free data, this divisional deconvolution becomes unstable when applied to band-limited seismograms containing noise (Owens, 1984). Therefore, a minimum allowable amplitude level (waterlevel) is applied to fill spectral troughs. Lastly, smoothing with a Gaussian function is performed. The final frequency domain expression for the radial receiver function is

$$Er(w) = [Dr(w)\overline{Dv}(w)/phi(w)]G(w),$$

where

$$phi(w) = \max\{Dv(w)\overline{Dv}(w),\ c \cdot \max[Dv(w)\overline{Dv}(w)]\};$$
$$c = \text{waterlevel parameter};$$
$$G(w) = \exp(-w^2/4a^2) = \text{Gaussian smoother}.$$

Inverse transformation of the radial and tangential spectra

yield the time domain receiver functions, Er(t) and Et(t).

In the above expression for G(w), parameter a controls the width of the Gaussian pulse, in turn controlling the degree to which high frequency noise is reduced. For the frequency content of broadband receiver functions, a = 5 is an appropriate selection (Owens, 1984). Including a waterlevel parameter (c > 0) reduces noise in the receiver function due to spectral troughs and high frequency noise present in the vertical component, but a reduction in relative arrival time resolution can be expected with increased c magnitude. Furthermore, increased c values lead to truncation of higher frequencies in the vertical component amplitude spectrum, which can introduce sidelobes into the receiver functions. An optimum tradeoff between these effects must be made, which the processor must determine by trial and error. Appropriate values of c fall in the range between 0.0001 to 1.0. The deconvolution should be performed over this range, and the optimum result chosen (Owens, 1984).

STACKING RECEIVER FUNCTIONS

Quality receiver functions are gathered into stacking suites based on relative origin distance and back azimuth and stacked to increase signal to noise ratio, and to provide an average estimate of crustal and upper mantle response along a particular propagation path. The range in distance variation within a single stacking suite should be less than 15 degrees

for events with distance >= 70 degrees, and less than 10 degrees for closer events. Back azimuthal variation should be kept to less than 20 degrees. Determination of best estimate receiver functions for a range of back azimuths (controlled by the natural distribution of teleseismic sources, mainly NW, SE, and SW back azimuths for this study) allows for modeling of horizontal variations in shear wave velocity structure beneath the station (Owens, 1984).

MODELING RECEIVER FUNCTIONS

The 3-D raytracing method of Langston (1977) requires the assumption that earth structure beneath the three-component receiver can be modeled as a stack of homogeneous, planar layers of varying thickness and dip orientation overlying a half-space. Furthermore, each layer is parameterized with an S-wave velocity, a P-wave velocity, and a density. Since teleseismic sources are used, plane waves are assumed.

P-waves arriving from teleseismic sources impinge at steep angles of incidence beneath the layered stack (Figure 13). As the energy propagates upward through the layers, P-to-S conversions occur due to velocity contrasts at layer interfaces. These shear waves are recorded on the horizontal component seismograms within 50 seconds following the arrival of the direct P phase for interfaces up to 80 km depth (Owens, 1984). Langston's method assumes all multiples are

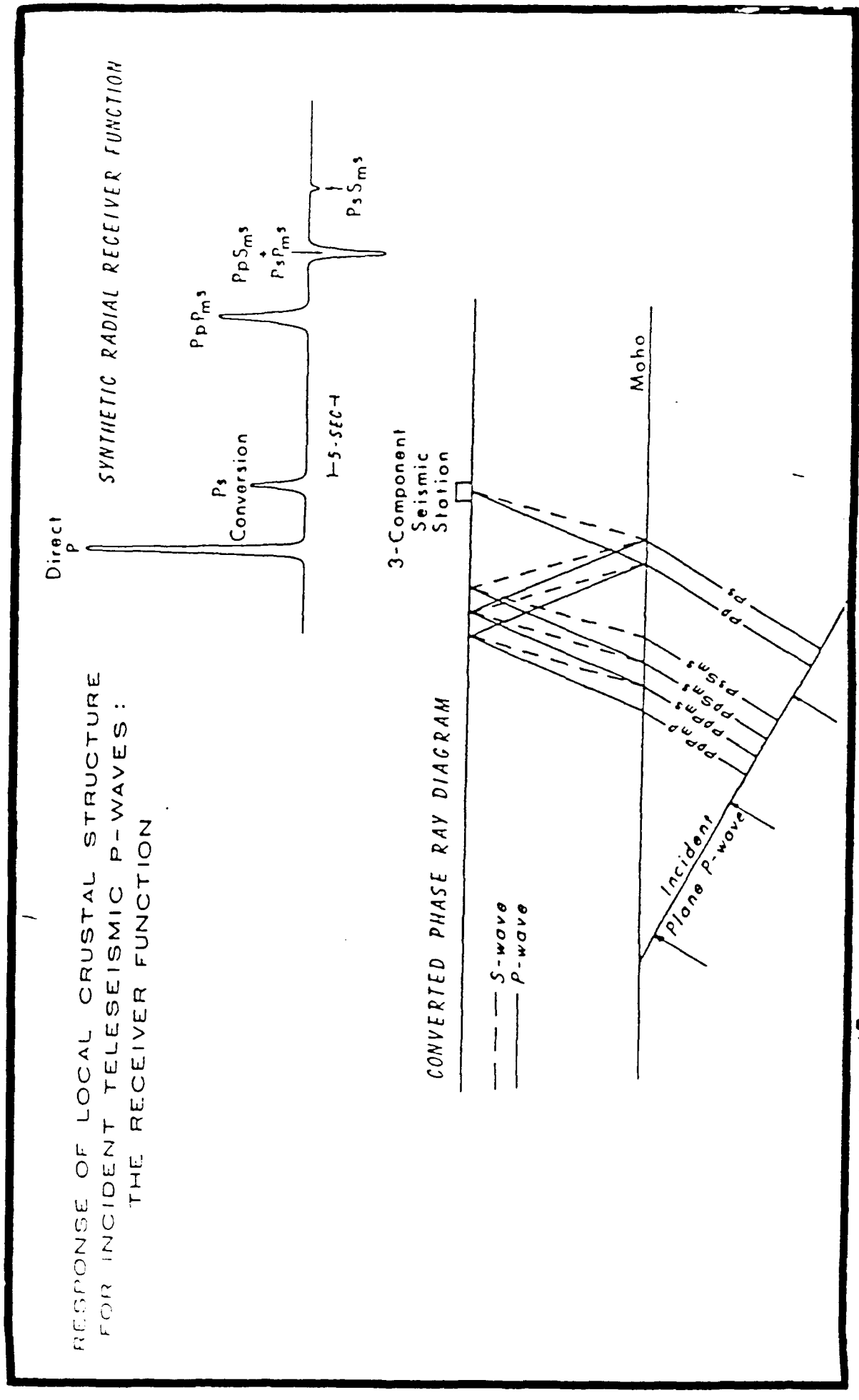

Figure 13. Schematic ray diagram and synthetic receiver function for simple crust (from Owens, 1984).

between the free surface and layer interfaces within the stack; hence, no intralayer multiples can be included. The notation of Bath and Stefansson (1966) is used to name specific phases produced: (1) Incident waves at the bottom of a layered stack are represented by capital letters (P or S). (2) Upgoing waves in the layered stack are represented by lower case letters (p or s). (3) Downgoing waves in the layers (reflections from the free surface) are represented by capital letters.
(4) Reflected waves off the top of an interface are represented by subscripts indicating the number of the reflecting interface or an m for the Moho (Owens, 1984). Extensive forward modeling was used in this study, along with implementation of an inverse scheme developed by Owens.

In the time domain inversion, the starting model is assumed to be close to the true model, and making a Taylor series expansion about the initial model yields the linearized equations

$$dRi = Ri(obs) - Ri(pk) = \sum_{k=1}^{N} \frac{\partial Ri}{\partial pk} dpk.$$

Here, subscript i denotes the ith sample of the observed and synthetic radial receiver functions, Ri(obs) and Ri(pk), where pk is the kth initial model parameter, and dRi is the residual between the observed and synthetic waveforms. The residual is minimized using the L2 norm, and the pk are

iteratively corrected by dpk until a satisfactory waveform match is achieved.

Synthetics are calculated using Langston's raytracing method, as in the forward problem, and only S-wave velocity is inverted for. The inverse operator is determined using singular value decomposition, and the partial derivatives are determined by a finite difference scheme (Owens, 1984).

It should be noted here that both forward and inverse modeling efforts are exploited in this study. Initially, extensive forward modeling offers insight into relating observed phases with specific structural zones at depth. Basing the intial models mainly on previous seismic refraction and surface wave dispersion results, forward modeling to refine the models, and inverting the receiver functions with smoothed versions of these well constrained starting models (implying that extreme bias is removed from the starting models before inversion) increases confidence in the final derived estimates of S-wave velocity structure.

SURFACE WAVE ANALYSIS

Rayleigh wave dispersion in the Rio Grande rift has been previously analyzed by Sinno and Keller (1986) . They employed the two-station method, using events recorded at both the EPT and ALQ WWSSN seismic stations, determining interstation group and phase velocities from fundamental mode

Rayleigh wave data. The group and phase velocities were simultaneously inverted for gross shear velocity structure along the interstation path.

In this thesis, the data used in the 1986 original study is reprocessed with a scheme which involves filtering seismograms, computing the interstation Green's function, and determining the self-consistent phase and group dispersion with standard errors (Dean and Keller, to be published). The first-order difference inversion scheme (Russell, 1980) is used to derive shear velocity models for the interstation path.

DATA SELECTION

The two station method requires that in order to determine interstation shear structure via Rayleigh wave dispersion analysis, the earthquake sources must occur within a few degrees of the great circle path between the stations (Knopoff et al., 1967). All 5 events used in the 1986 study met this requirement. For the present reanalysis, paper seismogram records from both the EPT and ALQ stations were obtained and the surface wave trains were redigitized. This data set consisted of records for 3 of the original 5 events used.

SURFACE WAVE DATA PROCESSING

The processing scheme devised by Dr. E. A. Dean (see

Appendix) to derive interstation group and phase velocities from multi-event data sets was implemented. As outlined by Dean and Keller (to be published), this scheme involves the following steps for a single event:

(1) Resampling the raw digitized surface wave signal, interpolating at 1 sample/sec.

(2) Windowing the relevant portion of the seismograms is performed to reduce the number of samples processed. By default, this is the portion with apparent velocities between 1.8 km/sec and 4.6 km/sec.

(3) Optional application of a zero-phase quasi-pink filter (QPF) which smooths the spectrum towards constant power per octave.

(4) Application of the multiple filter technique (MFT) to determine initial group velocity estimates. A matrix of power vs. period and group velocity (arrival time) is displayed on the computer screen, and the user may edit the computer selected ridge of the contoured matrix by choosing a different local maximum or deleting a selection.

(5) A least squares polynomial in log T smooths the group velocity function determined by the MFT.

(6) Phase matching iteration (PMI) refines either phase or group velocity. The phase phi(f) is determined by numerical integration of the group arrival time t(f):

$$phi(f) = \int_0^f t(f')df'$$

A "pseudo-autocorrelation function" (PAF) is derived by cross correlating a unit-amplitude signal of phase phi(f) with the seismogram. This PAF is windowed in time and its phase spectrum phi'(f) is used to improve the group arrival times by the inverse of the above equation,

$$t'(f) = dphi'(f)/df.$$

This technique is iteratively applied until the PAF is symmetric.

(7) A time variable filter (TVF) based on the refined group velocity is applied. This step attenuates higher modes and multipath arrivals.

(8) The filtered signals x(t) (near station) and y(t) (far station) are then used to determine an interstation Green's function. The frequency domain convolutional representation of the far station signal can be expressed as

$$Y(f) = G(f) \cdot X(f),$$

where G(f) is the spectrum of the interstation Green's function. G(f) can be recovered by the spectral ratio method as follows:

$$G(f) = C(f) \; / \; A(f),$$

where C(f) is the transformed cross correlation of x(t) and y(t), and A(f) is the transformed autocorrelation of x(t). Spectral holes in the near station signal's spectrum can cause instability in the deconvolution. The deconvolution performed as

$$\langle G'(f) \rangle = \langle C(f) / [\,|X(f)||Y(f)|\,]^{\frac{1}{2}} \rangle$$

decreases this effect, where < > on the right side of the equation means windowing the PAF of g'(t), and |X(f)| and |Y(f)| are the amplitudes of the filtered seismogram spectra. Inverse transformation of G'(f) yields the interstation Green's function, g'(t), which is then filtered as outlined in the steps 1-7. Further analysis to determine the interstation group and phase velocities is as follows:

(9) MFT is applied to the filtered Green's function to

determine the initial estimate of group velocity (u(T)).

(10) A least squares polynomial of variable order smooths the MFT estimated group velocity. The F-test (Dean, 1986) is used to determine the highest order significant fit. Standard errors ($\triangle u$) for the smoothed velocities are determined from the covariance matrix of the polynomial fit to the group velocity data.

(11) PMI is applied to both fast ($u(T) + \triangle u$) and slow ($u(t) - \triangle u$) group velocities and the two refined phase velocities are meaned to obtain "raw phase velocity".

(12) A simultaneous least-squares fit to the raw group and phase velocities is applied as described by Dean (1986). A modified version of the dispersion relation

$$u = v/[1+(T/v)(dv/dT)]$$

is used which handles the non-linear least squares analysis and log-T dependence in this approach. Working with group and phase slownesses ($y(x) = 1/u$, $z = 1/v$) and a scaled expression for period ($x = A + B(\log T)$, with A and B such that $x = -1$ for the minimum period of analysis, and $x = 1$ for the maximum period of analysis) yields

$$y(x) = z(x) - B(dz/dx).$$

Phase slowness is approximated by

$$z(x) = \sum ci \cdot Pi(x),$$

where Pi(x) is an ith degree polynomial of x. Group slowness is

$$y(x) = \sum ci \cdot Qi(x),$$

$$\text{where } Qi(x) = Pi(x) - B(dPi(x)/dx).$$

The expansion coefficients are solved by the least squares method using singular value decomposition, and the order of fit is determined by the F-test. Errors ($\triangle u$, $\triangle v$) for the fitted group (u) and phase (v) velocities are determined from the covariance matrix for the singular value decomposition of the design matrix (Dean and Keller, to be published).

MODELING GROUP AND PHASE VELOCITY DISPERSION

The first-order difference inverse technique (Russell, 1980) is used to derive interstation shear velocity models from the phase and group velocities. This method simultaneously minimizes the standard least squares error and the magnitude of the difference between adjacent solution

elements (Twomey, 1977). Expressed mathematically,

$$(1-A)\sum_{k=1}^{N} e_k^2 + A\sum_{K=2}^{M}(X_{k-1} - X_K)^2$$

is minimized, where ek is the error between observed and predicted values,; xk is the kth element of the solution (model) vector, x; A is an arbitrary scale between 0 and 1; N is the number of observations; M is the number of model parameters. In the above equation, the second term acts to smooth the optimum solution (Sinno and Keller, 1986).

CHAPTER 4: SEISMIC STUDIES AND RESULTS

ANMO RECEIVER FUNCTION STUDY

In this section, both the processing and velocity modeling results for the receiver function analysis are presented. Important features in both waveforms and velocity models will be noted. Geologic interpretations will be addressed in the following section.

Table 2 lists the teleseismic events used as sources in this study. These were all recorded at ANMO between 1983-1984. Based on their spatial distribution, local structure is modeled along three constrained back azimuths: Honshu, Chile, and Tonga events provided control along the northwest, southeast, and southwest back azimuths, respectively.

Only the radial component receiver functions are modeled in this study. Although tangential motion can provide information on lateral structural variation (e.g., dipping interfaces), the merged tangential receiver functions demonstrate no characteristic polarity trends with azimuthal variation. Therefore, horizontal layer parameterizations are made, and only observed radial displacement is modeled.

Figure 14 shows the northwest back azimuth stacking suite receiver functions. The waterlevel (c) values used in the deconvolution process are listed for each trace. The resultant mean stacked receiver function is given at the bottom of Figure 14. Figure 15 is the mean trace again, with

TABLE 2: ANMO Teleseismic Events

Date	Distance <degrees>	Back Azimuth <degrees>	Depth <km>	Mb
	Northwest Back Azimuth			
01/01/84	89.6	311.8	368.	6.5
03/06/84	91.2	307.5	457.	6.2
09/18/84	86.5	309.5	48.	6.6
05/26/83	83.7	315.7	24.	6.8
06/09/83	83.9	315.5	31.	6.3
08/25/83	92.9	314.8	126.	6.1
	Southwest Back Azimuth			
06/01/83	82.7	243.5	180.	6.2
09/17/83	84.6	245.6	33.	6.1
08/30/83	80.7	242.2	39.	6.0
10/17/83	84.5	240.1	30.	6.0
12/03/83	80.6	243.6	82.	6.1
06/15/84	82.1	244.6	247.	6.1
	Southeast Back Azimuth			
10/04/83	69.9	146.0	15.	6.4
10/09/83	69.6	145.8	16.	5.9
10/20/84	69.7	141.9	213.	5.9

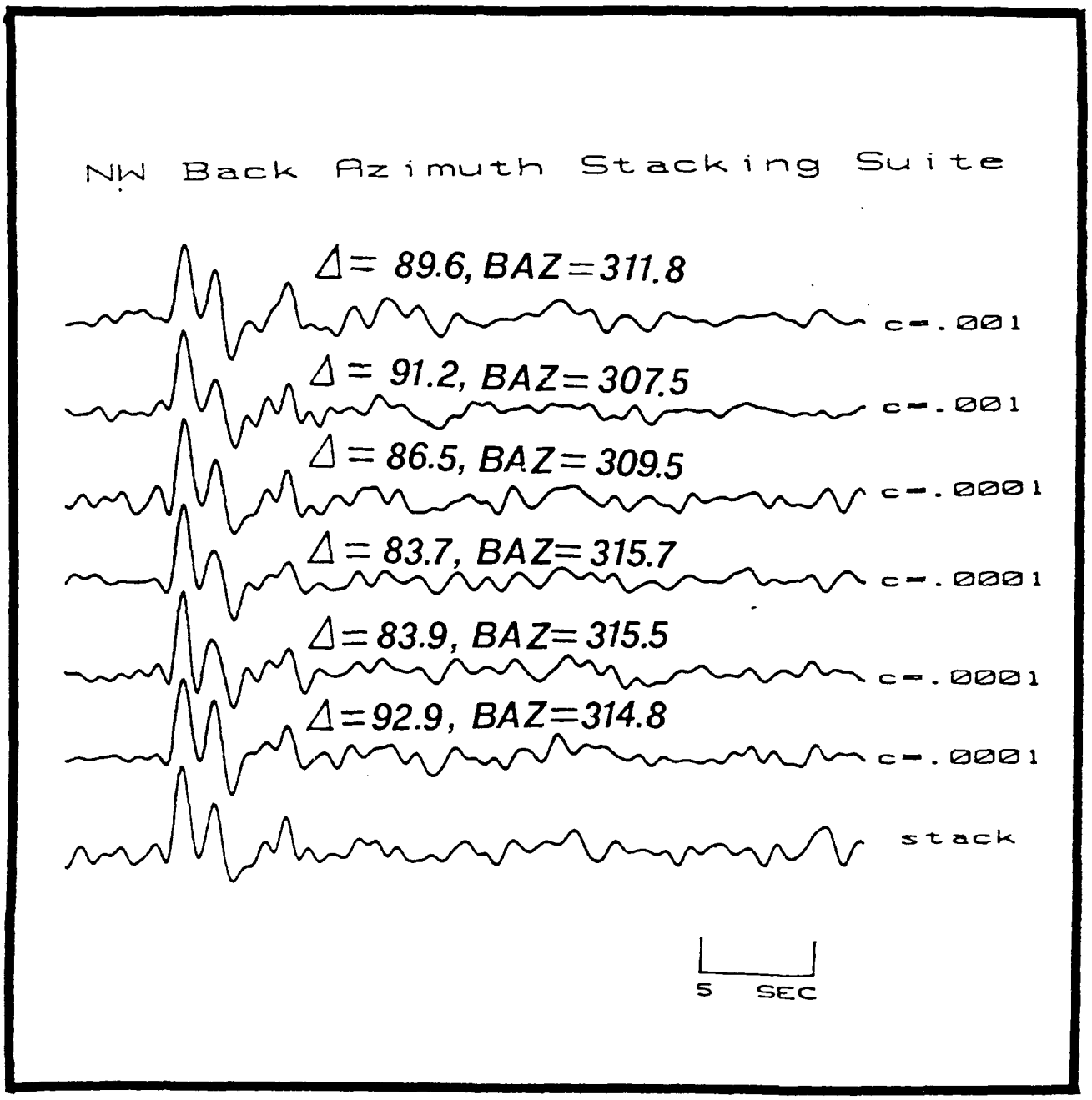

Figure 14. Receiver functions comprising northwest back azimuth data set. △ = source distance; BAZ = back azimuth; c = waterlevel value used; stack = mean stacked trace.

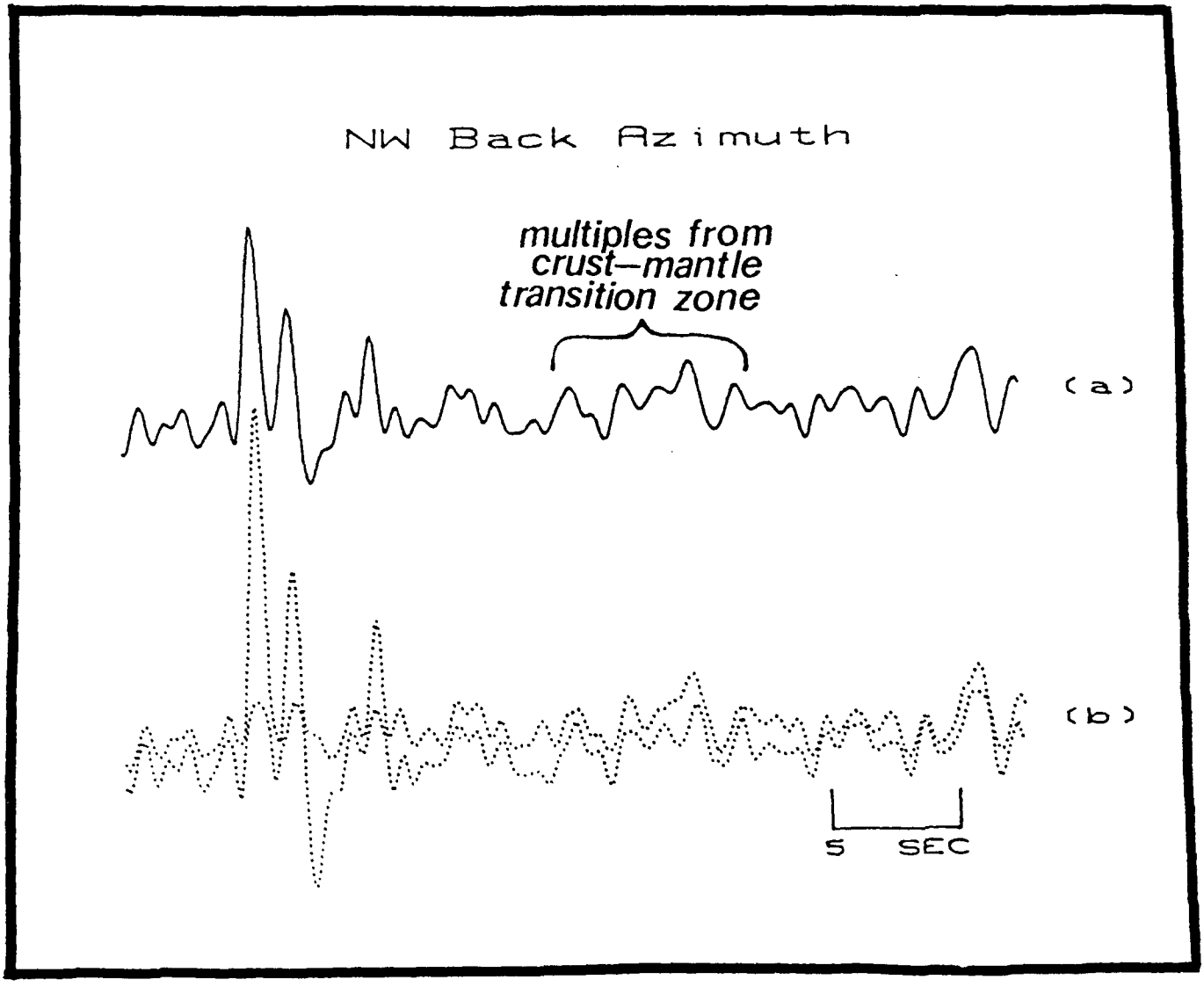

Figure 15. (a) Mean stacked receiver function for northwest back azimuth, and (b) +/- 1 standard deviation data bounds.

its data bounds. The data bounds are determined from the variance in the seismograms within the stacking suite, and are plotted as plus-or-minus 1 standard deviation about the mean. This provides a statistical check of the waveform matching in that a satisfactory match between the synthetic and observed radial receiver functions is achieved if the synthetic fits within these bounds. Since traces are normalized to the amplitude of the direct P arrival before stacking, a zero variance results about this first arrival in the stacked receiver function. The nonzero variance at the P arrival in the northwest mean trace is due to the fact that more relative weight was applied during stacking to the cleaner traces within this stacking suite. In other words, once normalized, the cleaner traces were given a greater relative scaling in amplitude than the noiser seismograms, and the statistics calculated during stacking reflect this. In retrospect, for statistical purposes, it would have been more appropriate to weight these additively rather than multiplicatively. However, it will be demonstrated that the followed procedure did not distort these results.

Figures 16 and 17 show the southeast back azimuth stacking suites and the mean stacked trace with data bounds, respectively. The similar data for the southwest back azimuth are given in Figures 18 and 19. Phases seen between 2-5 seconds (following the direct P arrival at 0 seconds) in these mean receiver functions (Figures 17 and 19) exhibit a

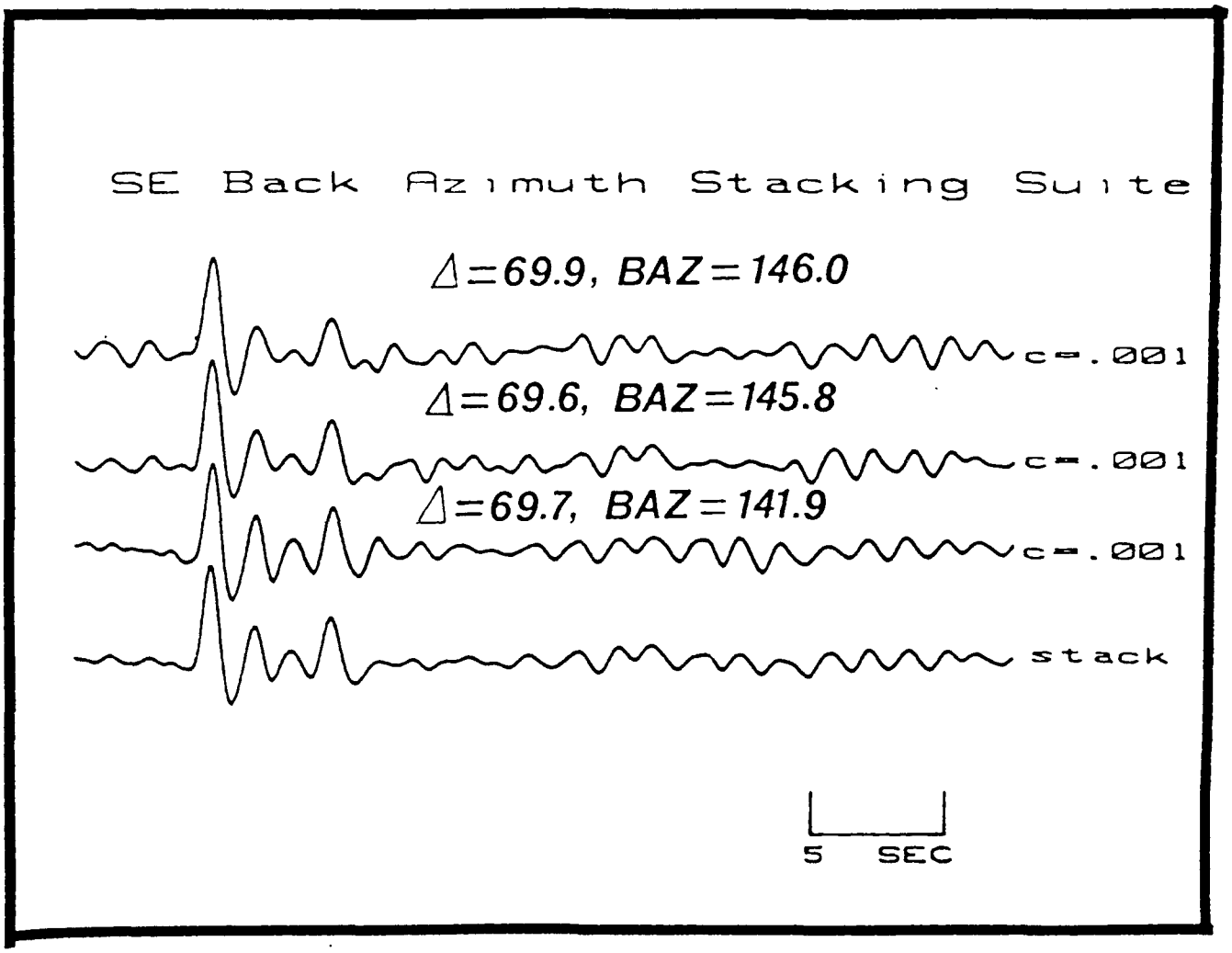

Figure 16. Receiver functions comprising southeast back azimuth data set. $\triangle$ = source distance; BAZ = back azimuth; c = waterlevel value used; stack = mean stacked trace.

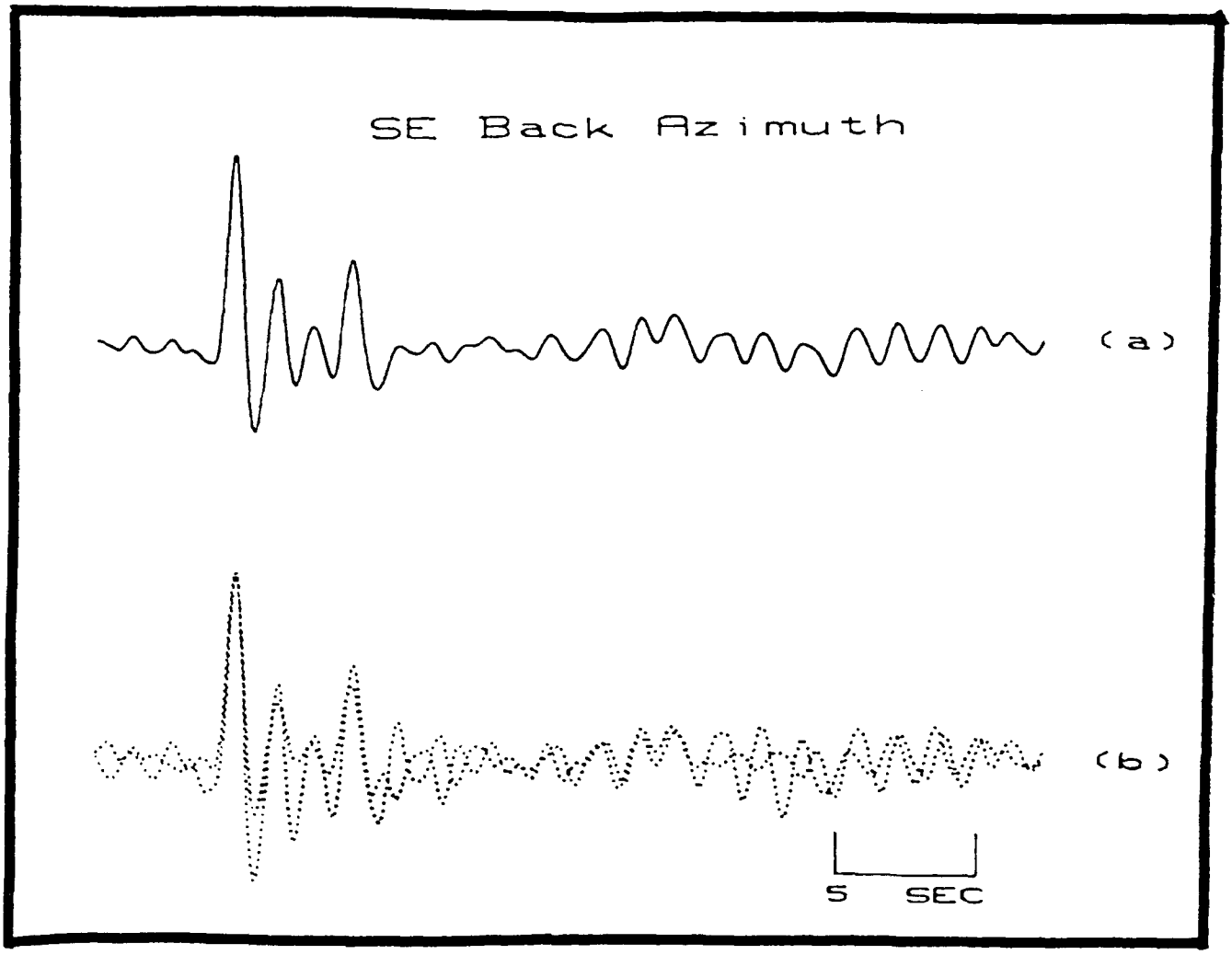

Figure 17. (a) Mean stacked receiver function for southeast back azimuth, and (b) +/- 1 standard deviation data bounds.

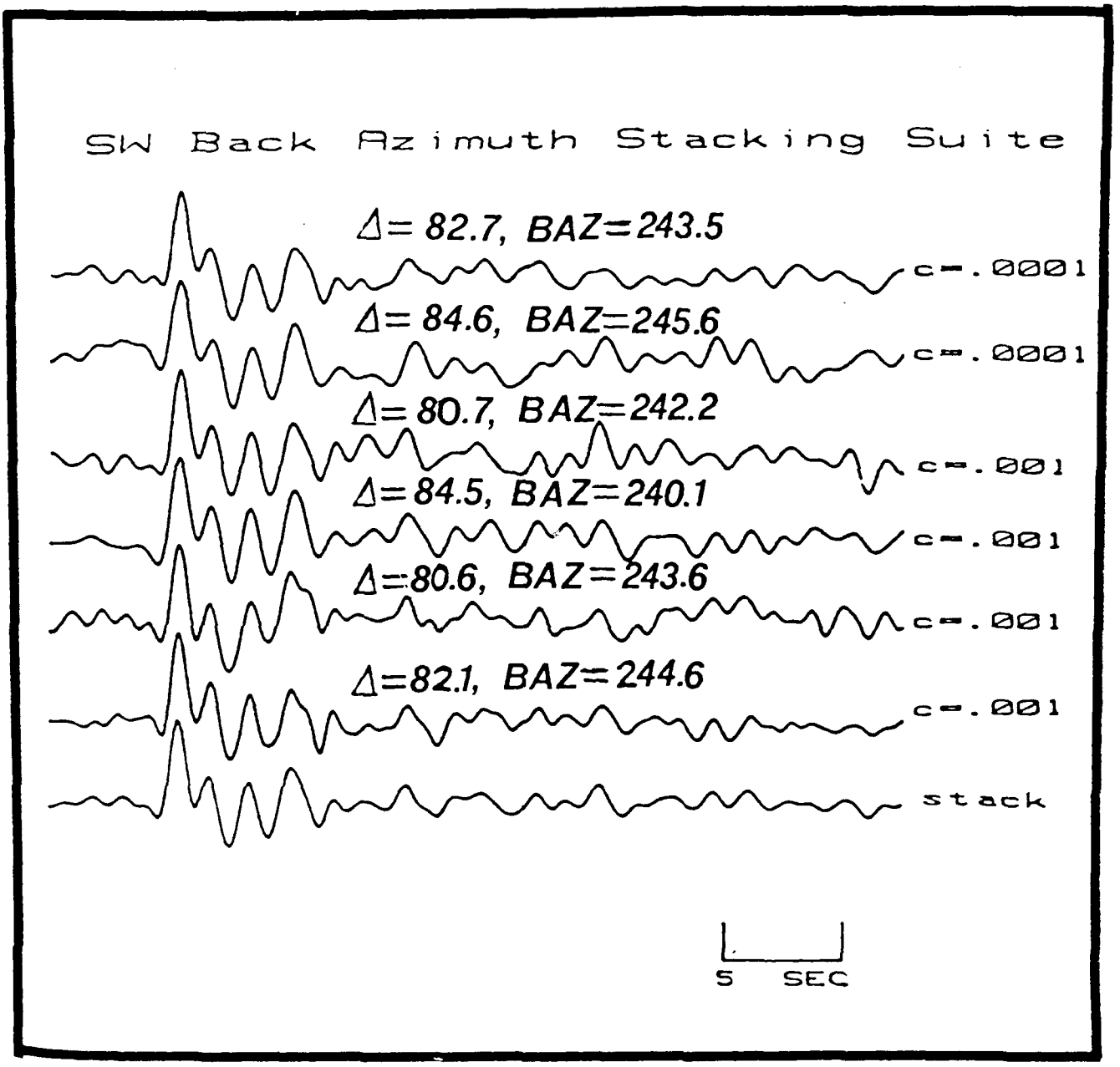

Figure 18. Receiver functions comprising southwest back azimuth data set. Δ = source distance; BAZ = back azimuth; c = waterlevel value used; stack = mean stacked trace.

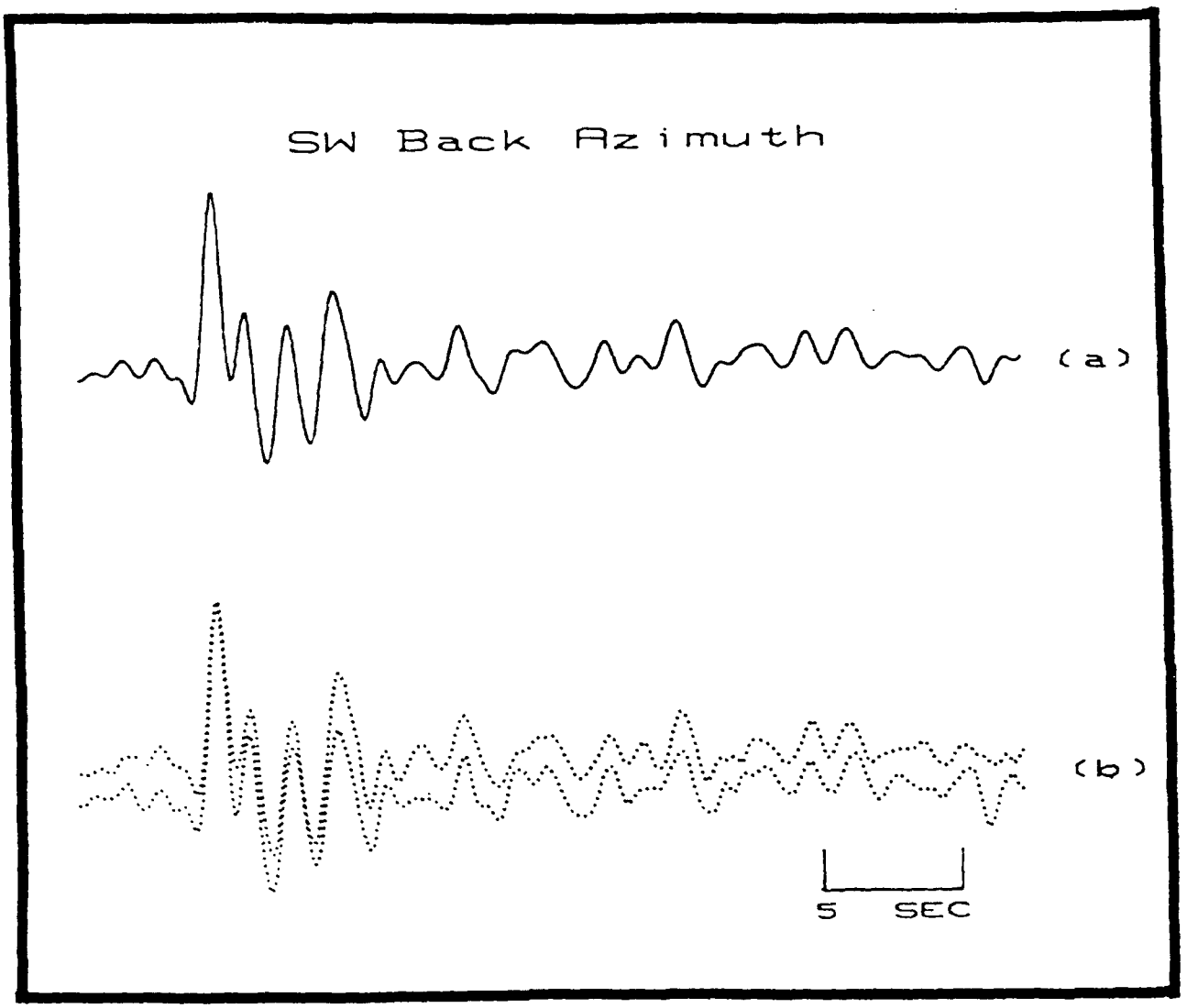

Figure 19. (a) Mean stacked receiver function for southwest back azimuth, and (b) +/- 1 standard deviation data bounds.

similar character. They are significantly different from the northwest back azimuth receiver function (Figure 15) within the same time window. In each mean trace, converted phases arriving between 13-20 seconds are multiples from the crust-mantle transition zone. Phases following these arrivals are conversions from deeper structure within the upper mantle.

The final radial waveform fit for the northwest back azimuth is given in Figure 20. All phases between 0-27 seconds are satisfactorily matched, as indicated by both Figure 20-a and Figure 20-b. The corresponding derived S-wave velocity model is shown in Figure 21 and Table 3. The upper crustal portion of the derived model indicates a positive shear velocity gradient down to 15 km depth. A slight positive velocity step near 28 km depth tends to produce the Ps phase arriving at 3.2 seconds in this receiver function, which is not seen in the other two receiver functions. This might suggest a more defined mid-to-lower crust division toward the northern rift portion, but more data would be needed to verify this. Just beneath this feature at about 30 km, a 2 to 4 km thick zone appears which shows a slight flattening in S-wave velocity. Upper mantle velocities are encountered near 37 km depth, and, given the +/- 2 standard errors in the velocity estimates, the model indicates the transition from lower crust to upper mantle occurs over an interval of approximately 3 to 6 km. A positive shear wave velocity gradient of about .01 km/sec/km

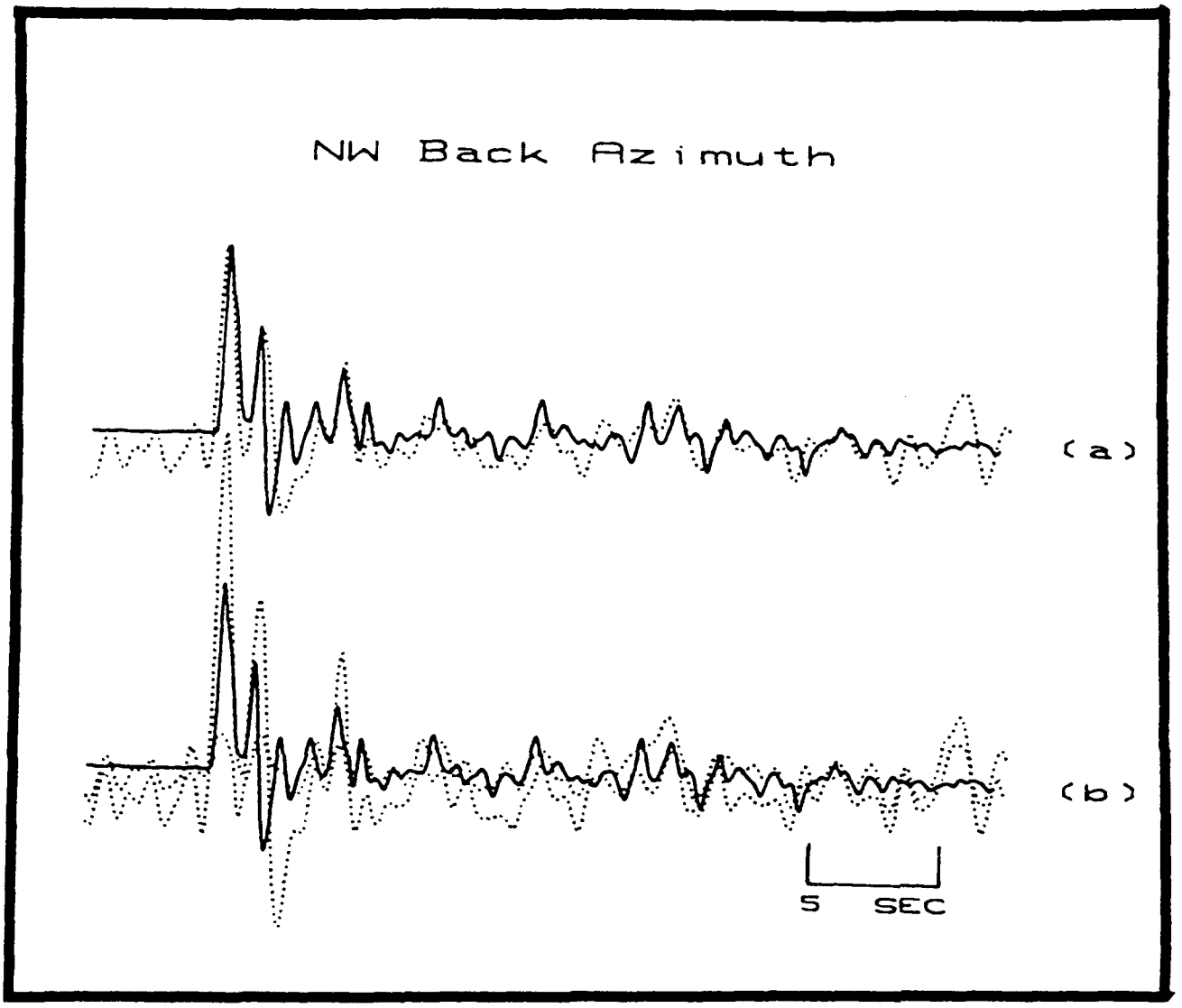

Figure 20. Final waveform fit for northwest back azimuth. (a) Dotted trace = mean receiver function, solid trace = derived synthetic. (b) Dotted traces = upper and lower data bounds, solid trace = derived synthetic.

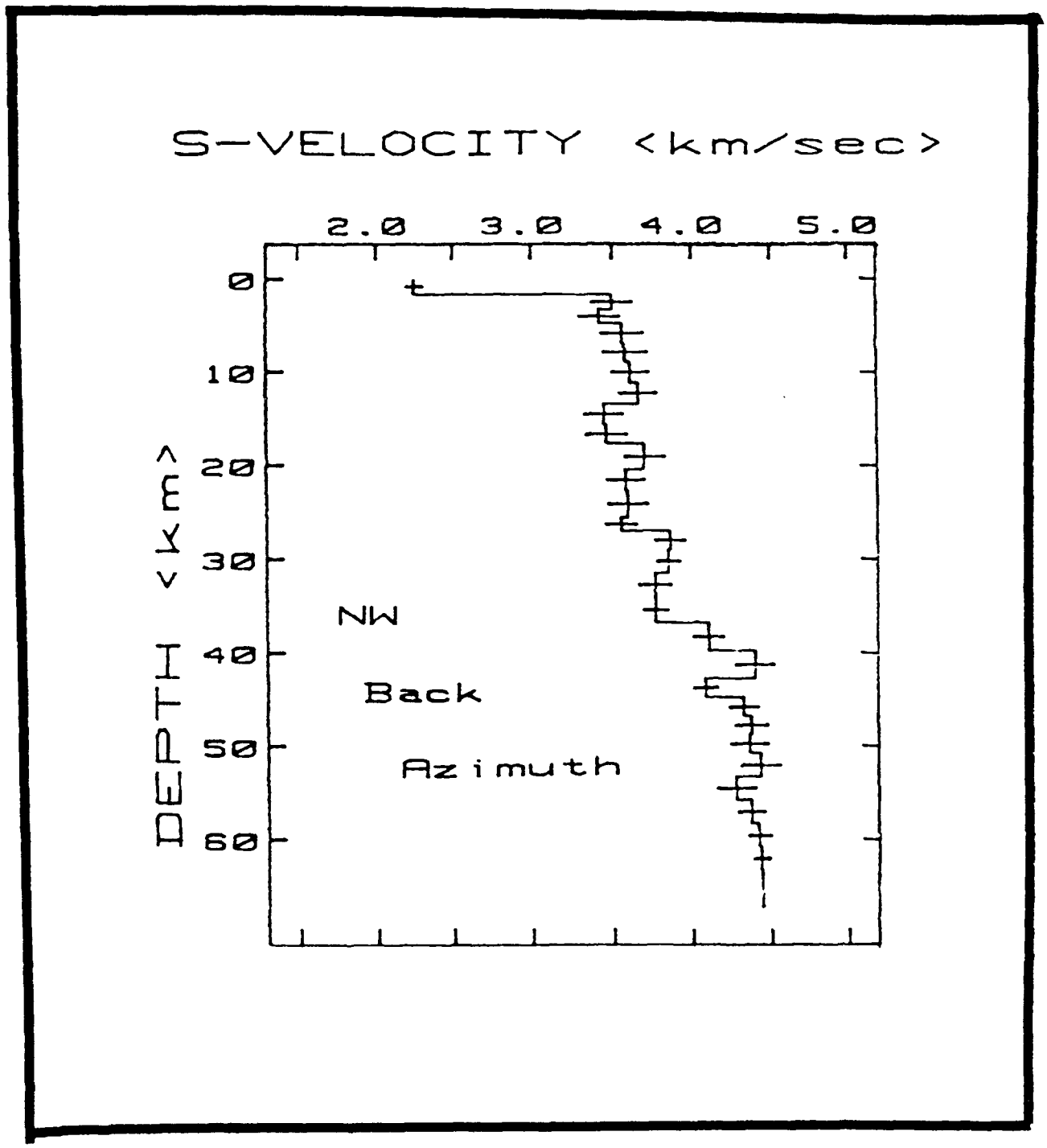

Figure 21. Final S-wave velocity model for northwest back azimuth. Error bars represent +/- 2 standard errors.

TABLE 3: Final S-wave Velocity Model-- ANMO NW Back Azimuth

Layer #	Thickness <km>	NW S-wave Velocity <km/sec>
1	1.75	2.25
2	1.60	3.50
3	1.50	3.42
4	2.10	3.57
5	2.00	3.58
6	2.25	3.61
7	2.25	3.67
8	2.25	3.45
9	2.00	3.46
10	2.75	3.70
11	2.25	3.59
12	2.90	3.60
13	1.40	3.56
14	2.00	3.87
15	2.50	3.85
16	2.50	3.77
17	2.80	3.77
18	3.00	4.11
19	3.00	4.40
20	2.00	4.08
21	2.00	4.32
22	2.00	4.37
23	2.00	4.36
24	2.50	4.43
25	2.50	4.27
26	2.50	4.37
27	2.50	4.42
28	2.50	4.43
29	0.00	4.44

beneath the crust mantle transition continues to over 60 km depth in this model.

Figures 22, 23, and Table 4 give the final waveform modeling results and final velocity model, respectively, for the southeast back azimuth. This model has a smooth positive velocity gradient to a depth near 28 km. As in the northwest model, shear velocities seem to be attenuated close to 30 km depth, but when the standard errors in the southeast velocity model at this depth are considered, verification of this particular feature is difficult. A gradational Moho shear boundary near 36 km depth determined in the inversion yields a significantly good waveform fit for this back azimuth. Here again, shear velocities within the upper mantle increase with depth.

Lastly, Figure 24 is the derived synthetic fit for the southwest back azimuth. Figure 25 and Table 5 give the derived S-wave velocity model. Upper crustal velocities increase to a depth of 15 km. Interpretation of the slight velocity reversal between 15 and 20 km may not be justifiable due to the overlap in error bars. Again, flattening to reversing of shear velocity is noted at 30 to 32 km depth. A transitional shear boundary grading into upper mantle near 36 km depth produces a statistically acceptible match for the crust mantle multiples. As in the other models, the crust mantle transition occurs over an interval of 3 to 6 km. Although this model shows a strong positive velocity step

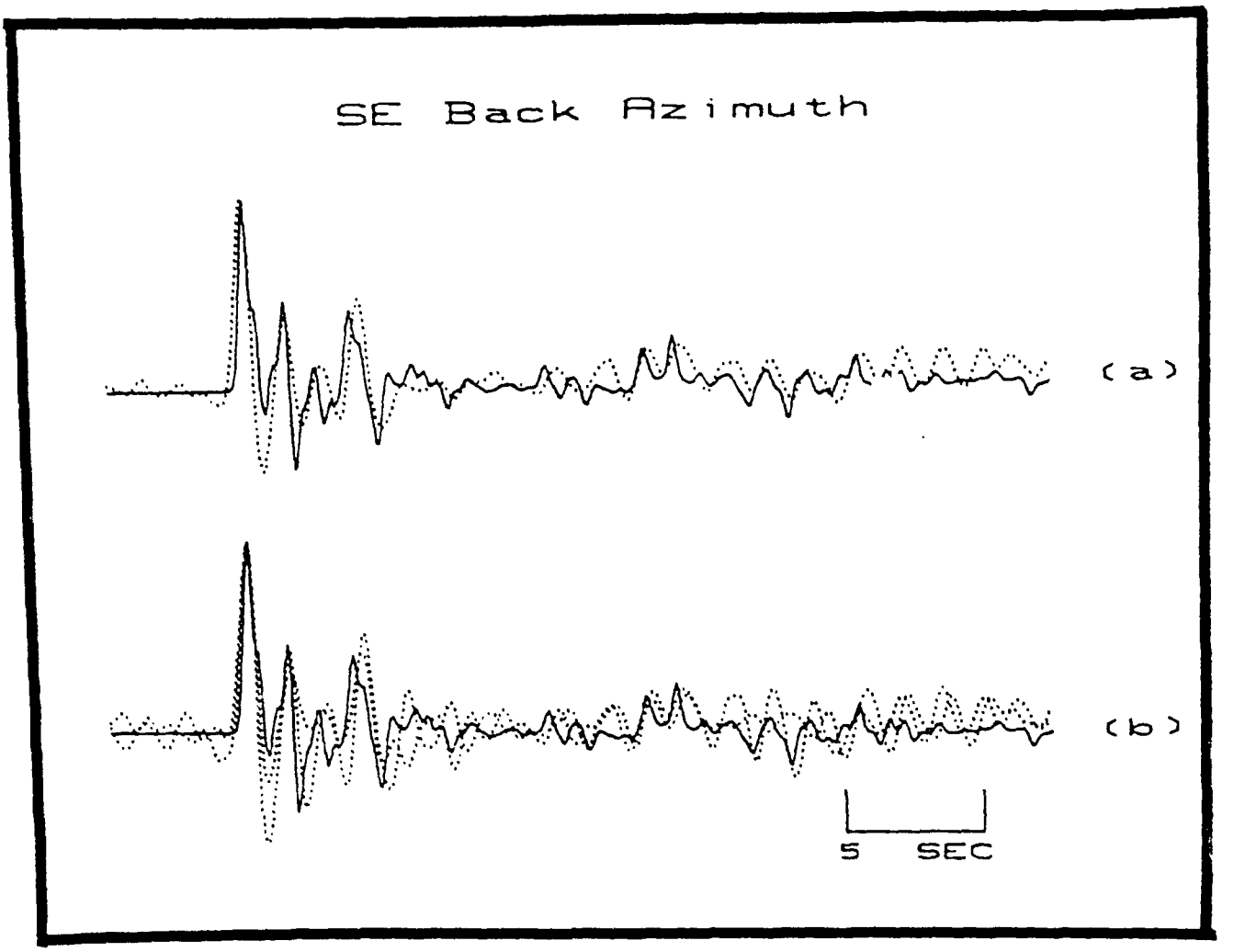

Figure 22. Final waveform fit for southeast back azimuth. (a) Dotted trace = mean receiver function, solid trace = derived synthetic. (b) Dotted traces = upper and lower data bounds, solid trace = derived synthetic.

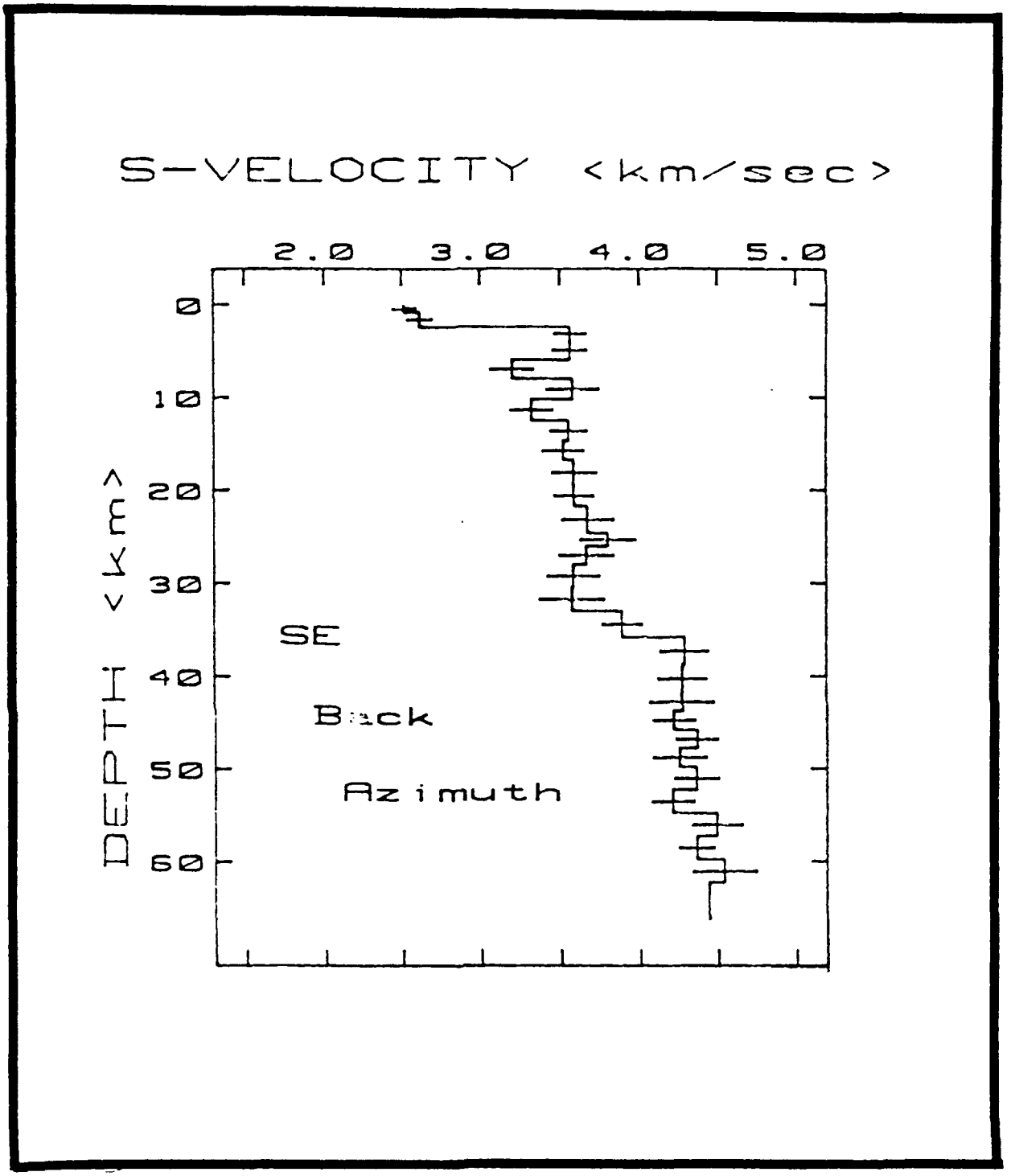

Figure 23. Final S-wave velocity model for southeast back azimuth. Error bars represent +/- 2 standard errors.

TABLE 4: Final S-wave Velocity Model-- ANMO SE Back Azimuth

Layer #	Thickness <km>	SE S-wave Velocity <km/sec>
1	0.80	2.51
2	1.60	2.61
3	1.50	3.56
4	2.10	3.56
5	2.00	3.20
6	2.25	3.58
7	2.25	3.32
8	2.25	3.55
9	2.00	3.52
10	2.75	3.59
11	2.25	3.59
12	2.90	3.67
13	1.40	3.80
14	2.00	3.66
15	2.50	3.58
16	2.50	3.57
17	2.80	3.89
18	3.00	4.29
19	3.00	4.28
20	2.00	4.27
21	2.00	4.22
22	2.00	4.36
23	2.00	4.25
24	2.50	4.36
25	2.50	4.21
26	2.50	4.49
27	2.50	4.36
28	2.50	4.54
29	0.00	4.44

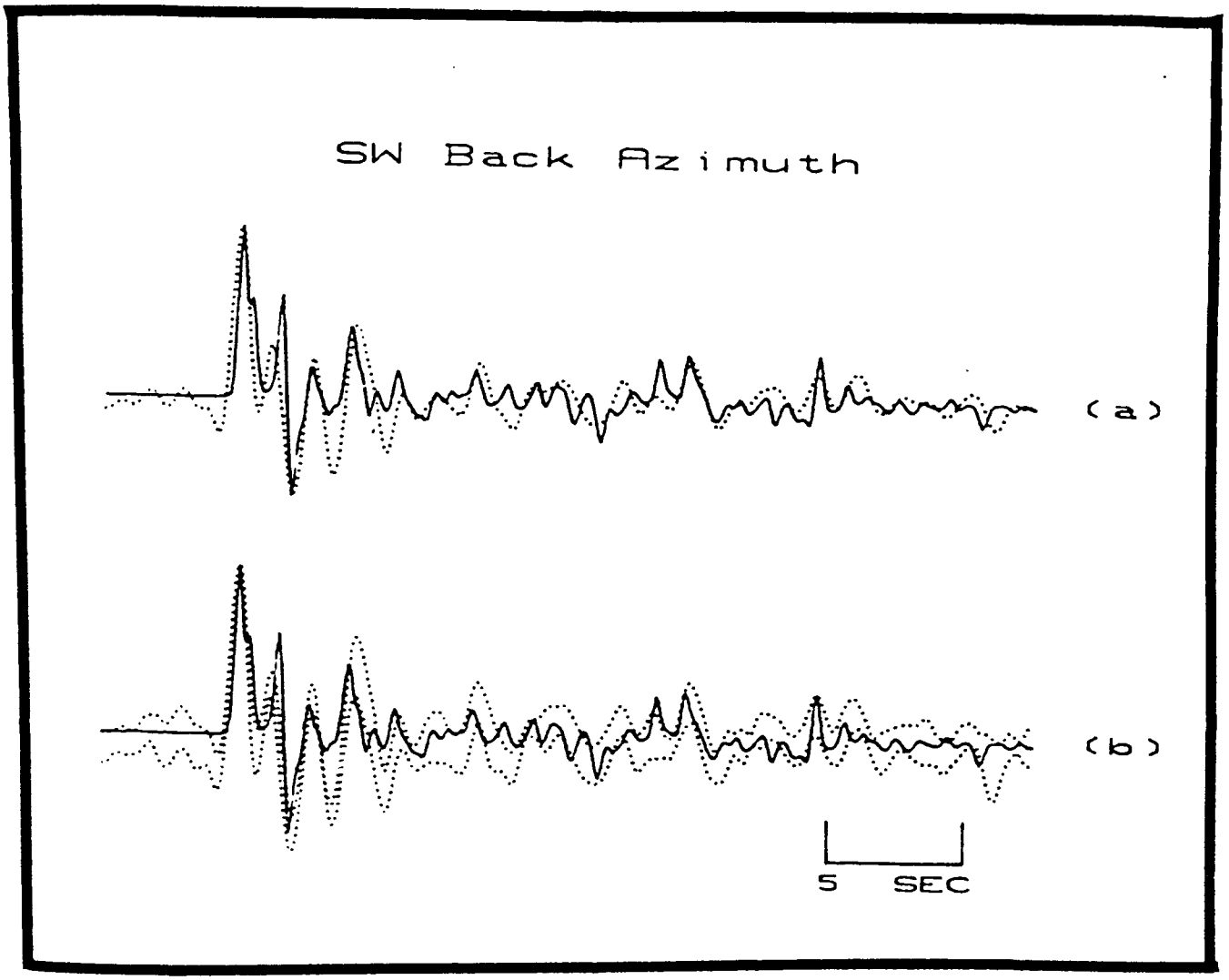

Figure 24. Final waveform fit for southwest back azimuth. (a) Dotted trace = mean receiver function, solid trace = derived synthetic. (b) Dotted traces = upper and lower data bounds, solid trace = derived synthetic.

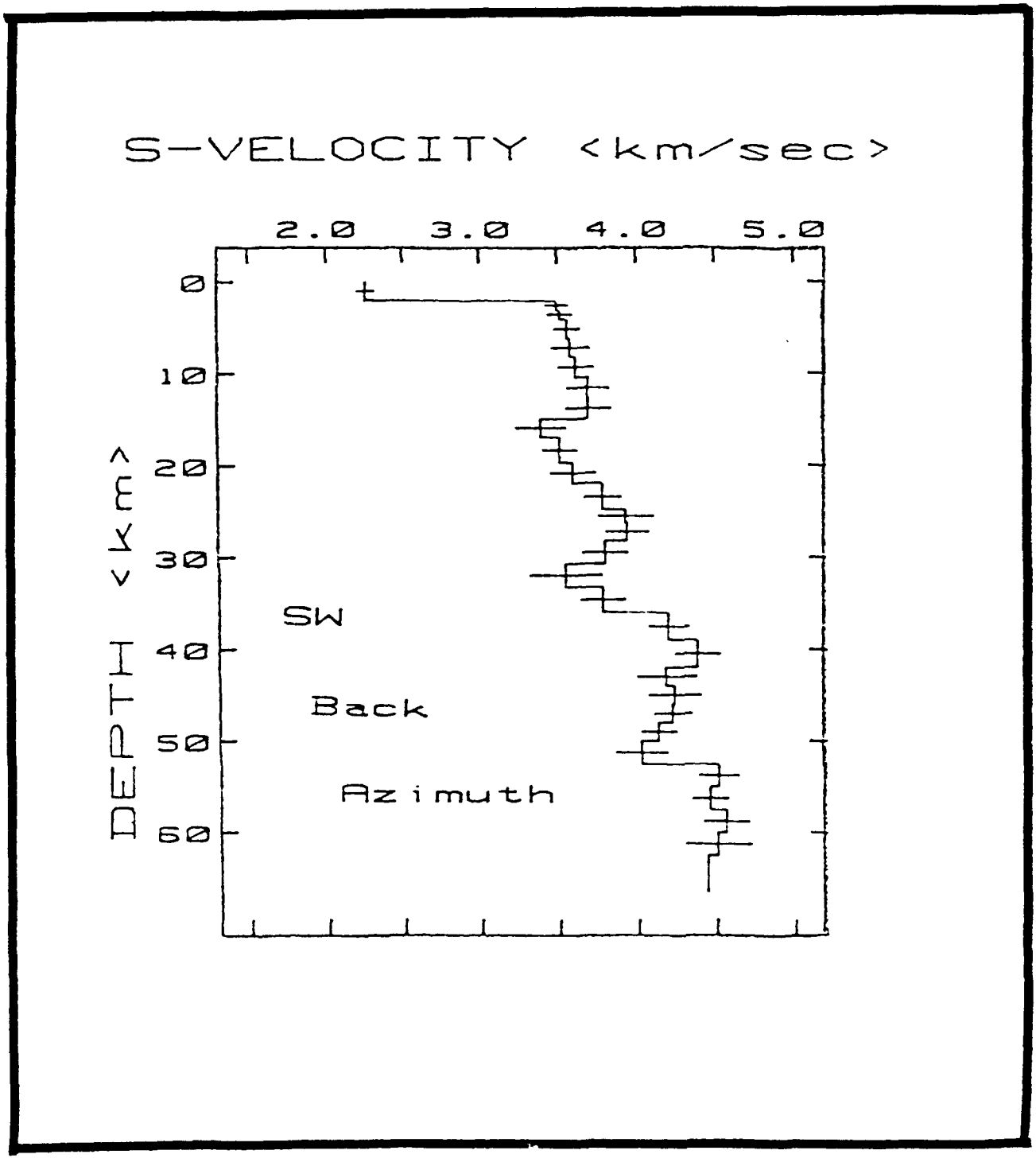

Figure 25. Final S-wave velocity model for southwest back azimuth. Error bars represent +/- 2 standard errors.

TABLE 5: Final S-wave Velocity Model-- ANMO SW Back Azimuth

Layer #	Thickness <km>	SW S-wave Velocity <km/sec>
1	2.10	2.26
2	1.00	3.50
3	1.00	3.52
4	2.10	3.57
5	2.00	3.58
6	2.25	3.61
7	2.25	3.69
8	2.25	3.70
9	2.00	3.39
10	2.75	3.51
11	2.25	3.60
12	2.90	3.79
13	1.40	3.93
14	2.00	3.94
15	2.50	3.80
16	2.50	3.54
17	2.80	3.78
18	3.00	4.20
19	3.00	4.38
20	2.00	4.18
21	2.00	4.24
22	2.00	4.22
23	2.00	4.13
24	2.50	4.02
25	2.50	4.51
26	2.50	4.46
27	2.50	4.56
28	2.50	4.51
29	0.00	4.44

near 52 km depth which produces the high amplitude phases between 22 to 25 seconds in the synthetic receiver function, the associated errors make interpreting the abruptness of this boundary difficult.

GEOLOGIC INTERPRETATION OF MODELING RESULTS

The shear wave velocity models together with observed regional compressional velocities, Rio Grande rift geotherms (Decker and Smithson, 1975) and igneous and metamorphic phase diagrams (Figures 26 and 27) comprised the basis for these lithological determinations. Absolute lithology determination is supported by information gathered by N. I. Christensen (1982) on characteristic rock velocities and by A. W. Hatheway and G. A. Kiersch (1982) on engineering properties of rocks. Upper mantle structural interpretations are made here in light of the observed volcanism in the central rift region, together with various references on experimentally derived upper mantle models using xenolith studies.

UPPER CRUST (< 15 KM DEPTH):

Beneath the near surface sedimentary layer, the upper crustal basement beneath ANMO is known to be comprised of Precambrian granitic rocks (Vp = 5.9 - 6.1 km/sec). Shear velocities for all three back azimuths range from 3.4 km/sec near the surface to 3.5 - 3.7 km/sec near 15 km depth

(Poisson ratios ranging between .21 to .24). The gradational character of the shear velocities may indicate a transition from more felsic to intermediate composition granitic rocks.

MIDDLE CRUST (15 - 25 KM DEPTH):

Throughout this zone, shear velocities in the models are indicative of intermediate composition igneous rocks (e.g., granodiorite). To the southeast, velocities grade smoothly throughout this zone. Higher heat flow along the central rift along with 5 to 6 kbars pressure at 15 to 20 km depth would tend to produce a slight reduction in the shear velocity of approximately 2.7 gm/cc density granodiorite, which we observe in both the southwest and northwest back azimuthal models. The aforementioned velocity reversal in the southwest back azimuth near the top of this zone could also be reasonably explained by local thermal effects. Figure 28 shows the outline of the Socorro magma body as mapped by Rhinehart et al. (1979). The propagation path for energy arriving from the Tonga teleseisms intersects this horizon (15 - 20 km depth) within nearly 20 km distance from the northernmost extent of this body. However, the standard errors in velocity mask the degree to which these thermal effects may attenuate shear velocities in this vicinity. The southwest model demonstrates a relatively steeper velocity gradient into lower crustal depths as compared to the northwest and southeast models.

LOWER CRUST AND CRUST-MANTLE TRANSITION (25 - 40 KM DEPTH):

In each model, an increase in shear velocity is noted within the upper portion of this zone. This may reflect a change from intermediate igneous lithologies (e.g., granodiorite) to intermediate-to-mafic granulite lithologies. These anhydrous granulites can form in continental rift zones under the influence of high mantle-derived heat flow (Weber, 1986). Figure 27 shows that for the Rio Grande rift thermal and pressure regimes, granulites may form near 20 km depth. According to Frost and Frost (1987), in extensional regimes, upwelling basaltic magmas at the base of the crust introduce additional heat as well as high volumes of CO2 which act to dehydrate neighboring rocks, thereby driving granulite metamorphism of crustal materials. Along the rift axis, shear velocities derived here of approximately 3.75-3.80 km/sec and compressional velocities near 6.5 km/sec (Sinno et al., 1986; Olsen, 1979) are consistent with 2.8-2.9 gm/cc density mafic granulites. In addition, seismic reflection imaging of the lower crust (e.g., Brown et al., 1979, 1980) has revealed layered, discontinuous reflectors within this zone which could indicate the expected layering of these granulites with mafic rocks and preexisting lower velocity lithologies. However, the layer thickness parameterizations of 2-3 km used in this present study fail to reveal laminations in the 1-D models locally within these zones. Based on these shear velocities, these complex zones are

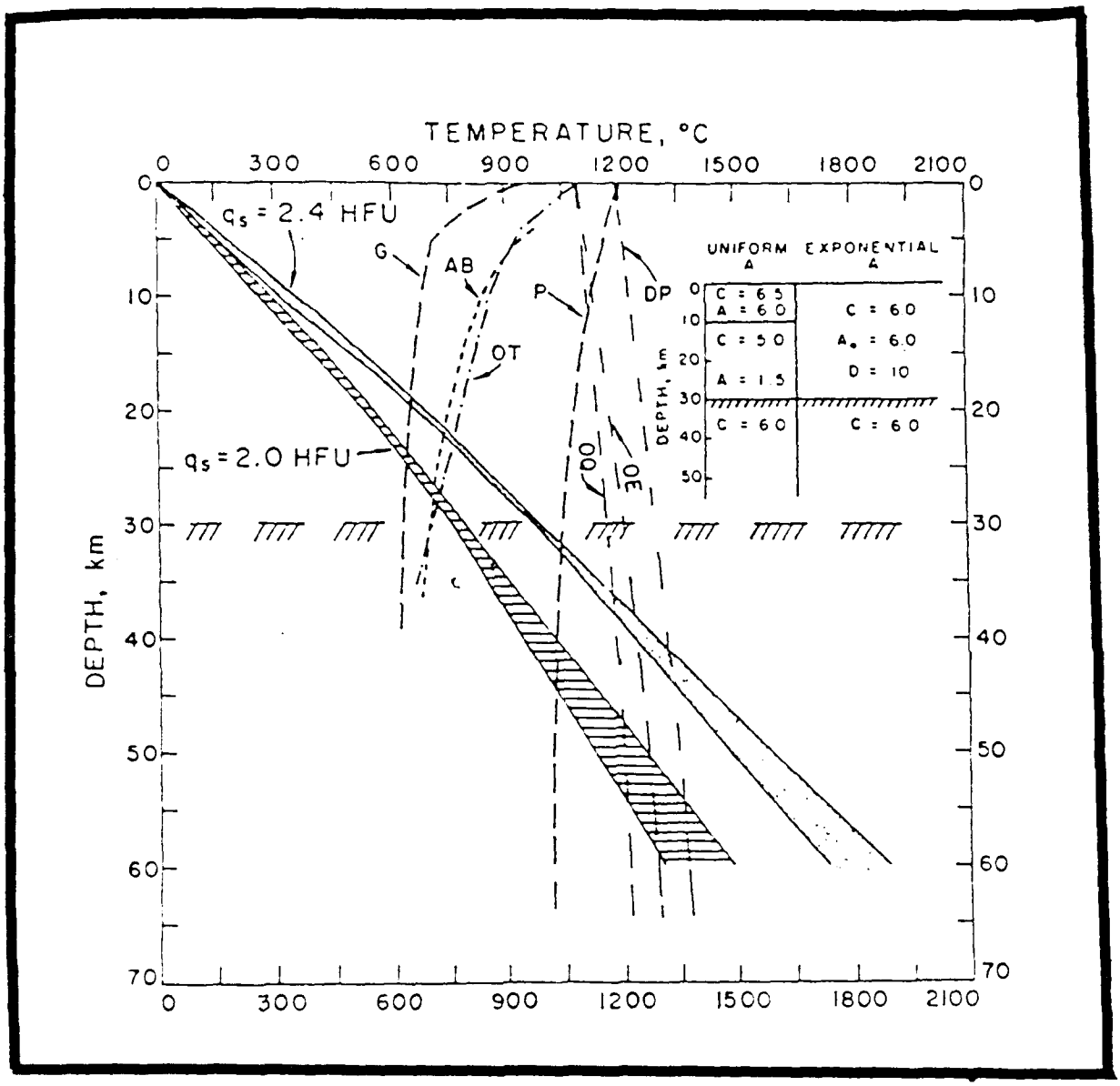

Figure 26. Southern Rio Grande rift geotherms: qs = surface flux assumed in temperature calculations. Wet solidus curves: G = granodiorite, P = peridotite, AB = alkaline basalt, OT = olivine tholeiite. Dry solidus curves: OQ = olivine tholeiite to quartz eclogite at high pressures, OE = olivine tholeiite to olivine eclogite at high pressures, and DP = peridotite (from Decker and Smithson, 1975).

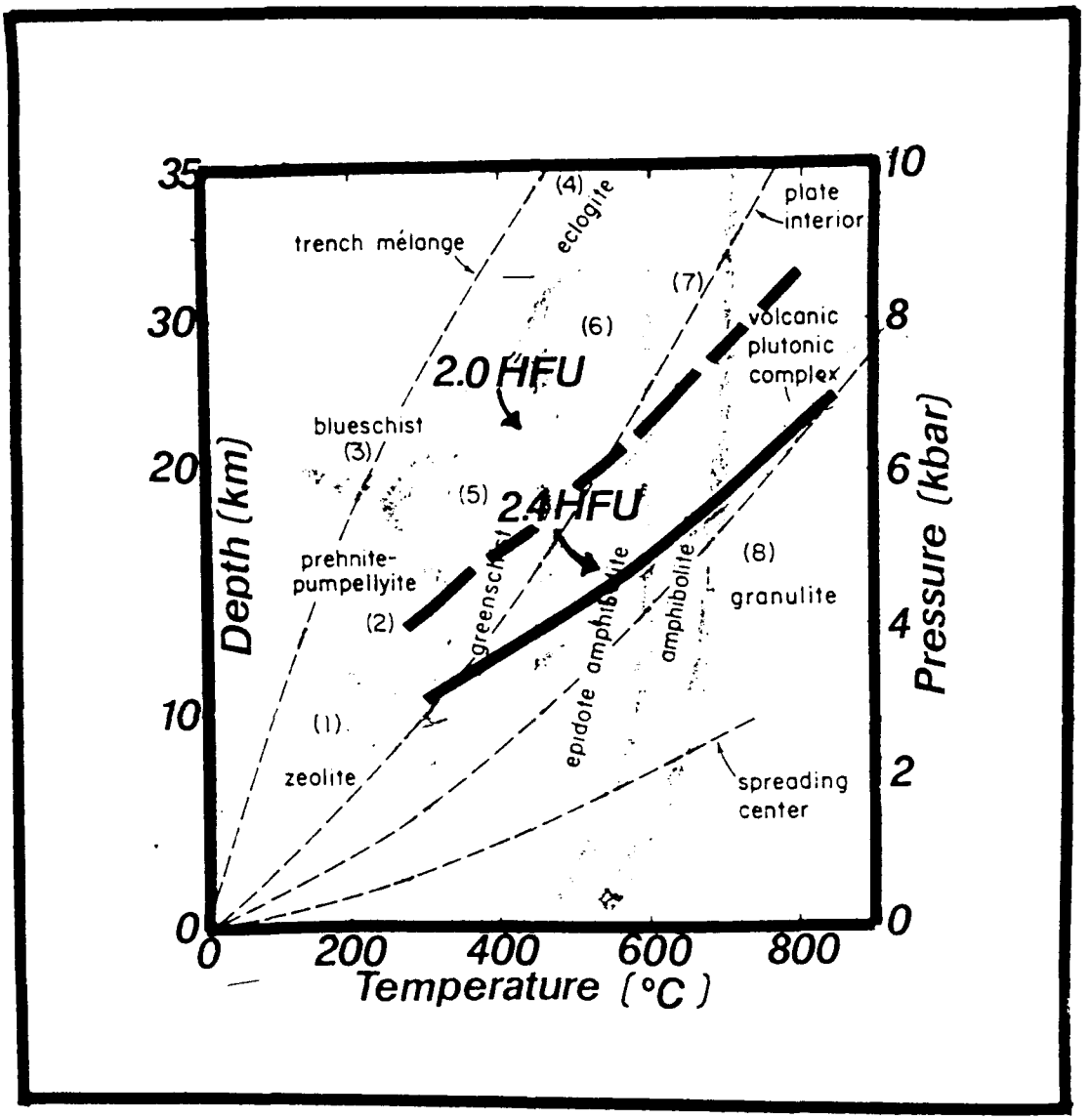

Figure 27. Metamorphic phase diagram with Rio Grande rift geotherms (from Decker and Smithson, 1975) demonstrating potential for lower crustal granulite facies (modified from Ernst, 1976).

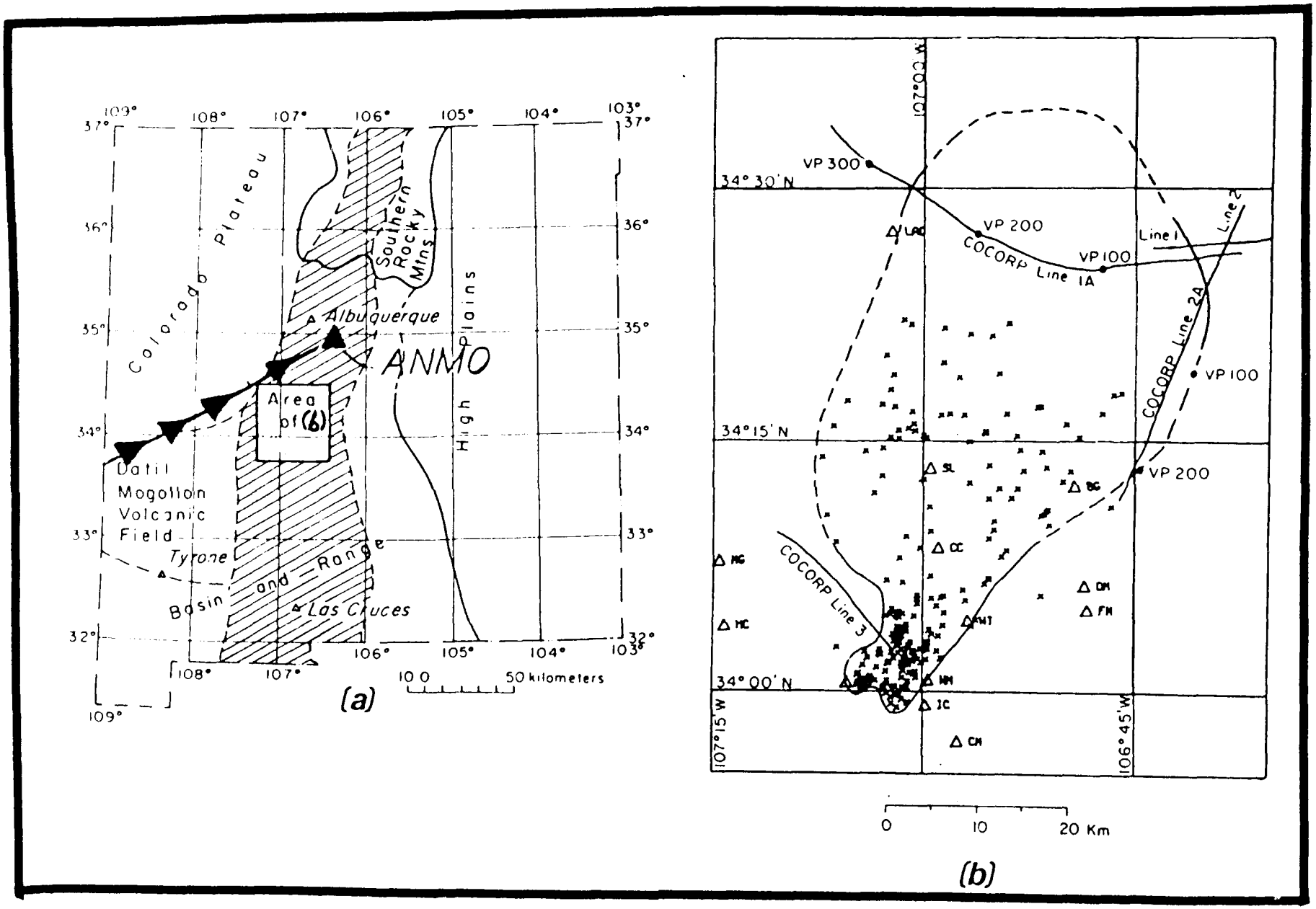

Figure 28. Proximity of (a) propagation path of seismic energy arriving from Tonga events (SW BAZ) to (b) mapped extent of Socorro magma body (modified from Rhinehart et al., 1979).

likely intermediate-to-mafic granulites, together with underplated mafics and other precursor crustal rocks. The refraction work of Olsen, et al (1979) and Sinno et al. (1986) found the crust mantle boundary between 31 and 34 km depth along the southern to central rift axis. This zone corresponded to Pn derived velocities between 7.6 -7.94 km/sec, with 7.77 km/sec taken as the average Moho velocity. However, this same zone corresponds to a slight attenuation in the shear velocities. Assuming that depth related errors are minimal between these analyses, the high Poisson ratios (near .33) evidenced by shear wave attenuation within this zone could be attributed to the presence of basaltic material at the base of the crust from partial melting within the upper mantle. Plio-Pleistocene volcanism within the central rift area in the form of olivine tholeiitic basalts indicate that these originated from partial melting within the upper mantle (Baldridge, 1979). This mechanism could emplace melt rich in silica, olivine, and pyroxene at the base of the crust, which may produce the observed shear velocity anomaly. However, it may be more reasonable to assume that the depth to the upper mantle in the vicinity of the refraction profiles would differ from the depths to the upper mantle noted for the 1-D azimuthal models. Then this zone between 30 and 34 km in the models with attenuated velocities near 3.6 to 3.7 km/sec would not correspond to the refraction Moho (i.e., would lie above it), and could be explained as an

interval characterized by partial melting of the lower crust beneath the granulite suite, possibly overlying upwelled basalts released from partial melting near 50 km depth in the upper mantle.

Between 35 and 40 km depth, the shear velocities increase rapidly into typical upper mantle values (4.25-4.35 km/sec). This likely reflects a transition from the overlying lower crustal partial melt zone to the high silica-content (near 50%) olivine and pyroxene upper mantle partial melt (which should correspond to the refraction Moho, with Pn velocity = 7.7 km/sec) to spinel peridotite near 40 km depth.

UPPER MANTLE (BELOW 36-40 KM DEPTH):

The velocities within the upper mantle observed in the models range between 4.25 to 4.45 km/sec. Given the higher rift geotherm relative to adjacent provinces, these are appropriate velocities for upper mantle between about 40 and 60 km depth, where a peridotite composition with some partial melt present should prevail. Poisson ratios based on these determination and compressional velocities calculated by Sinno (1984) have an average range between .28 and .31. The pressure gradient within this zone (approximately .27 kbar/km) may alone account for the slight positive shear velocity gradient. Although the velocity step near 52 km depth observed in the southwest model does produce a satisfactory waveform match for phases between 22 and 25

seconds in the southwest receiver function, one cannot be confident that these are not intralayer multiple phases from the crust-mantle transition which cannot be generated using the fast raytracing method of Langston. If such an anomaly does exist, however, partial melt between 45 and 50 km could explain this shear wave attenuation. This depth could also mark the zone where replacement of spinel by garnet in upper mantle peridotite occurs, although it is uncertain if the associated density change would be sufficient to produce this velocity anomaly. Another possible explanation could be that this zone marks the lithosphere-asthenosphere transition zone.

EPT-ALQ SURFACE WAVE DISPERSION STUDY

Table 6 lists the events used as sources in determination of interstation dispersion. These earthquakes were located in the eastern Pacific between 1980 and 1982. The same EPT and ALQ analog recorded long period vertical component seismograms from the 1986 study were obtained and peaks, troughs, and inflection points of the surface wave trains were redigitized. The distance from the event to the station, relative start time (0 seconds) and end time for digitization, and time in seconds from the event time to the start of the record were recorded for velocity determination. The raw digitized seismograms were interpolated to 1 sample/sec with a piecewise, cubic, polynomial fit (Wiggins,

TABLE 6: Source Events and EPT-ALQ Station Data

Date	Origin Time	Lat.	Lon.	Azimuth to EPT <degrees>	Dist. to EPT <km>
		<degrees>			
09/29/80	2221:45.3	18.33 N	106.37 W	-0.5	1489.1
05/05/82	1200:41.7	22.09 N	107.24 W	3.7	1075.3
12/20/81	0907:32.3	4.40 S	105.30 W	-1.8	4001.0

Station	Lat.	Lon.	Azimuth to EPT <degrees>	Dist. to EPT <km>
EPT	31.77 N	106.51 W	----	----
ALQ	34.94 N	106.46 W	1.0	351.6

1976) prior to filtering.

Figures 29 through 34 demonstrate filtering of the EPT and ALQ seismograms. In each, part (a) is the windowed seismogram. A quasi-pink filter (QPF) was applied to the Fourier transform of each signal in order to boost long period gain lost due to WWSSN instrument response for low frequencies (Dean and Keller, 1990). Part (b) shows the multiple filter technique (MFT) derived group dispersion (triangles), and phase match iterated (PMI) phase (solid) and group (dashed) curves. For each station analysis, the time variable filtered (TVF) seismograms appear in part (c).

The windowed seismogram in Figures 29 (from EPT) and 30 (from ALQ) are for an event off the coast of Jalisco, Mexico on September 29, 1980. Both signals are fairly clean, with the exception of the long period noise component with apparent velocity between 2.1 and 2.4 km/sec in the ALQ recording. PMI results in essentially no refinement in group velocity (Figures 29(b) and 30(b)). Figures 29(c) and 30(c) are the signals after time variable filtering. Later arriving interference (presumably multipath) was effectively removed in the TVF process.

Figures 31(a) and 32(a) are, respectively, the windowed EPT and ALQ seismograms for the May 5, 1982 event off the coast of central Mexico. A higher mode early arrival (apparent velocity between 3.2 and 3.7 km/sec) is noted in both signals. PMI applications for the EPT signal using an

experimental range of integration constants between 40 to 60 seconds resulted failed to produce any refinement to MFT selected group velocities between 40 and 50 second periods (Figure 31(b)), where clearly a discrepancy in PMI determined phase and group velocity exists. In both TVF seismograms, higher mode and later arriving interference are significantly reduced (Figures 31(c) and 32(c)).

In Figures 33 and 34, filtering results for the EPT and ALQ signals from a December 20, 1989 event in the northern Easter Island cordillera event are shown. PMI results in a slight refinement in MFT selected group velocities. Again, higher mode propagation and later arriving interference has been removed in the TVF process.

Filtering of the interstation Green's functions for the three events is shown in Figures 35, 36, and 37. In each, part (a) is the windowed cross correlation of the EPT and ALQ filtered signals. Interstation dispersion is shown in part(b). The extreme deviation in the PMI group velocity from the MFT group velocity noted in the EPT-ALQ dispersion for the Easter Island event (Figure 37(b)) deserves comment. The MFT selected velocities in this period range were edited out because they looked incorrect. As a result, the PMI application yielded this refinement to the group velocity curve, which is close to the original MFT selection.

Figures 38, 39, and 40 illustrate the interstation dispersion determined from the filtered Green's functions.

MFT group velocities are shown in part (a), with the fast (solid) and slow (dashed) group velocity curves. PMI for the fast and slow group velocities yields fast and slow phase velocities, which are meaned to produce the phase velocities (circles) in part (b). The curves in part (b) are the simultaneous least-squares fit to the mean phase and MFT group data. The self-consistent phase and group velocities with standard errors are given in part (c).

Having determined the EPT-ALQ path dispersion for each individual event (Figure 41(a)), these are weighted by the inverse square of their standard errors, and the mean group (triangles) and phase (circles) interstation dispersion is determined, as shown in Figure 41(b).

In Figure 42(b), comparison of the polynomial fitted group and phase dispersion curves from Sinno and Keller's 1986 study (symbols) with the simultaneous fits derived here (curves) reveals close agreement in phase velocity over the 10 to 65 second period range. Group velocity deviations are noted at the extreme periods of our analysis. The techniques applied here have resulted in a smoother estimated group dispersion curve over the period range of analysis. However, given the short interstation distance (351 km) between EPT and ALQ, no additional dispersion information could be gained for periods outside this range.

Figures 29 - 34. (following pages) Filtering results for individual events: (a) Windowed, resampled seismogram. (b) Dispersion of (a). Triangles = MFT selected group velocities, dashed line = PMI group velocities, and solid curve = PMI phase velocities. (c) TVF seismogram based on PMI group velocity curve in (b).

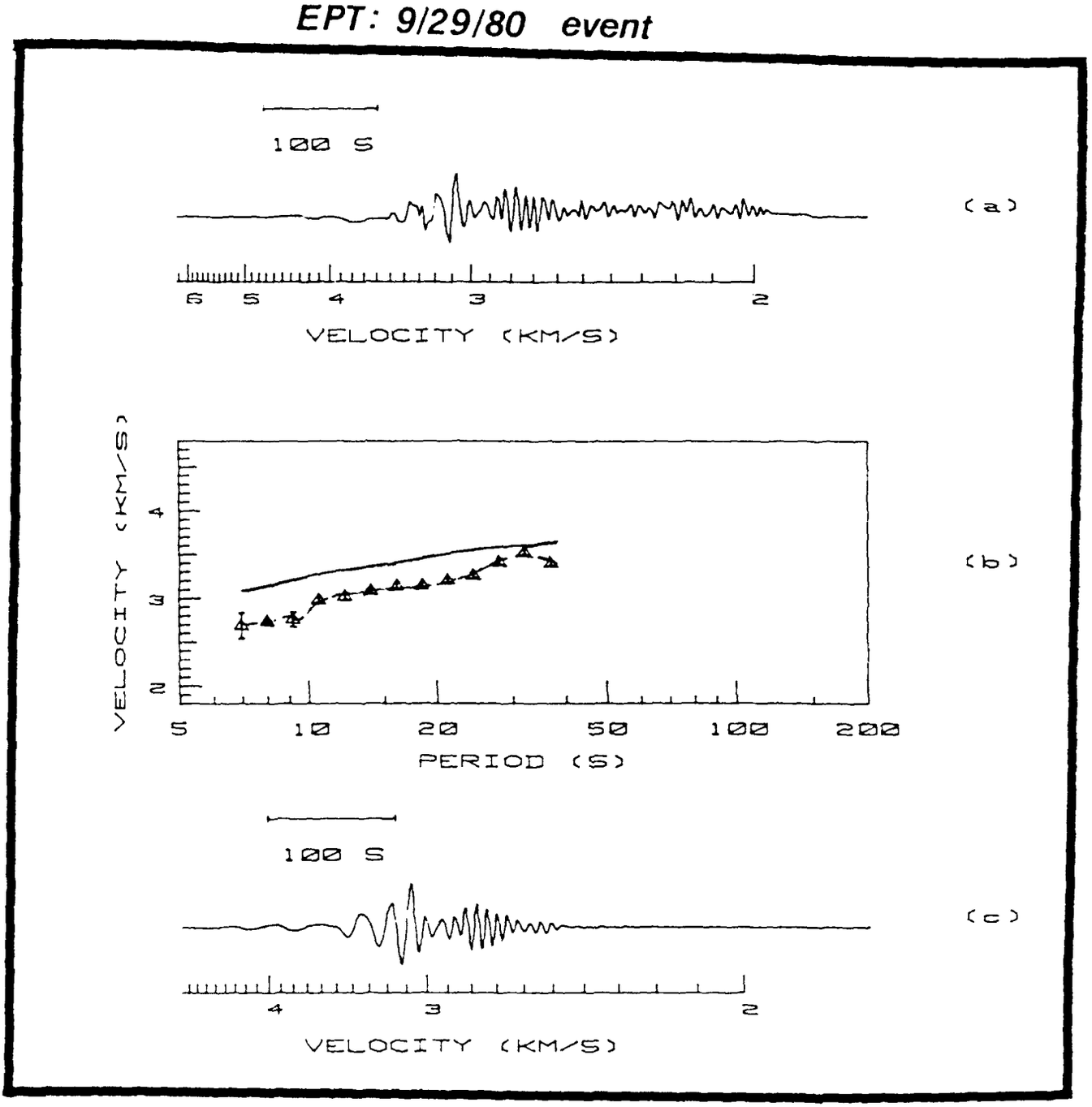
EPT: 9/29/80 event
100 S
(a)
6 5 4 3 2
VELOCITY (KM/S)
VELOCITY (KM/S)
2 3 4
5 10 20 50 100 200
PERIOD (S)
(b)
100 S
(c)
4 3 2
VELOCITY (KM/S)

Figure 29.

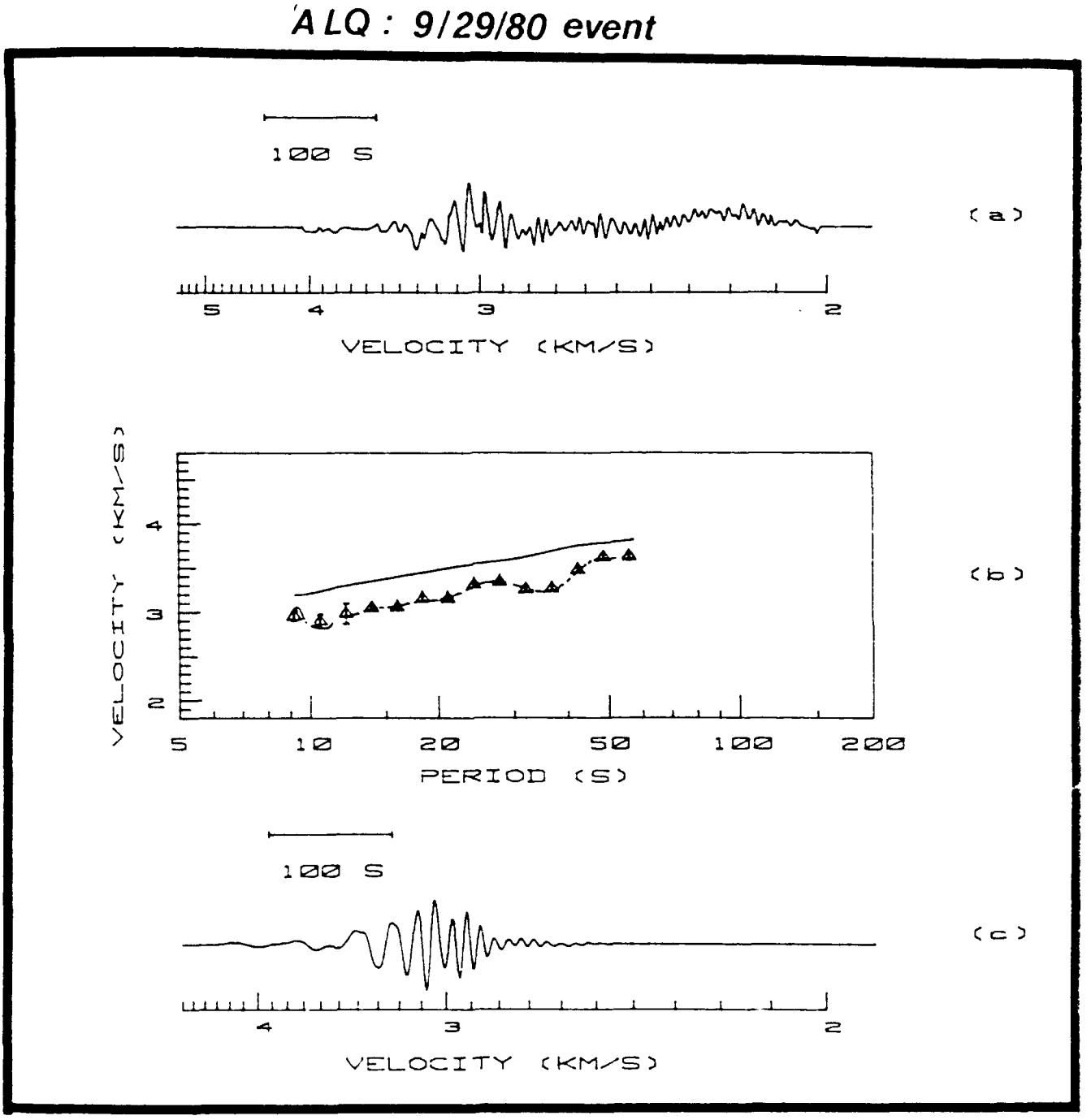
ALQ : 9/29/80 event
100 S
(a)
5
4
3
2
VELOCITY (KM/S)
VELOCITY (KM/S)
4
3
2
(b)
5
10
20
50
100
200
PERIOD (S)
100 S
(c)
4
3
2
VELOCITY (KM/S)

Figure 30.

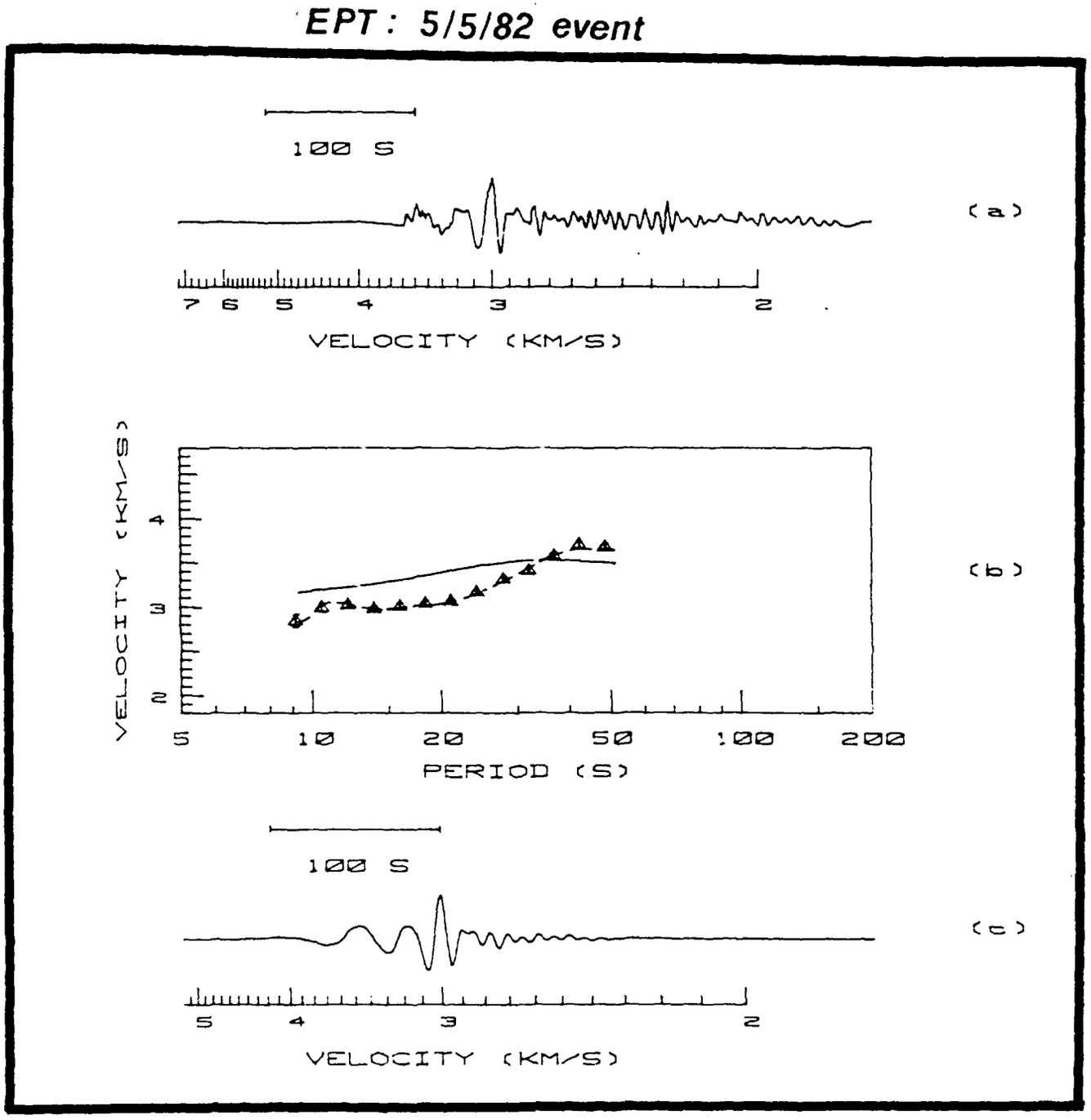
EPT : 5/5/82 event
100 S
(a)
7 6 5 4 3 2
VELOCITY (KM/S)
VELOCITY (KM/S)
4
3
2
5 10 20 50 100 200
PERIOD (S)
(b)
100 S
(c)
5 4 3 2
VELOCITY (KM/S)

Figure 31.

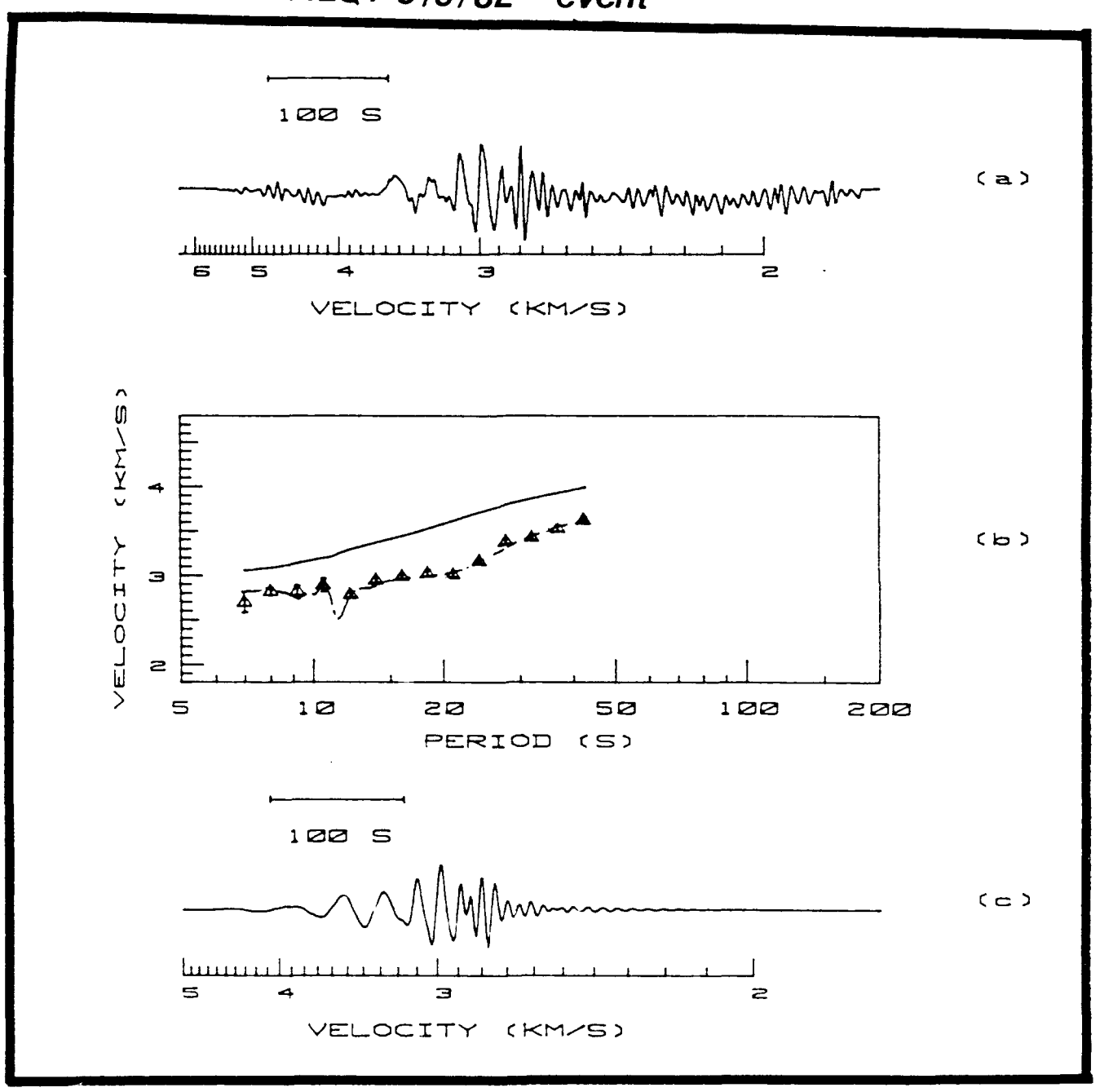
ALQ: 5/5/82 event
100 S
(a)
6 5 4 3 2
VELOCITY (KM/S)
VELOCITY (KM/S)
2 3 4
5 10 20 50 100 200
PERIOD (S)
(b)
100 S
(c)
5 4 3 2
VELOCITY (KM/S)

Figure 32.

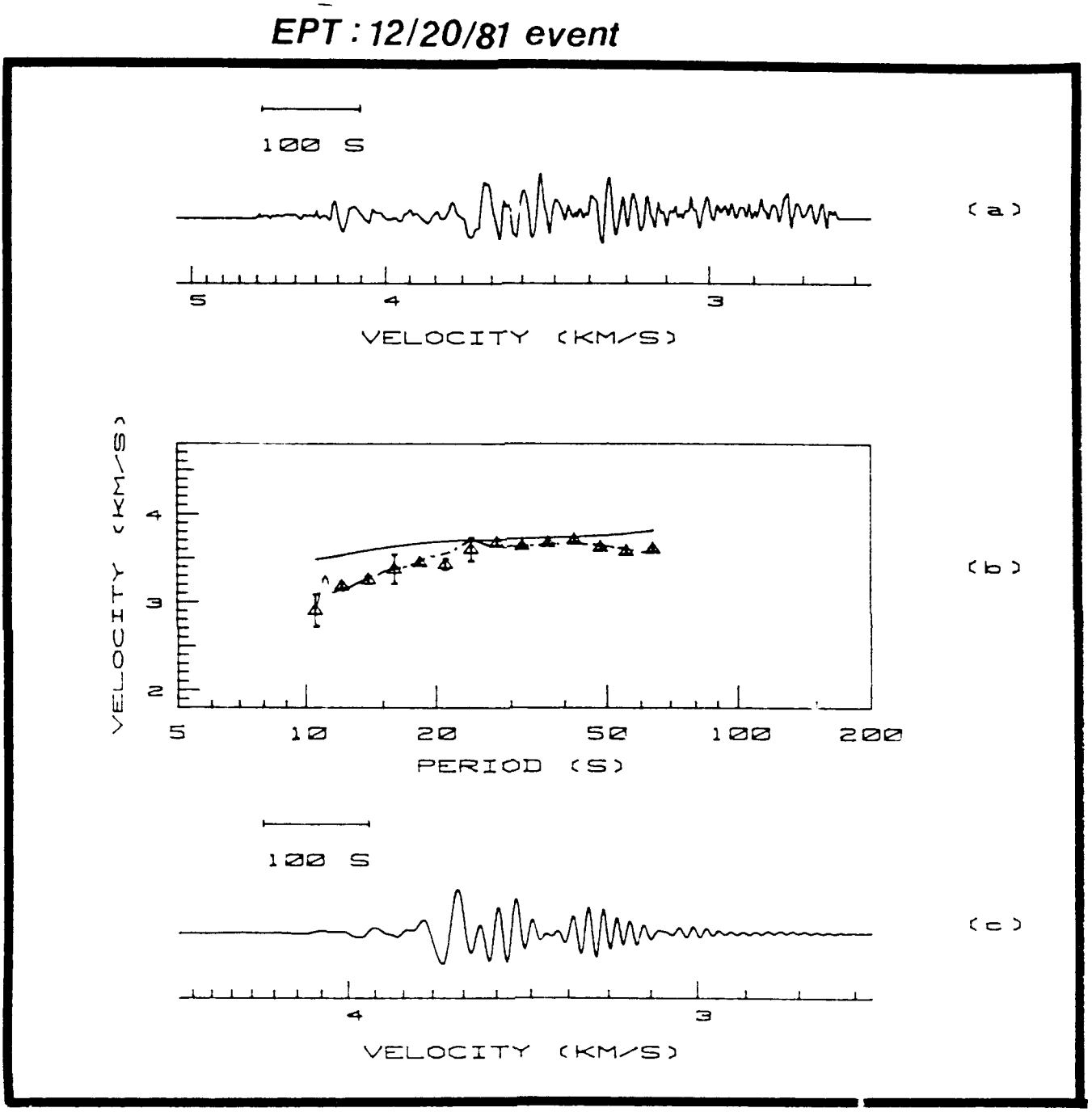
EPT : 12/20/81 event
100 S
(a)
5
4
3
VELOCITY (KM/S)
VELOCITY (KM/S)
4
3
2
(b)
5
10
20
50
100
200
PERIOD (S)
100 S
(c)
4
3
VELOCITY (KM/S)

Figure 33.

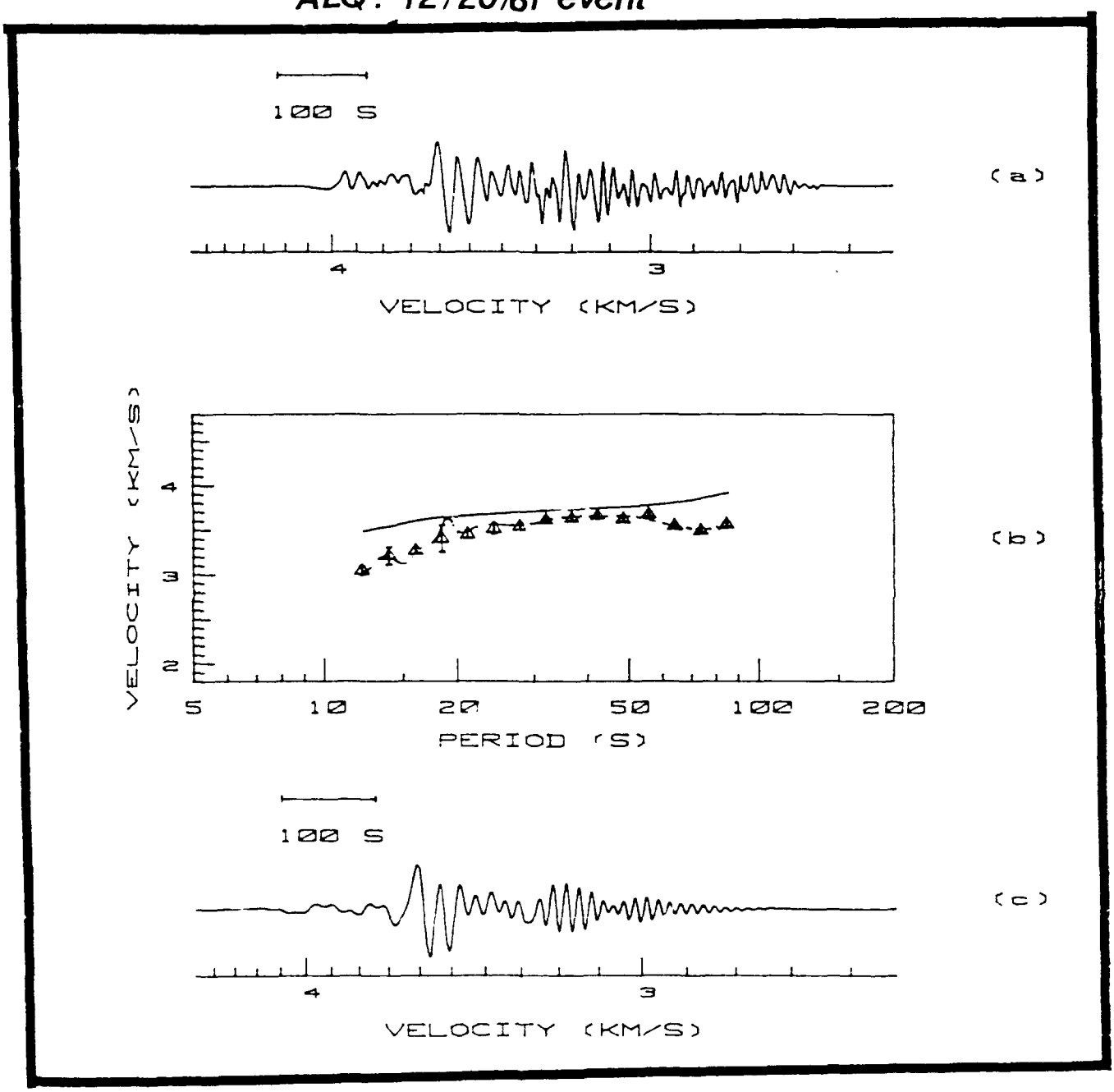
ALQ: 12/20/81 event
100 S
(a)
4
3
VELOCITY (KM/S)
VELOCITY (KM/S)
2
3
4
5
10
20
50
100
200
PERIOD (S)
(b)
100 S
(c)
4
3
VELOCITY (KM/S)

Figure 34.

Figures 35 - 37. (following pages) Filtering results for EPT-ALQ interstation Green's functions. (a) Windowed cross correlation of EPT and ALQ TVF seismograms for single events. (b) Interstation dispersion of seismogram in (a). Triangles = MFT group velocities, dashed curves = PMI group velocities, and solid curves = PMI phase velocities. (c) TVF Green's function based on PMI group velocity curve shown in (b).

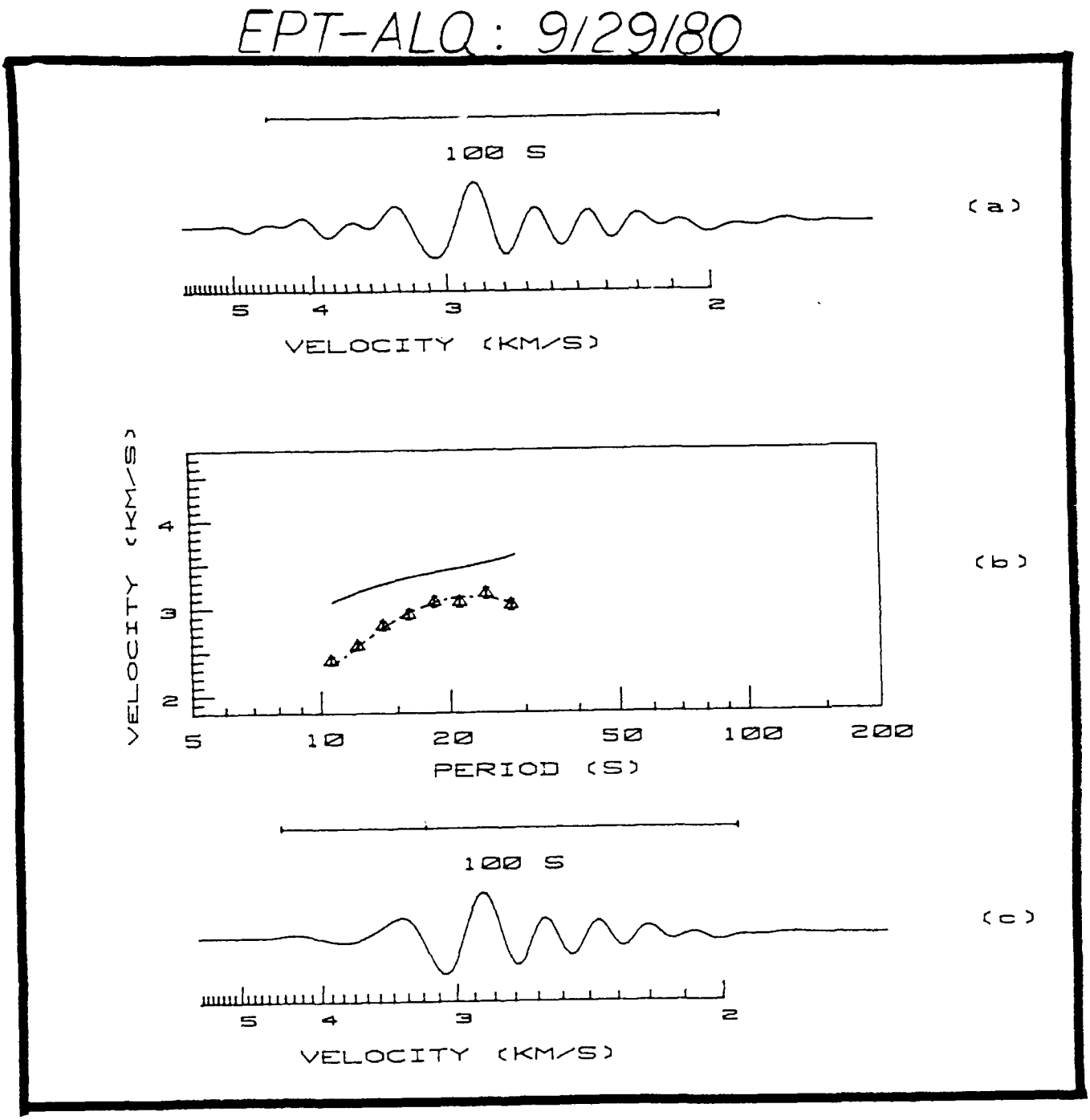
EPT-ALQ: 9/29/80
100 S
(a)
5
4
3
2
VELOCITY (KM/S)
VELOCITY (KM/S)
4
3
2
(b)
5
10
20
50
100
200
PERIOD (S)
100 S
(c)
5
4
3
2
VELOCITY (KM/S)

Figure 35.

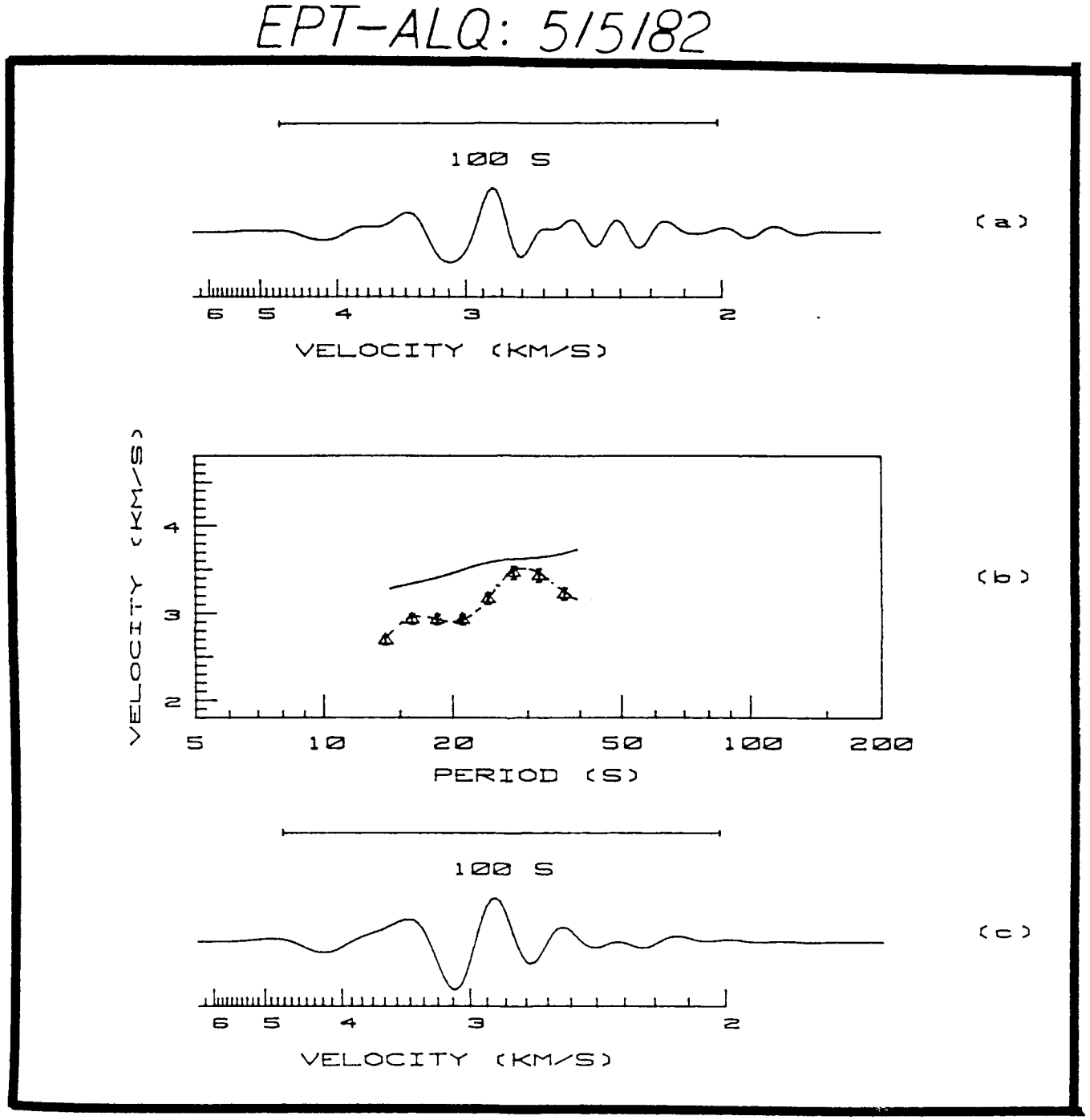
EPT-ALQ: 515182
100 S
(a)
6 5 4 3 2
VELOCITY (KM/S)
VELOCITY (KM/S)
2 3 4
5 10 20 50 100 200
PERIOD (S)
(b)
100 S
(c)
6 5 4 3 2
VELOCITY (KM/S)

Figure 36.

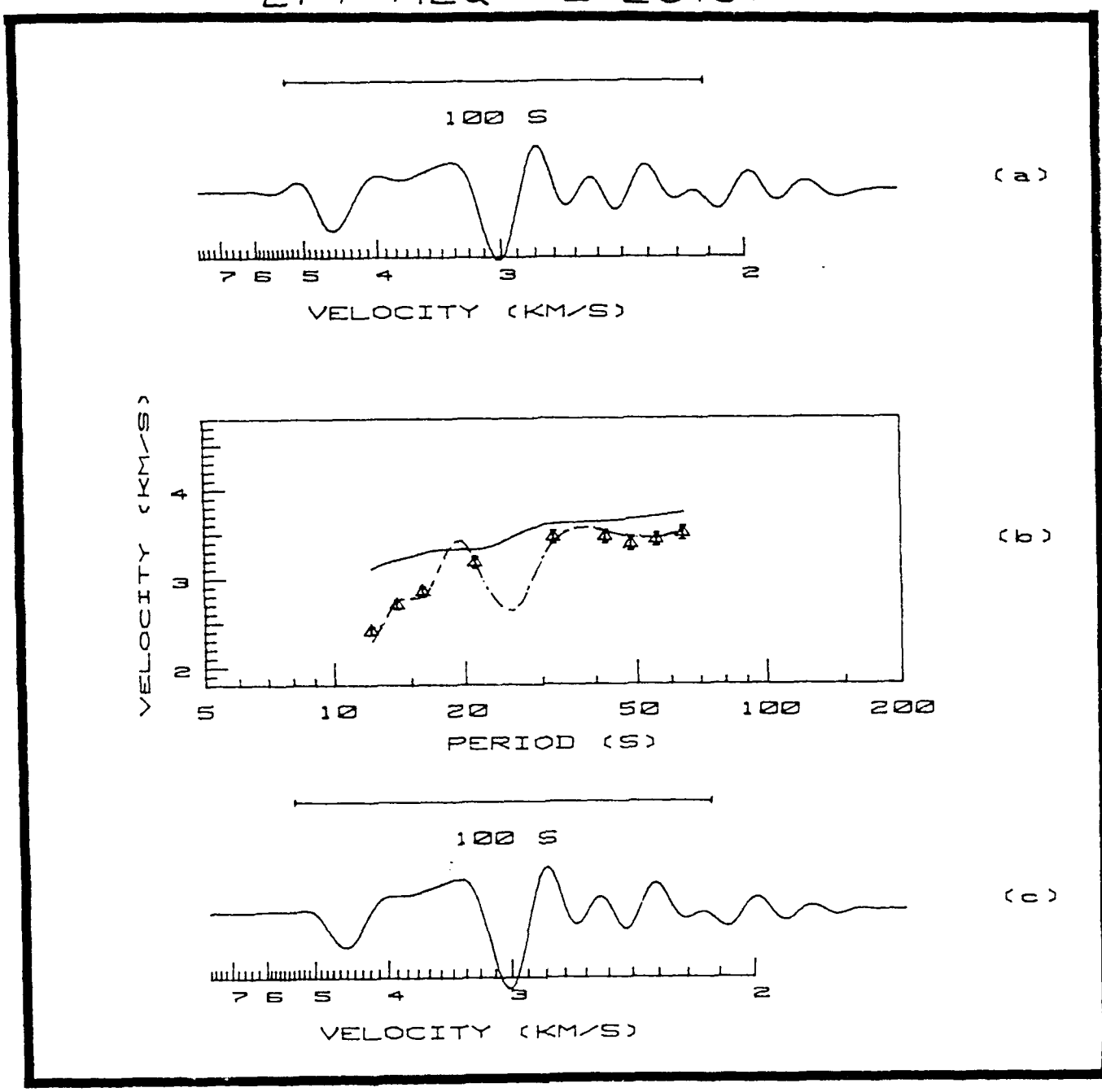
EPT-ALQ: 12/20/81
100 S
(a)
7 6 5 4 3 2
VELOCITY (KM/S)
VELOCITY (KM/S)
2 3 4
5 10 20 50 100 200
PERIOD (S)
(b)
100 S
(c)
7 6 5 4 3 2
VELOCITY (KM/S)

Figure 37.

Figures 38-40. (following pages) EPT-ALQ interstation dispersion determination for the three events. (a) Triangles = MFT-selected group velocities. Solid curves = fast velocities, dashed curves = slow velocities, which are determined by standard errors of the least squares smoothed group velocities and inputs to PMI. (b) Triangles = MFT group velocities, circles = meaned fast and slow PMI output, curves = simultaneous fit dispersion. (c) Final phase and group dispersion with standard errors.

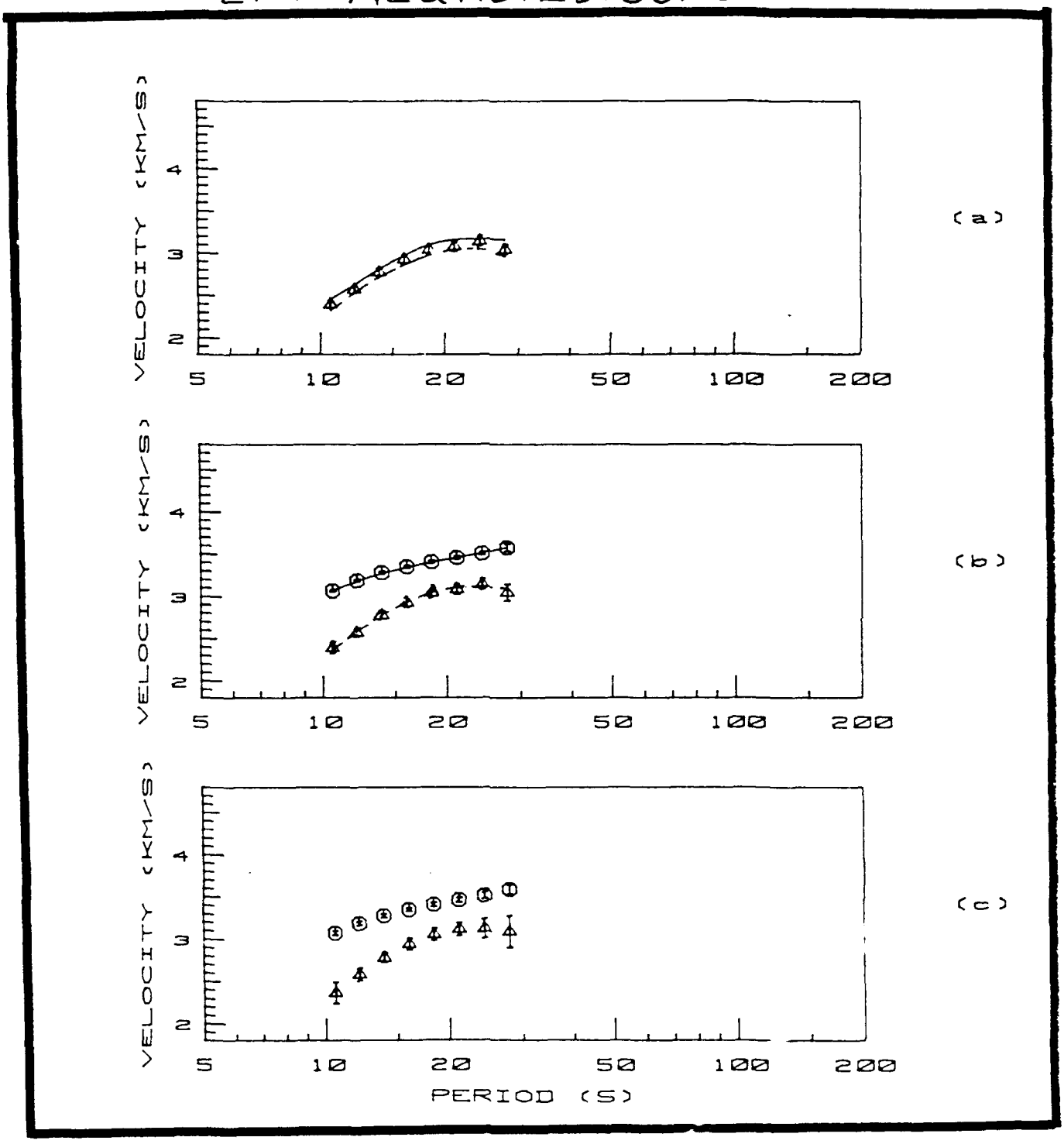
EPT-ALQ:(9/29/80) DISPERSION
VELOCITY (KM/S)
2
3
4
5
10
20
50
100
200
(a)
(b)
(c)
PERIOD (S)

Figure 38.

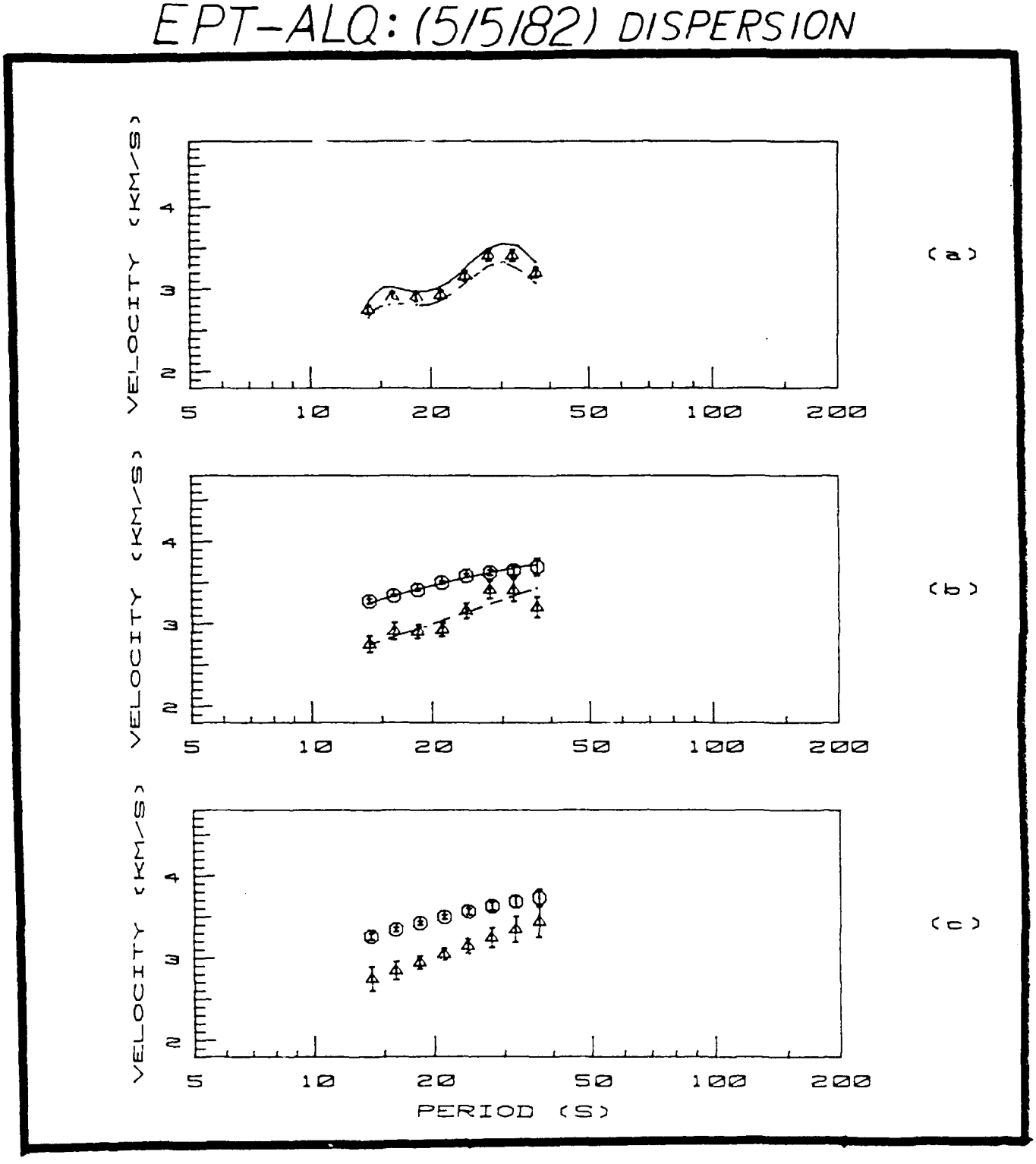
EPT-ALQ: (5/5/82) DISPERSION
VELOCITY (KM/S)
2
3
4
5
10
20
50
100
200
(a)
(b)
(c)
PERIOD (S)

Figure 39.

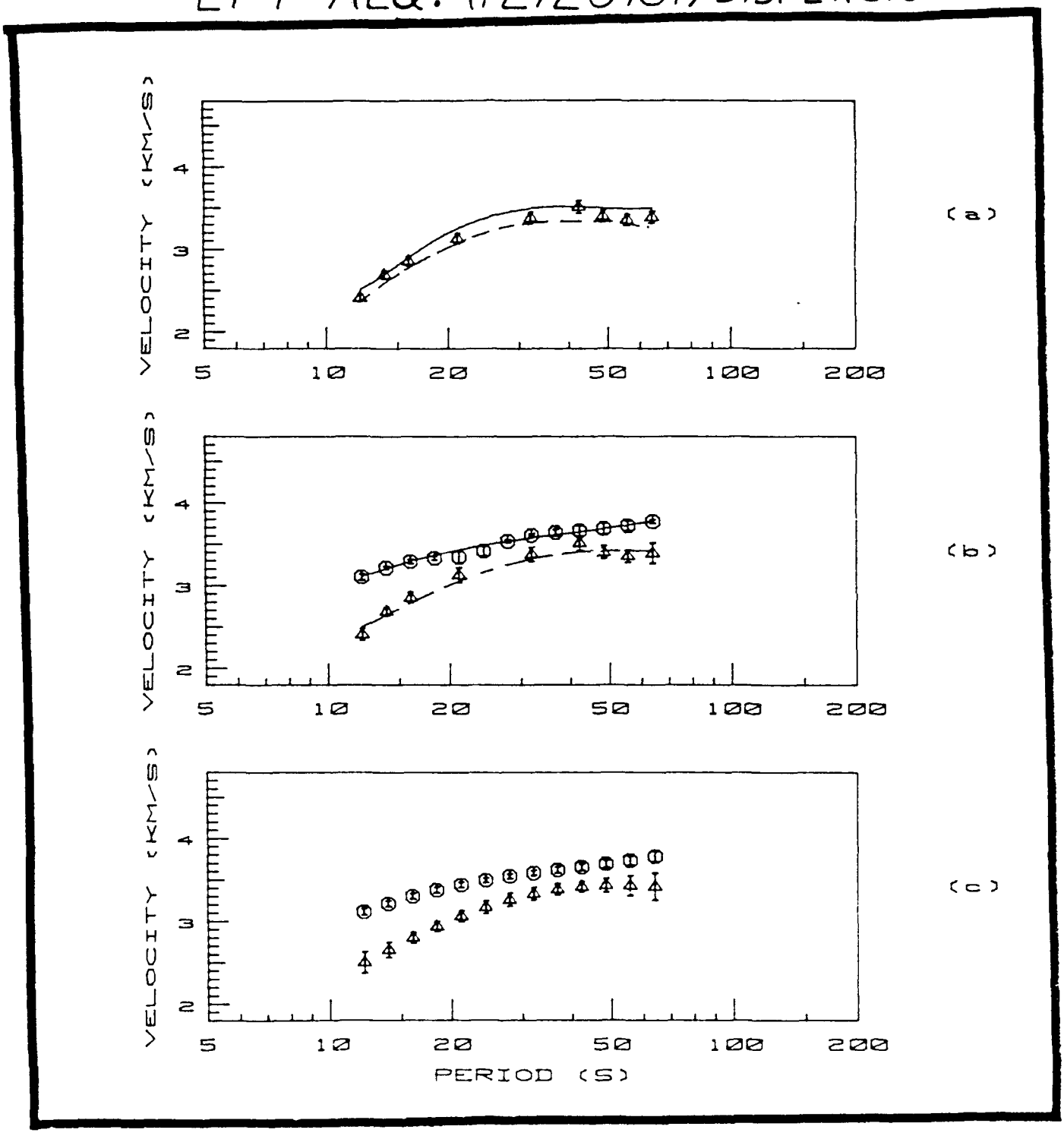
EPT-ALQ: (12120181) DISPERSION
VELOCITY (KM/S)
2
3
4
5
10
20
50
100
200
(a)
(b)
(c)
PERIOD (S)

Figure 40.

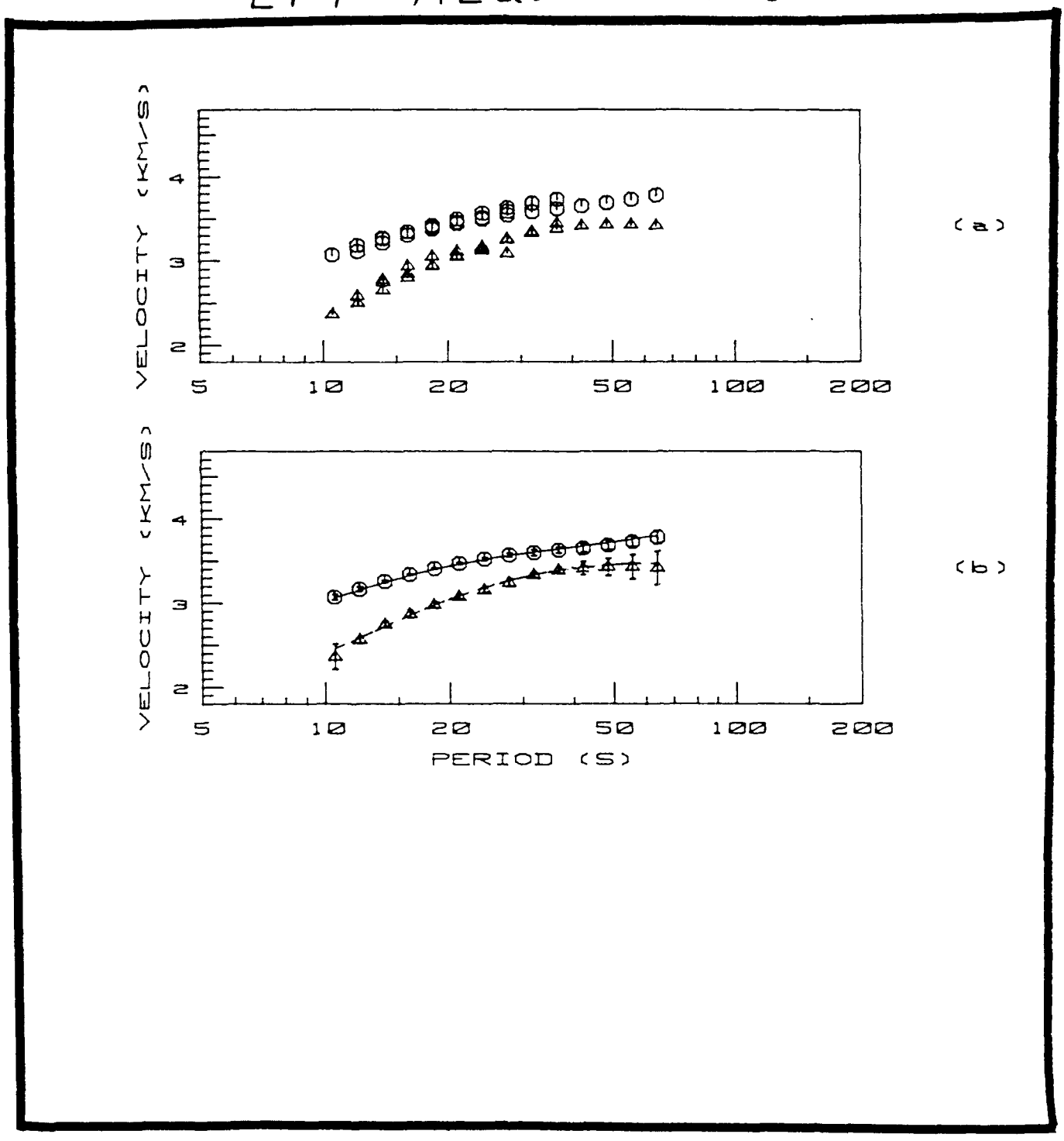

Figure 41. Simultaneous fit of EPT-ALQ interstation dispersion for the three events. (a) Individual event dispersion. (b) Weighted means (triangles group velocity, circles = phase velocity) for the three events with error bars. Curves are the simultaneous fit of the mean data.

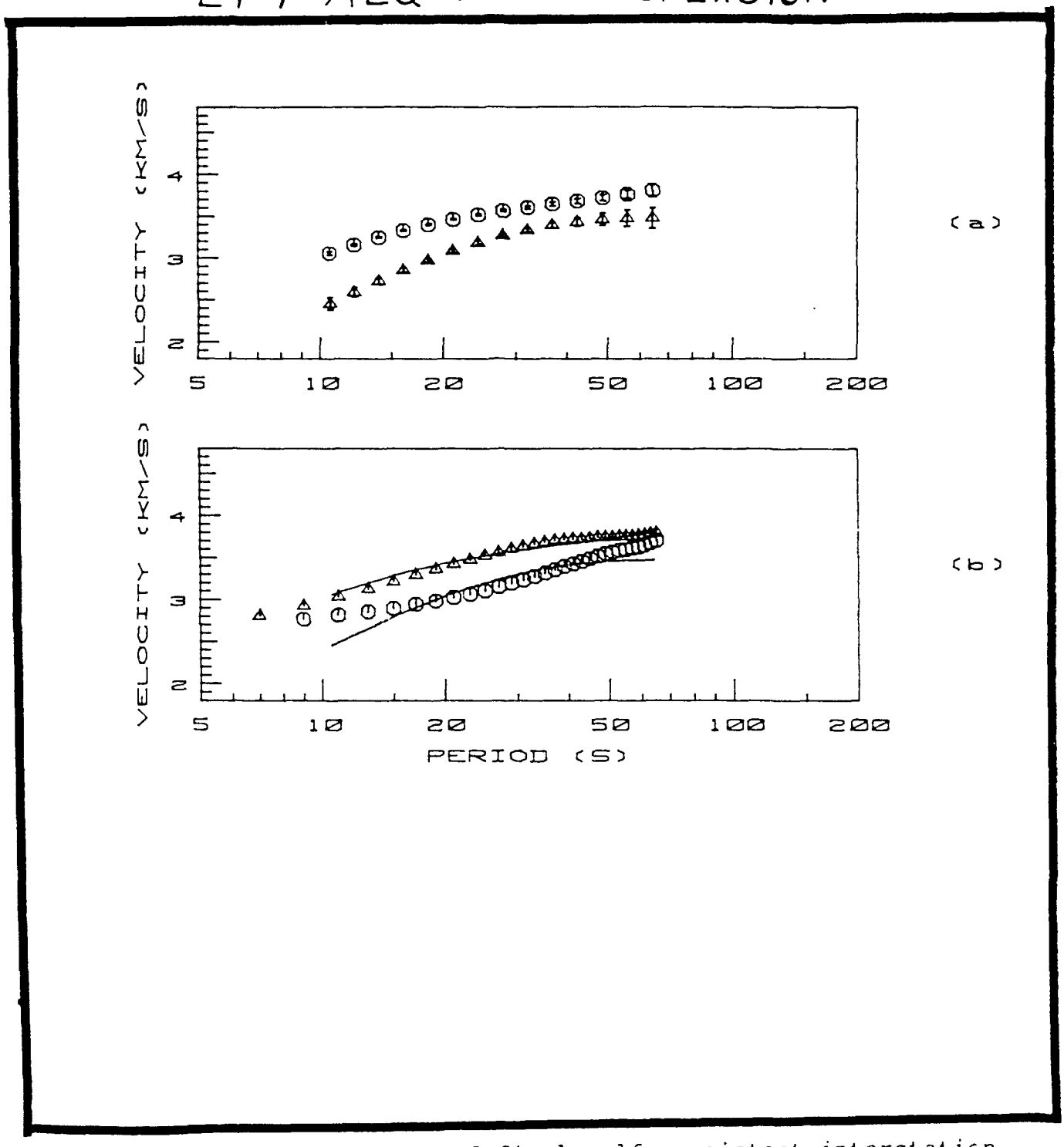

Figure 42. Comparison of final self-consistent interstation dispersion with results from the 1986 study. (a) Final interstation dispersion, this study. Triangles = group velocities, circles = phase velocities, with error bars. (b) Symbols = 1986 study interstation dispersion results, curves = final interstation dispersion, this study.

MODELING OF GROUP AND PHASE DISPERSION

Implementing the first order difference inversion, two starting models are used in the determination of interstation shear velocity structure. First of all, a constrained starting model based on the final model from the southwest back azimuth receiver function analysis is constructed. This biased model is a smoothed version of the southwest model, confined within the standard error bounds in the derived velocity model (Figure 43). Poisson ratios of .24 for the upper crust, .27 for the lower crust, and .29 for the upper mantle are assigned. Initial P-wave velocities are then determined based on the relationship of S-wave velocity and Poisson ratio.

The derived S-wave velocity model (Figure 44, and Table 7) generates the dispersion (solid symbols) shown in Figure 45 and listed in Table 8. This demonstrates a significant match to the group and phase dispersion (open symbols) determined from the filtered interstation Green's functions. The model of shear structure derived from surface wave dispersion should be expected to deviate slightly from the local models for structure beneath ANMO in that (a) it represents velocity structure averaged over the interstation distance through the rift province, and (b) dispersion results are most reliable for the mid-periods; hence, upper and lower portions of the derived models are less reliable. Average shear velocities near 3.4 km/sec for the upper crust,

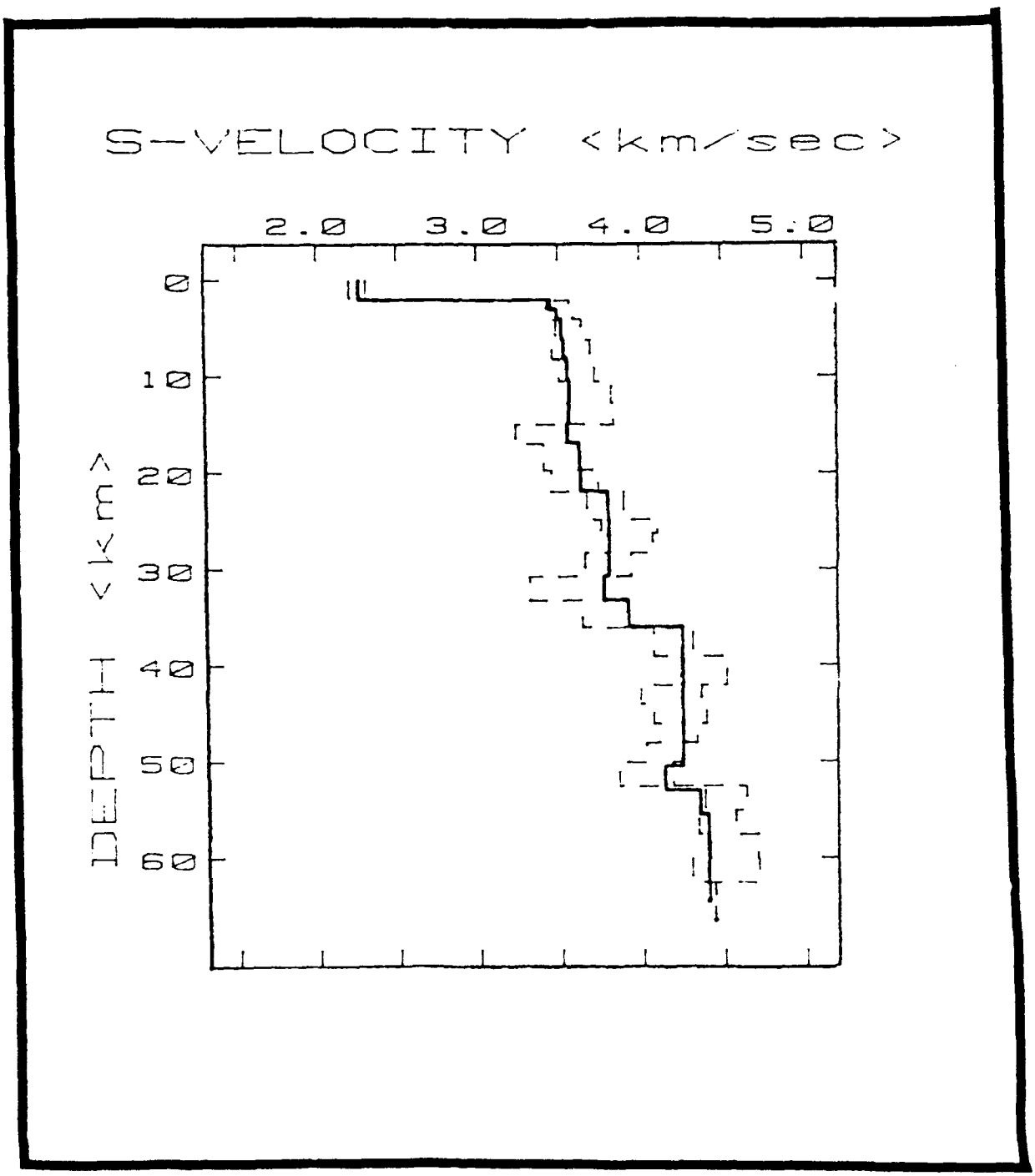

Figure 43. EPT-ALQ S-wave velocity starting model for surface wave inversion, constrained with derived model from southwest back azimuth receiver function modeling. Solid line = starting model, dashed lines = +/- 2 standard errors in southwest model.

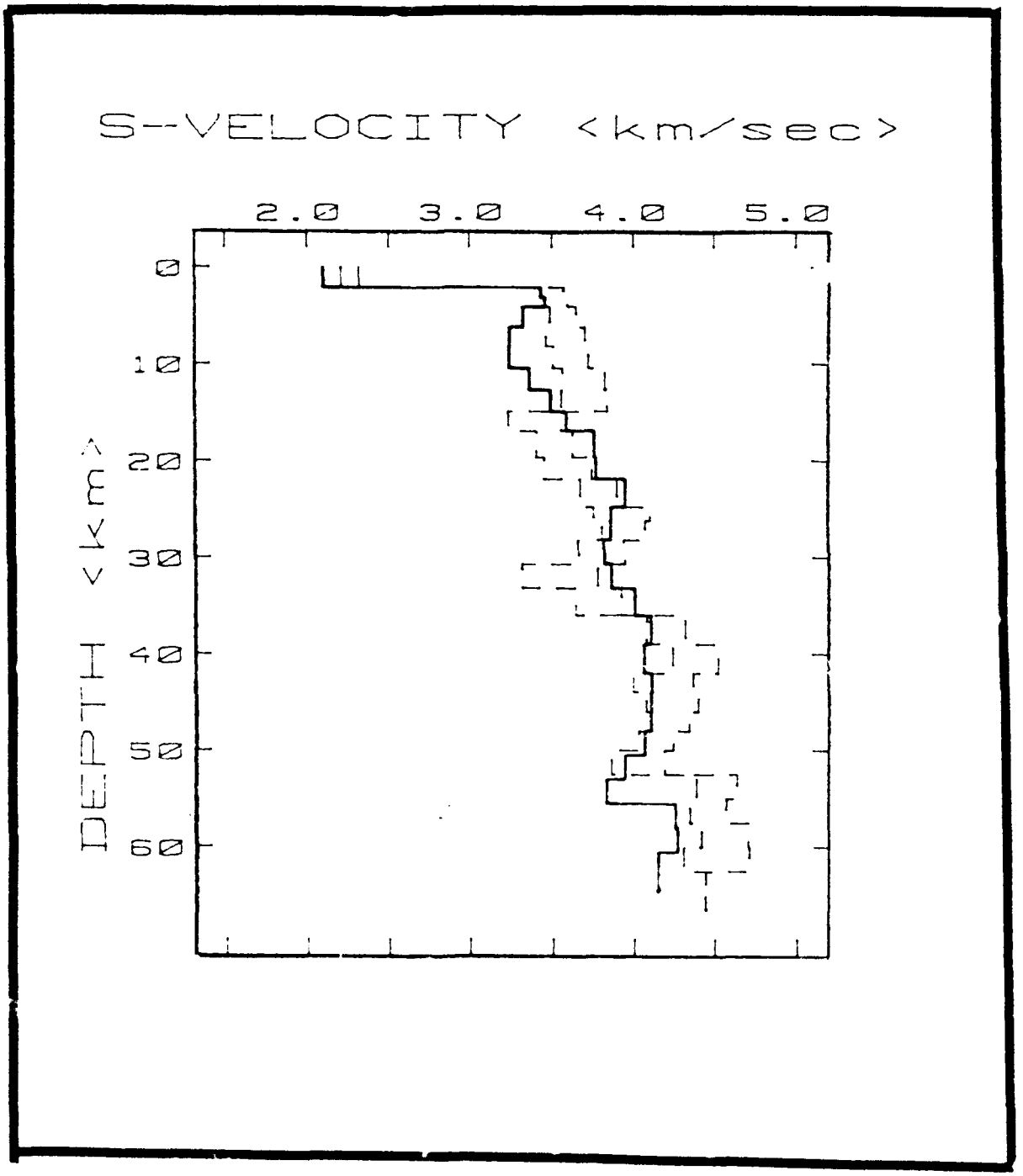

Figure 44. Inversion results from starting velocity model outlined in Figure 43. Solid line = derived model, dashed lines = +/- 2 standard errors in southwest model.

TABLE 7: Final S-wave Velocity Model-- EPT-ALQ Interstation Path (Inversion Constrained with SW Back Azimuth Receiver Function Results)

Layer #	Thickness <km>	EPT-ALQ S-wave Velocity <km/sec>
1	2.10	2.09
2	1.00	3.43
3	1.00	3.45
4	2.10	3.32
5	2.00	3.24
6	2.25	3.23
7	2.25	3.36
8	2.25	3.49
9	2.00	3.58
10	2.75	3.75
11	2.25	3.76
12	2.90	3.95
13	1.40	3.86
14	2.00	3.85
15	2.50	3.81
16	2.50	3.86
17	2.80	4.00
18	3.00	4.10
19	3.00	4.06
20	2.00	4.11
21	2.00	4.10
22	2.00	4.10
23	2.00	4.06
24	2.50	3.94
25	2.50	3.82
26	2.50	4.25
27	2.50	4.27
28	0.00	4.14

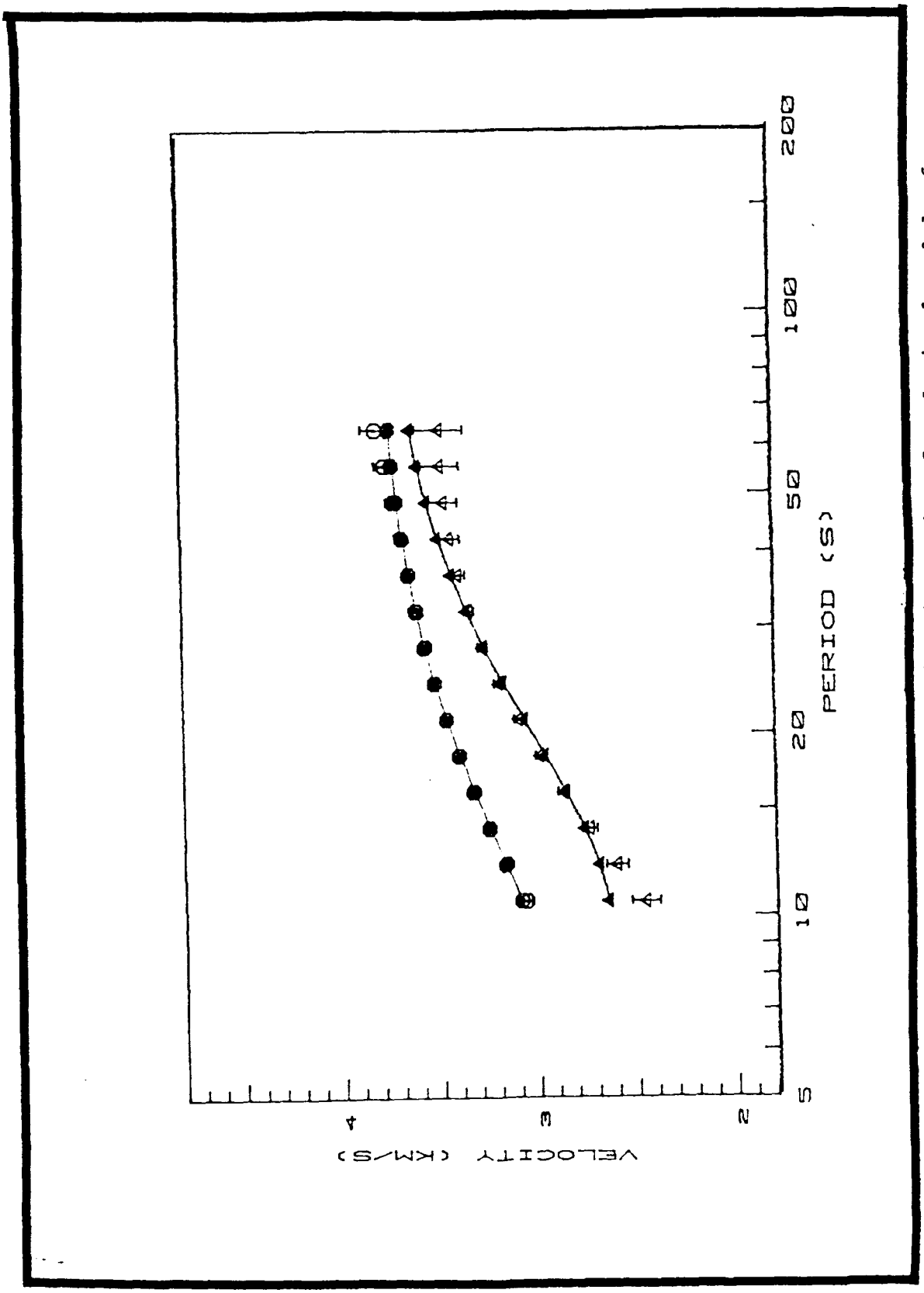

Figure 45. Fit of synthetic dispersion for derived model of Figure 44 to observed self-consistent dispersion. Closed triangles and circles = synthetically determined group and phase velocities, and open triangles and circles (with error bars) = observed group and phase velocities.

TABLE 8: Final Observed-Synthetic Dispersion-- EPT-ALQ Interstation Path (Synthetic Dispersion for Derived Model from Inversion Constrained with SW Back Azimuth Receiver Function Results)

Period <sec>	Simultaneous Fit <km/sec>	Synthetic <km/sec>
	Phase	Phase
10.56	3.060 +/- .024	3.090
12.13	3.160 +/- .016	3.166
13.92	3.250 +/- .012	3.245
16.00	3.331 +/- .011	3.324
18.38	3.402 +/- .012	3.397
21.11	3.464 +/- .013	3.464
24.25	3.519 +/- .015	3.522
27.89	3.566 +/- .018	3.573
32.00	3.608 +/- .021	3.615
36.76	3.647 +/- .025	3.651
42.22	3.684 +/- .030	3.680
48.50	3.721 +/- .037	3.704
55.72	3.762 +/- .049	3.724
64.00	3.808 +/- .069	3.741
	Group	Group
10.56	2.458 +/- .072	2.642
12.13	2.597 +/- .054	2.685
13.93	2.731 +/- .038	2.756
16.00	2.860 +/- .028	2.849
18.38	2.980 +/- .024	2.955
21.11	3.090 +/- .025	3.064
24.25	3.188 +/- .026	3.170
27.86	3.271 +/- .025	3.267
32.00	3.341 +/- .027	3.355
36.76	3.395 +/- .035	3.432
42.22	3.436 +/- .051	3.498
48.50	3.462 +/- .072	3.552
55.72	3.477 +/- .097	3.597
64.00	3.481 +/- .123	3.634

3.6 km/sec for the mid-crust, and 3.7-3.8 for the lower crust are seen in this model. In light of the above considerations, these results agree satisfactorily with the southwest back azimuth modeling results.

A second approach at resolving interstation shear structure involved beginning with a three layer model with 2.25 km/sec for the near surface, 3.4 km/sec for the entire crust, and 4.0 km/sec for the upper mantle (Figure 46). Inversion of this unbiased starting model resulted in a convergence toward the previously derived models (Figure 47). Although this derived model contains unrealistic components (for example, the velocity reversal at 4 to 10 km depth, and the strong first order crust-mantle boundary imposed in the starting model), one can observe that the mid-to-lower crust portion of this model moves within the bounds of the model determined from receiver function analysis. The corresponding dispersion shown in Figure 48 demonstrates the significant fit to observed dispersion. This further supports the previously presented 1-D determinations of shear wave velocity structure beneath ANMO in the Rio Grande rift.

CONCLUSION

The ANMO receiver function study results are significant in at least two ways. Firstly, it has been shown here that conventional methods of modeling detailed receiver structure can be applied for three component digital seismic stations

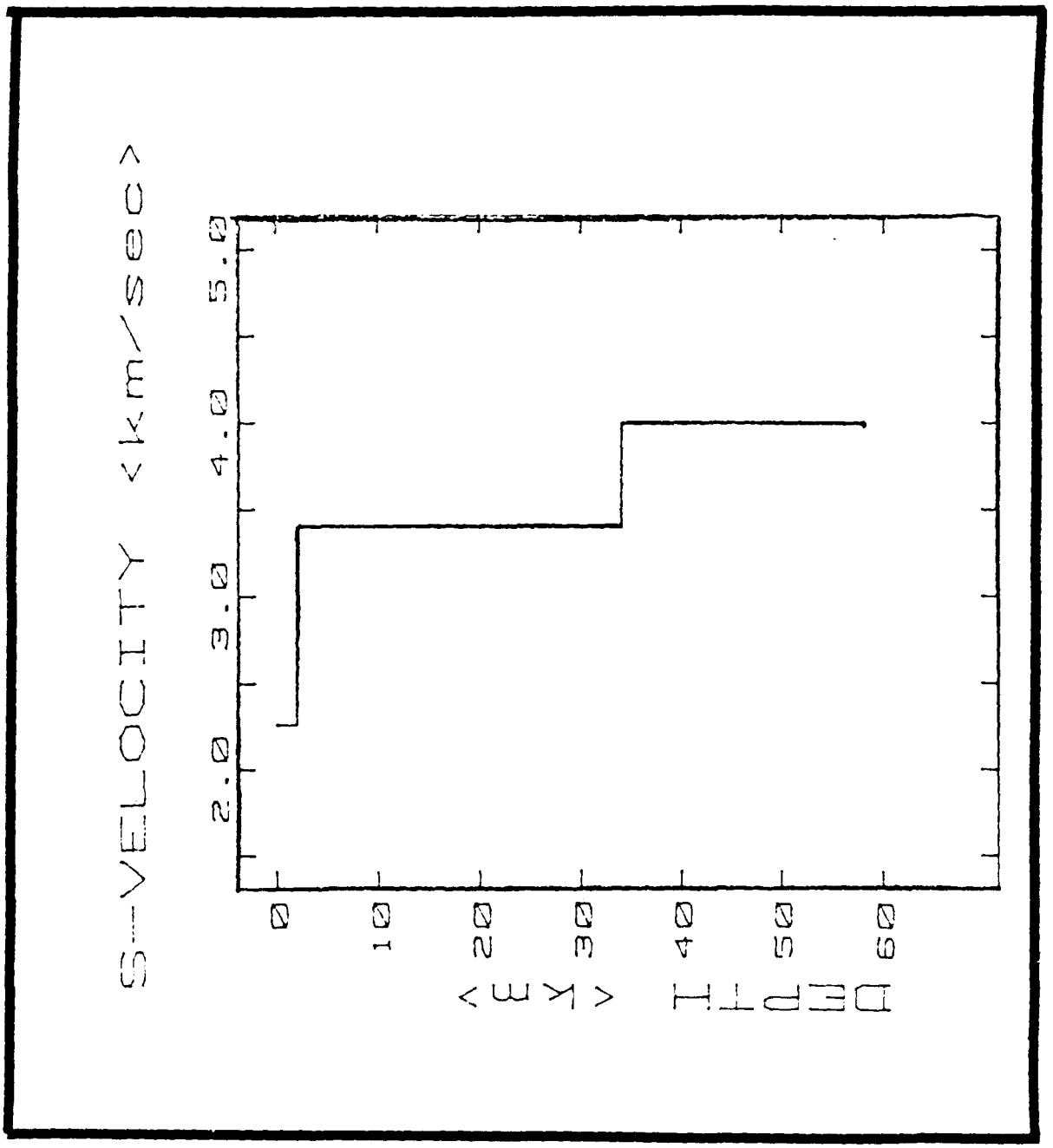

Figure 46. 3-layer EPT-ALQ S-wave velocity starting model for surface wave inversion.

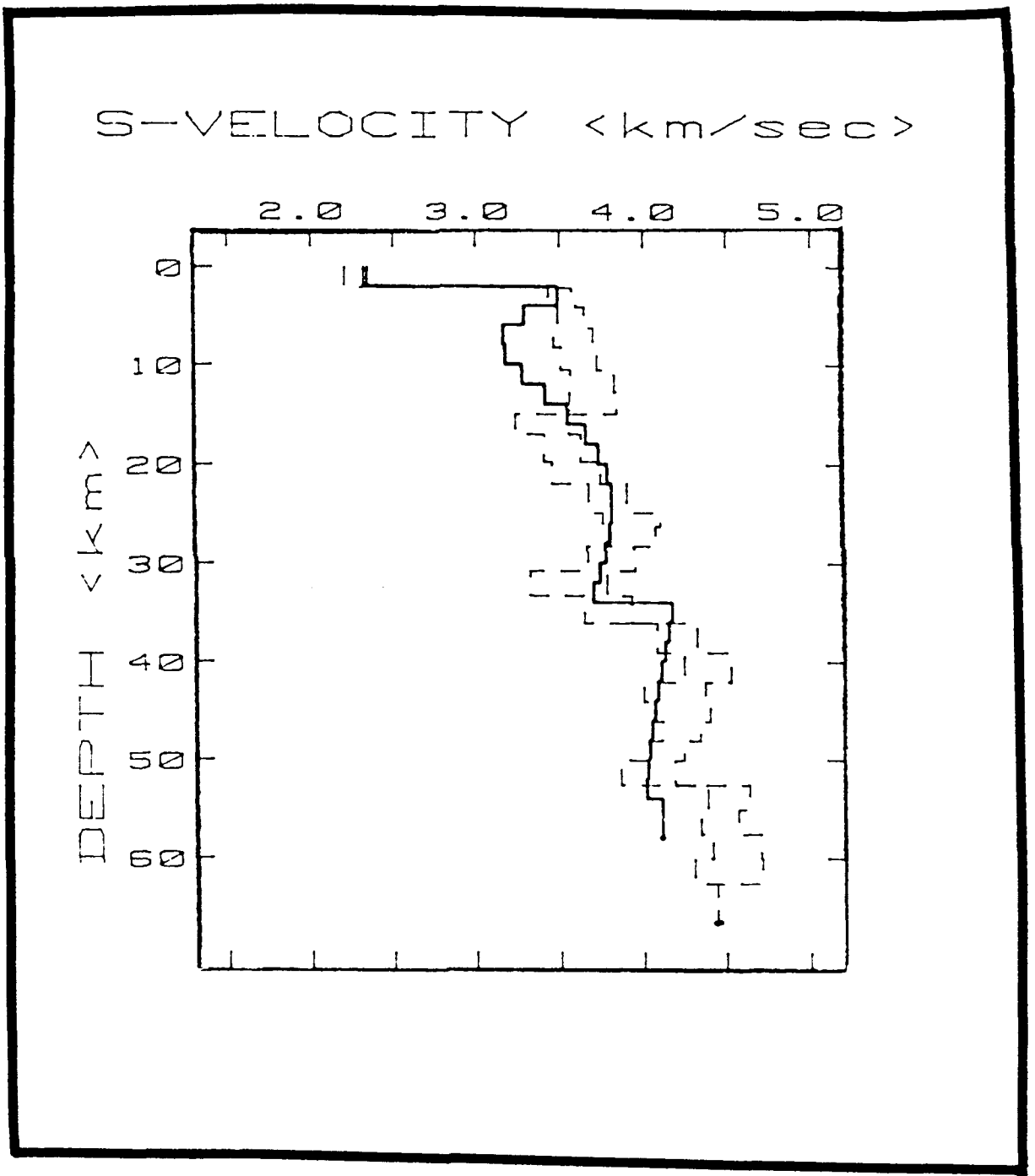

Figure 47. Inversion results from starting model outlined in Figure 46, demonstrating convergence toward southwest back azimuth model in the mid-to-lower crustal range.

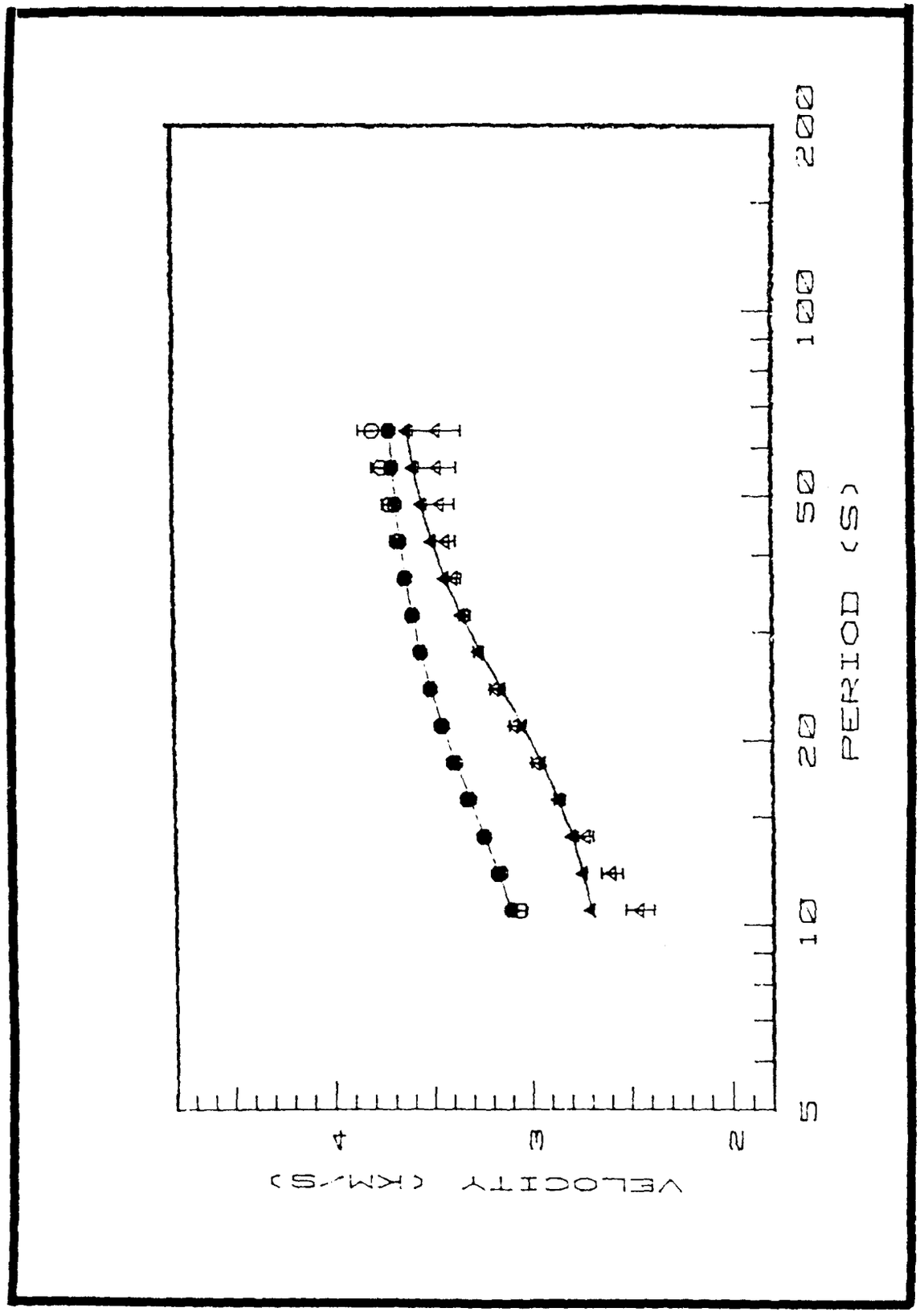

Figure 48. Fit of synthetic dispersion for derived model of Figure 47 to observed self-consistent dispersion. Closed triangles and circles = synthetically determined group and phase velocities, and open triangles and circles (with error bars) = observed group and phase velocities.

lacking broadband instrumentation. Merging the long and short period digital records provides the appropriate bandwidth for such high resolution analysis. Secondly, more information on deep shear structure within the central Rio Grande rift has been provided. Integrating these local findings with results from future such studies within the Rio Grande rift (e.g., EPT receiver structure in the southern rift, and local studies using portable broadband recording instruments) should aid in detailed regional mapping of the extremely heterogeneous lower crustal and upper mantle structure within this province.

The EPT-ALQ dispersion analysis results are quite consistent with those of the original study. This is understandable, given that information outside the original period range analyzed could not be extracted due to the band-limitedness of the dispersion data for such a short interstation path. However, this study provided another estimate of average shear velocity structure along the rift axis using the same data, but processed with different filtering techniques. Also, these S-wave velocity estimates provide a satisfactory tie with the mid-to-lower crustal portion of the velocity model derived in the southwest back azimuth receiver function analysis. These results, together with those from previous Rio Grande rift geophysical studies, will hopefully provide both reliable control for future seismic modeling, and a better understanding of the

petrologic processes taking place within the rift.

APPENDIX

LIST OF COMPUTER PROGRAMS

USED IN THESIS.

PROGRAM: RAY3D

AUTHOR: Dr. T.J. Owens

MODIFICATIONS BY B.P. MURPHY: Replaced S.A.C. (Seismic Analysis Code) input/output subroutines with HP-9000 compatible routines, which manipulate S.A.C. format ASCII files.

PROGRAM PURPOSE: Implementation of Langston's 3-D raytracing method, used in modeling receiver function waveforms.

- -

PROGRAM: PWAVEQN

AUTHOR: Dr. T.J. Owens

MODIFICATIONS BY B.P. MURPHY: Replaced S.A.C. input/output subroutine calls.

PROGRAM PURPOSE: Implementation of Langston's source equalization deconvolution method. Deconvolves vertical component from horizontal component (radial and tangential) seismograms to produce receiver functions.

- -

PROGRAM: STACK

AUTHOR: Dr. T.J. Owens

MODIFICATIONS BY B.P. MURPHY: Added code for determining standard deviations (+/- 1 S.D. about the mean stacked trace) based on data variance. Upper and lower bound output traces are produced.

PROGRAM PURPOSE: Determines a mean receiver function trace for a particular back azimuth by stacking a variable number of receiver functions with approximately equal source distances and directions.

- -

PROGRAM: INVINI

AUTHOR: Dr. T.J. Owens

MODIFICATIONS BY B.P. MURPHY: Replaced S.A.C. input/output subroutine calls.

PROGRAM PURPOSE: Initializes a binary output file, which is input file for the inversion program (TIMINV). This file contains all user selected inversion options, plus user specified starting model and receiver function trace.

- -

PROGRAM: TIMINV

AUTHOR: Dr. T.J. Owens

MODIFICATIONS BY B.P. MURPHY: Replaced S.A.C. input/output subroutine calls.

PROGRAM PURPOSE: Given the binary parameter output file from INVINI, TIMINV inverts a receiver function trace for S-wave velocity. RAY3D is called for forward calculations. Updated S-wave velocity model with upper and lower bound velocity models and the corresponding synthetic radial component receiver function are the output produced.

- -

PROGRAM: HPMERGE

AUTHOR: B. Belmont

MODIFICATIONS BY B. P. MURPHY: None

PROGRAM PURPOSE: Implemetation of Harvey and Choy's data merging technique. Merges WWSSN digital three component LP (long period) and SP (short period) seismograms to produce BB (broadband) seismograms for receiver function waveform modeling.

- -

PROGRAM: ROTATE (subroutine)

AUTHOR: Dr. D. I. Doser

MODIFICATIONS BY B. P. MURPHY: Coded into main calling routine, ROTE.

PROGRAM PURPOSE: Rotates N-S and E-W seismograms in source back azimuth to produce radial and tangential component seismograms.

PROGRAM: SEISMO

AUTHOR: Dr. E. A. Dean

MODIFICATIONS BY B. P. MURPHY: NONE

PROGRAM PURPOSE: Interactive processing routine for determining group and phase velocities and their standard errors for multi-event surface wave data.

- -

PROGRAM: VS3

AUTHOR: B. P. MURPHY

PROGRAM PURPOSE: Plots S-wave velocity vs. Depth models for receiver function analysis. Standard error bars may be included in the plot. VELPARAMS is the required control file.

- -

PROGRAM: S_GRAPH

AUTHOR: B. P. MURPHY

PROGRAM PURPOSE: Plots a user specified number of seismograms stored in S.A.C. ASCII format. S_CONFIG is the required control file.

- -

PROGRAM: FIGURE

AUTHORS: D. G. Roberts and Dr. E. A. Dean

MODIFICATIONS BY B. P. MURPHY: None

PROGRAM PURPOSE: Plots SEISMO output (dispersion curves and filtered seismograms).

- -

PROGRAM: SURF

AUTHOR: Dr. D. R. Russell

MODIFICATIONS BY B. P. MURPHY: None

PROGRAM PURPOSE: Surface wave inversion program. Output is updated S-wave velocity model, and synthetic group and phase dispersion data.

REFERENCES

Ander, M. F., Geophysical study of the crust and upper mantle beneath the central Rio Grande rift and adjacent Great Plains and Colorado Plateau, Los Alamos Nat. Lab. Rep., LA-8676-T, 218 pp., 1981.

Baldridge, W. S., Petrology and petrogenesis of Plio-Pleistocene basaltic rocks from the central Rio Grand rift, New Mexico, and their relation to rift structure, in Rio Grande Rift: Tectonics and Magmatism, edited by R. F. Riecker, pp. 323-353, AGU, Washington, D. C., 1979.

Baldridge, W. S., K. H. Olsen, and J. F. Callender, Rio Grande rift: Problems and Perspectives, Field Conf. Guideb. N. M. Geol. Soc., 35, 1-12, 1984.

Bath, M., and R. Stefansson, S - P Conversions at the base of the crust, Ann. Geofis., 19, 119-130, 1966.

Bloch, S., and A. L. Hales, New techniques for the determination of surface wave phase velocities, Bull. Seismol. Soc. Am., 58, 1021-1034, 1968.

Braile, L. W. and G. R. Keller, Fine structure of the crust inferred from linear inversion of Rayleigh-wave dispersion, Bull. Seismol. Soc. Am., 65, 71-83, 1975.

Bridwell, R. J., Lithospheric thinning and the Late Cenozoic thermal and tectonic regime of the northern Rio Grande rift, Vermejo Park, Field Conf. Guideb. N. M. Geol. Soc., 27, 283-292, 1976.

Brocher, T. M., Geometry and physical properties of the Socorro, New Mexico, magma bodies, J. Geophys. Res., 86, 9420-9432, 1981.

Brown, L. D., C. E. Chapin, A.R. Sanford, S. Kaufman, and J. Oliver, Deep structure of the Rio Grande rift from seismic reflection profiling, J. Geophys. Res., 85, 4773-4800, 1980.

Brown, L. D., P. A. Krumhansl, C. E. Chapin, A. R. Sanford, F. A. Cook, S. Kaufman, J. E. Oliver, and F. S. Schilt, COCORP seismic reflection studies of the Rio Grande rift, in Rio Grande Rift: Tectonics and Magmatism, edited by R. E. Riecker, pp. 169-184, AGU, Washington, D. C., 1979.

Burdick, L. J., and C. A. Langston, Modeling crustal structure through the use of converted phases in teleseismic body-wave forms, Bull. Seismol. Soc. Am., 67, 677-691, 1977.

Callender, J. F., J. W. Hawley, and G. R. Keller, Rio Grande rift, Field Trip Guideb. T318, I.G.C., 37 pp., 1989.

Chapin, C. E., Evolution of the Rio Grande rift, in Rio Grande Rift: Tectonics and Magmatism, edited by R. E. Rieker, pp. 1-5, AGU, Washington, D.C., 1979.

Chapin, C. E., and W. R. Seager, Evolution of the Rio Grande rift in the Socorro and Las Cruces areas, Field Conf. Guideb. N.M. Geol. Soc., 26, 297-321, 1975.

Christensen, N. I., Seismic velocities, in Handbook of Physical Properties of Rocks, edited by R. S. Carmichael, vol. 2, pp. 1-228, CRC, Boca Raton, Florida, 1982.

Cook, F. A., D. B. McCullar, E. R. Decker, and S. B. Smithson, Crustal structure and evolution of the southern Rio Grande rift, in Rio Grande Rift: Tectonics and Magmatism, edited by R. E. Rieker, pp. 195-208, AGU, Washington, D.C., 1979.

Cordell, L., Aeromagnetic and gravity studies of the Rio Grande graben in New Mexico between Belen and Pilar, Spec. Publ. N.M. Geol. Soc., 6, 62-70, 1976.

Cordell, L., Regional geophysical setting of the Rio Grande rift, Geol. Soc. Am. Bull., 89, 1073-1090, 1978.

Cordell, L., Extension in the Rio Grande rift, J. Geophys. Res., 87, 8561-8569, 1982.

Daggett, P. H., G. R. Keller, P. Morgan, and C. L. Wen, Structure of the southern Rio Grande rift from gravity interpretation, J. Geophys. Res., 91, 6143-6156, 1986.

Davis, P. M., E. C. Parker, J. R. Evans, H. M. Iyer, and K. H. Olsen, Teleseismic deep sounding of the velocity structure beneath the Rio Grande rift, Field Conf. Guideb. N.M. Geol. Soc., 35, 29-38, 1984.

de Voogd, B., L.D. Brown, and C. Merey, Nature of the eastern boundary of the Rio Grande rift from COCORP surveys in the Albuquerque basin, New Mexico, J. Geophys. Res., 91, 6305-6320, 1986.

Dean, E. A., The simultaneous smoothing of phase and group velocities from multi-event surface wave data, Bull. Seismol. Soc. Am., 76, 1367-1383, 1986.

Dean, E. A., and G. R. Keller, Interactive processing to obtain interstation surface-wave dispersion, Bull. Seismol. Soc. Am., to be published.

Decker, E. R., and S. B. Smithson, Heat flow and gravity interpretation across the Rio Grande rift in southern New Mexico and west Texas, J. Geophys Res., 80, 2542-2552, 1975.

Ernst, W. G., Petrological Phase Equilibria, 331 pp., W. H. Freeman and Co., 1976.

Frost, B. R., and C. D. Frost, CO2, melts and granulite metamorphism, Nature, 327, 503-506, 1987.

Harvey, D., and G. L. Choy, Broad-band deconvolution of GDSN data, Geophys. J. R. Astr. Soc., 69, 659-668, 1982.

Haskell, N. A., Crustal reflection of plane P and SV waves, J. Geophys. Res., 67, 4751-4767, 1962.

Hathaway, A. W. and G. A. Kiersch, Engineering properties of rock, in Handbook of Physical Properties of Rocks, edited by R. S. Carmichael, vol. 2, pp. 289-331, CRC, Boca Raton, Florida, 1982.

Keller, G. R., P. Morgan, and W. R. Seager, Crustal structure, gravity anomalies and heat flow in the southern Rio Grande rift and their relationship to extensional tectonics, Tectonophyics, 174, 21-37, 1990.

Knopoff, L., M. J. Berry, and F. A. Schwab, Tripartite phase velocity observations in laterally heterogeneous regions, J. Geophys. Res., 72, 2595-2601, 1967.

Landisman, M., A. Dziewonski, and Y. Sato, Recent improvements in the analysis of surface wave observations, Geophys. J. R. Astr. Soc., 17, 369-403, 1969.

Langston, C. A., The effect of planar dipping structure on source and receiver responses for constant ray parameter, Bull. Seism. Soc. Am. 67, 1029-1050, 1977.

Langston, C. A., Structure under Mount Rainier, Washington, inferred from teleseismic body waves, J. Geophys. Res., 84, 4749-4762, 1979.

Lozinsky, R. P., Stratigraphy, sedimentology, and sand petrology of the Santa Fe group and pre-Santa Fe Tertiary deposition in the Albuquerque basin, central New Mexico, Ph.D. Dissertation, 298 pp., New Mexico Institute of Mining and Technology, Socorro, 1988.

Morgan, P., and M. P. Golombek, Factors controlling the phases and styles of extension in the northern Rio Grande rift, Field Conf. Guideb. N. M. Geol. Soc., 35, 13-19, 1984.

Morgan, P., W. R. Seager, and M. P. Golombek, 1986, Cenozoic thermal, mechanical, and tectonic evolution of the Rio Grande rift, J. Geophys. Res., 91, 6263-6276, 1986.

Olsen, K. H., G. R. Keller, and J. N. Stewart, Crustal along the Rio Grande rift, in Rio Grande Rift: Tectonics and Magmatism, edited by R. E. Riecker, pp. 127-143, AGU, Washington, D.C., 1979.

Owens, T. J., Determination of crustal and upper mantle structure from analysis of broadband teleseismic P-waveforms, PH.D. Dissertation, University of Utah, Salt Lake City, Utah, 146 pp, 1984.

Owens, T. J., G. Zandt, and S. R. Taylor, Seismic evidence for an ancient rift beneath the Cumberland Plateau, Tennessee: A detailed analysis of broadband teleseismic P-waveforms, J. Geophys. Res., 89, 7783-7795, 1984.

Owens, T. J., Shallow structure effects on broadband teleseismic P waveforms, Bull. Seismol. Soc. Am., 78, 96-108, 1988.

Perry, F. V., W. S. Baldridge, and D. J. DePaolo, Chemical and isotopic evidence for lithospheric thinning beneath the Rio Grande rift, Nature, 332, 432-434, 1988.

Ramberg, I. B., F. A. Cook, and S. B. Smithson, Structure of the Rio Grande rift in southern New Mexico and west Texas based on gravity interpretation, Geol. Soc. Am. Bull., 89, 107-123, 1978.

Ramberg, I. B., and S. B. Smithson, Gridded fault patterns in a late Cenozoic and Paleozoic continental rift, Geology, 3, 201-205, 1975.

Reiter, M., R. E. Eggleston, B. R. Broadwell, and J. Minier, Terrestrial heat flow estimates from deep petroleum tests along the Rio Grande rift, J. Geophys. Res., 91, 6225-6245, 1986.

Rhinehart, E. J., A. R. Sanford, and R. M. Ward, Geographic extent and shape of an extensive magma body at mid crustal depths in the Rio Grande rift near Socorro, New Mexico, in Rio Grande Rift: Tectonics and Magmatism, edited by R. E. Riecker, pp. 237-251, AGU, Washington, D.C., 1979.

Russell, D. R., Constrained inversion techniques applied to surface wave analysis, M.S. thesis, 76 pp., Univ. of Tex. at El Paso, El Paso, 1980.

Russell, L. R., and S. Snelson, Structural style and tectonic evolution of the Albuquerque basin segment of the Rio Grande rift, The Potential of Deep Seismic Profiling for Hydrocarbon Exploration, edited by B. Pinet and C. Bois, pp. 175-207, Paris, 1990.

Sanford, A. R., O. S. Alptekin, and T. R. Toppozada, Use of reflection phases on microearthquake seismograms to map an unusual discontinuity beneath the Rio Grande rift, Bull. Seismol. Soc. Am., 63, 2021-2034, 1973.

Schlue, J. W., P. J. Singer, and C. L. Edwards, Shear wave structure of the upper crust of the Albuquerque-Belen basin from Rayleigh wave phase velocities, J. Geophys. Res., 91, 6277-6281, 1986.

Seager, W. R. and P. Morgan, Rio Grande rift in southern New Mexico, west Texas, and northern Chihuahua, in Rio Grande Rift: Tectonics and Magmatism, edited by R. E. Riecker, pp. 87-106, AGU, Waxhington, D.C., 1979.

Seager, W. R., M. Shafiqullah, J. W. Hawley, and R. F. Marvin, New K-Ar dates from basalts and the evolution of the southern Rio Grande rift, Geol. Soc. Am. Bull., 95, 87-89, 1984.

Sinno, Y. A. and G. R. Keller, A Rayleigh wave dispersion study between El Paso, Texas and Albuquerque, New Mexico, J. Geophys. Res., 91, 6168-6174.

Sinno, Y. A., P. H. Daggett, G. R. Keller, P. Morgan, and S. H. Harder, Crustal structure of the southern Rio Grande rift determined from seismic refraction profiling, J. Geophys. Res., 91, 6143-6156, 1986.

Thomson, W. T., Transmission of elastic waves through a stratified solid medium, J. Appl. Phys., 21, 89-93, 1950.

Toppozada, T. R., and A. R. Sanford, Crustal structure in central New Mexico interpreted from the Gasbuggy explosion, Bull. Seismol. Soc. Am., 66, 877-886, 1976.

Twomey, S., Introduction to the Mathematics of Inversion in Remote Sensing and Indirect Measurements, 243 pp., Elsevier Scientific, Amsterdam, 1977.

Weber, K., Metamorphism and crustal rheology--implications for the structural development of the continental crust during prograde metamorphism, in The Nature of the Lower Continental Crust, edited by J. B. Dawson, D. A. Carswell, J. Hall, and K. H. Wedepohl, Geol. Soc. Spec. Publ., 24, pp. 95-106, 1986.

Wiggins, R. A., Interpolation of digitized curves, Bull. Seismol. Soc. Am., 65, 2077-2081, 1976.

VITA

Brian Paul Murphy was born on March 10, 1964 in Beeville, Texas. He graduated in 1982 from Three Rivers High School in Three Rivers, Texas. In 1986, he received his B. S. degree in geology from Corpus Christi State University. He attended the University of Texas at El Paso from 1988 to 1991, completing an M. S. degree in geophysics. During the summer of 1990, he worked as a geophysicist for Pecten International Company in Houston, Texas. Upon completion of his M. S. degree in 1991, he began working as an exploration geophysicist with ARCO Oil and Gas Company in Houston, Texas.

Permanent Address: 14814 Perthshire Rd. # 231
Houston, Texas
77079

This thesis was typed by Brian Paul Murphy